The East Greenland Coastal Current: its structure, variability, and large-scale impact

by

David A. Sutherland

B.A., University of North Carolina, Wilmington, 2001

Submitted in partial fulfillment of the requirements for the degree of
Doctor of Philosophy
at the

MASSACHUSETTS INSTITUTE OF TECHNOLOGY

and the

WOODS HOLE OCEANOGRAPHIC INSTITUTION

February 2008

Author...
Joint Program in Oceanography / Applied Ocean Science and Engineering
Massachusetts Institute of Technology
and Woods Hole Oceanographic Institution
January 2, 2008

Certified by...
Robert S. Pickart
Thesis Supervisor

Accepted by..
Raffaele Ferrari
Chair, Joint Committee for Physical Oceanography

The East Greenland Coastal Current: its structure, variability, and large-scale impact

by David A. Sutherland

Submitted to the Joint Program in Physical Oceanography
on January 2, 2008 in partial fulfillment for the
requirements of degree of Doctor of Philosophy

Abstract

The subtidal circulation of the southeast Greenland shelf is described using a set of high-resolution hydrographic and velocity transects occupied in summer 2004. The main feature present is the East Greenland Coastal Current (EGCC), a low-salinity, high-velocity jet with a wedge-shaped hydrographic structure characteristic of other surface buoyancy-driven currents. The EGCC was observed along the entire Greenland shelf south of Denmark Strait, while the transect north of the strait showed only a weak shelf flow. This observation, combined with evidence from chemical tracer measurements that imply the EGCC contains a significant Pacific Water signal, suggests that the EGCC is an inner branch of the polar-origin East Greenland Current (EGC). A set of idealized laboratory experiments on the interaction of a buoyant current with a submarine canyon also supported this hypothesis, showing that for the observed range of oceanic parameters, a buoyant current such as the EGC could exhibit both flow across the canyon mouth or into the canyon itself, setting the stage for EGCC formation. Repeat sections occupied at Cape Farewell between 1997 and 2004 show that the alongshelf wind stress can also have a strong influence on the structure and strength of the EGCC and EGC on timescales of 2-3 days. Accounting for the wind-induced effects, the volume transport of the combined EGC/EGCC system is found to be roughly constant (~2 Sv) over the study domain, from 68°N to Cape Farewell near 60°N. The corresponding freshwater transport increases by roughly 60% over this distance (59 to 96 mSv, referenced to a salinity of 34.8). This trend is explained by constructing a simple freshwater budget of the EGCC/EGC system that accounts for meltwater runoff, melting sea-ice and icebergs, and net precipitation minus evaporation. Variability on interannual timescales is examined by calculating the Pacific Water content in the EGC/EGCC from 1984-2004 in the vicinity of Denmark Strait. The PW content is found to correlate significantly with the Arctic Oscillation index, lagged by 9 years, suggesting that the Arctic Ocean circulation patterns bring varying amounts of Pacific Water to the North Atlantic via the EGC/EGCC.

Thesis Supervisor: Robert S. Pickart
Title: Senior Scientist, WHOI

Acknowledgments

This thesis is dedicated to my family, who have supported all my adventures, even as a Yankee, with gusto.

My advisor, Bob Pickart, deserves a huge thank you for giving me the opportunity to pursue this research by inviting me along on the initial cruise and allowing me first crack at the dataset that emerged. He also provided constant guidance and was quick to refocus my attention when it wandered. Funding for the cruise and analysis was provided by the National Science Foundation, under grant OCE-0450658. The WHOI Academic Programs Office and the MIT Assistance Fund also contributed some funds for my travels to present this research at meetings, and for trips to meet with Bob during his sabbatical in Fairbanks, Alaska.

Many others contributed to the processing of the data used here, in particular I would like to thank Dan Torres (ADCP man), Terry McKee, Paula Fratantoni, and Jane Eert. The captain and crew of the *RRS James Clark Ross* contributed flawless service in obtaining the data during the summer of 2004. Chemical analyses were done by Kumiko Azetsu-Scott and her group at BIO, while Peter Jones, also at BIO, was extremely helpful in his comments on the nutrient chapter.

I would also like to thank the rest of my committee for their encouragement along the way, as well as their open door policy outside of committee meetings. Claudia Cenedese helped immensely with the setup of the laboratory experiments and gave me guidance early on in my grad school career as my initial advisor. Fiamma Straneo also was always ready to give advice, as was Steve Lentz. Dave Fratantoni and Amy Bower invited me on their field expeditions during my time at WHOI, and I will always be ready in case they need more help, as they were great experiences!

My friends in the Joint Program were essential in getting me to the finish line. In fact, I may have faltered at the starting line if it wasn't for the big group we had up at MIT during those first two years: Matt, Max, Ariane, Yohai, Dave, Asher, and Greg. And to all the other students who came in with us and enjoyed those stormy days on the *SSV Corwith Cramer*, the Barn, and the Hole in general: thank you!

Along the way many of these same friends actually gave me good scientific advice as well. And my gratitude goes out to past and present office mates and friends, as they provided easy examples to follow, as well as many fun times: Melanie, Jim, Carlos, Andrew, Jake, Bea, Stephanie, Kjetil, and Alex.

And lastly, I would like to express my sincere thanks to the Joint Program for pushing interdisciplinary science, as it led me to meet my future wife! My love for Kelly grew during the years I spent in Woods Hole and without her, my time here would have been vastly different. Thank you Kelly for giving me your love and for always being there no matter what.

Contents

Chapter 1

Introduction

Historically, the subpolar gyre of the North Atlantic Ocean is second only to its southern counterpart, the North Atlantic subtropical gyre and the Gulf Stream, in the amount of observational and theoretical study invested in trying to understand its motions. A general sense of the large-scale cyclonic circulation in the northern North Atlantic, and the convergence of polar-origin waters with those of the warmer and saltier subtropical region, has been known for at least 150 years, starting with the mid-nineteenth century Danish explorations into the region [see *Pickart et al.*, 2005 for a summary].

However, the details of the subpolar gyre circulation are still lacking, particularly along the boundaries of Greenland, where observations are difficult to obtain due to the presence of sea ice during most of the year that limits the use of research vessels, drifters, and standard mooring designs in the region. Cloud cover consistently blankets the region as well, which inhibits the use of remote-sensing techniques.

The main goal of this thesis is to improve our understanding of the circulation over the shelf region of southeast Greenland, where little is known inshore of the shelfbreak where the main currents of the subpolar gyre reside. The shelf and overlying ocean environment are complex, with numerous bathymetric irregularities, strong wind forcing on small spatial scales, and multiple sources of buoyancy input (meltwater runoff, precipitation, ice melt), along with intense mixing associated with the frontal region between the polar-origin shelf water and the northern remnants of the Gulf Stream.

Despite these complexities, a coherent coastal current feature has been observed several times near the southern tip of Greenland at Cape Farewell and has been named the East Greenland Coastal Current (EGCC), to distinguish it from the shelfbreak flow of the East Greenland and Irminger Currents (EGC, IC, respectively). The main objectives of this thesis focus on the coastal current flow and are, specifically, to

- describe the basic hydrographic and velocity structure of the EGCC, both across-shelf and along-shelf,
- determine the impact of the EGCC on the regional volume and freshwater budgets of the subpolar gyre,
- identify the contributions of freshwater to the EGCC in order to understand its origins,
- understand the formation process of the EGCC and determine its interaction, if any, with the EGC/IC system at the shelfbreak,
- and place the EGCC in context with other high-latitude coastal currents and understand the dominant processes controlling its behavior.

1.1 Thesis outline

The rest of this thesis is devoted to meeting the above objectives, and to answering any corresponding questions stemming from the research. The chapters are organized as follows.

Chapter 1 is an introductory chapter, starting with a list of thesis objectives and a brief outline of the thesis. Background on important aspects of the circulation in the subpolar gyre is given next, including some of the main forces that drive it. This broad introduction to the subpolar gyre circulation leads into a more detailed background on what is known about the EGCC from previous studies. Then, the main source of data used in this thesis is introduced along with the motivation for the field project that produced the data. Details on data processing and additional data sources are left for subsequent chapters.

Chapter 2 describes the hydrographic and velocity structure of the EGCC using sections obtained in the summer of 2004, addressing both the across-shelf and along-shelf evolution of the current. This chapter includes an objective definition of the EGCC, distinguishing it from the EGC, which has been a source of confusion historically. Despite the spatial distinction between the currents, though, the hydrographic properties of the EGCC suggest a close link between the EGCC and the EGC. Chapter 2 concludes with a discussion of additional hydrographic and velocity transects across the shelf at Cape Farewell that begin to elucidate the temporal variability of the EGCC and the main factor, along-shelf wind forcing, that is responsible for this variability.

Chapter 3 continues the description of the EGCC along the southeast coast of Greenland by calculating its volume and freshwater fluxes. These are compared with the calculated transports of the EGC, and are found to be similar in magnitude and co-varying, suggesting that the EGC and EGCC comprise a single system of equatorward-traveling polar-origin water over the Greenland shelf. A simple technique for adjusting the transports to reflect the along-shelf wind forcing is presented, which significantly enhances the interpretation of the results. Once these adjusted trends are computed, the chapter ends with a freshwater budget calculation for the southeast Greenland shelf region, showing that after the advection of freshwater in the EGC/EGCC system, melt from sea ice is the next largest contribution.

Chapter 4 utilizes chemical tracer techniques to explore the freshwater composition of the EGCC in more detail. Specifically, a combination of nitrate-phosphate relationships, oxygen isotope, and alkalinity data are used to quantify the amount of Pacific Water (which must ultimately be of Arctic-origin), sea ice melt, and meteoric water in the EGCC. A discussion follows on the origins of the EGCC, concluding that it does contain a significant amount of Pacific Water and thus is linked to the EGC as it exits the Arctic Ocean at Fram Strait. Historical data are then used to look at the interannual variability in the Pacific Water signal in the EGC/EGCC at Denmark and

Fram Straits (see Fig. 1.1), and some implications for the Arctic Ocean circulation are deduced from these results.

Chapter 5 describes a set of laboratory experiments conducted to examine the question of EGCC formation. It is hypothesized that the interaction of the EGC with a large canyon that cuts across the shelf might be responsible for the observed formation of the EGCC as a current over the inner shelf, separating from the EGC at the shelfbreak. The results presented in this chapter suggest that, indeed, the splitting process may occur at the canyon, but the process depends critically on the stratification and strength of the EGC upstream of the canyon. Also, numerous other effects could be important to the formation process, including instabilities inherent in the current, winds, and tides: these are discussed briefly in this chapter, after a comparison of the laboratory results with their oceanic analogues.

Chapter 6 is a summary chapter, providing a synthesis of the four previous science chapters and highlighting the main scientific contributions of this thesis. A brief discussion of future work is also presented, followed by two appendices, and, finally, a bibliography for the entire thesis.

1.2 Background

Classically, the subpolar gyre circulation can be thought of as a broad, slow, poleward interior flow with an intense western boundary current flowing equatorward to balance mass, all driven by a positive wind stress curl in accordance with Sverdrup theory [*Pedlosky*, 1987]. In the North Atlantic, this wind-driven western boundary current is the East Greenland Current. However, tests to verify the Sverdrup balance are inherently difficult, especially considering the many other forces that influence the subpolar gyre circulation.

Farther north at Fram Strait, the East Greenland Current exits the Arctic Ocean as a buoyancy-driven current, carrying with it colder and fresher water from the Arctic at the surface, as well as sea ice, that flows along isobaths down the coast of Greenland. Fig. 1.1 illustrates the subpolar region of interest and shows a schematic of the main upper layer currents. The positive wind-stress curl of the Nordic Seas (Greenland, Iceland, and Norwegian Seas) drives a wind-driven component, adding a seasonally-varying, barotropic part to the EGC [Fig. 1.2, *Woodgate et al.,* 1999]. No significant interannual trend has been found in the EGC at either Fram Strait or Denmark Strait [*Fahrbach et al.*, 2001; *Woodgate et al.,* 1999], suggesting that the throughflows there are the predominantly buoyancy-driven parts of the flow, though there is a tendency for transports to increase during the winter.

The Denmark Strait area (Fig. 1.1) is a critical region for the subpolar gyre circulation, as well as for the global ocean circulation. It is here that a part of the deep western boundary current (DWBC) begins it initial descent, spilling over the sill of the Strait and entraining water, increasing its transport dramatically before continuing equatorward. Debate over what role the EGC plays in the DWBC formation continues [*Rudels et al.,* 2002; *Jonsson and Valdimarsson,* 2004], yet the Strait region also plays an important role in the upper layer circulation.

South of the Denmark Strait region the northward-flowing Irminger Current (IC), which carries Gulf Stream remnant water that is relatively warm and salty, splits in two, with the main part of the flow turning equatorward next to the EGC. This forms a sharp hydrographic front between the two water masses that is commonly observed in the area, yet by the latitude of Cape Farewell, the two currents are hard to identify in velocity structure alone (i.e. they merge at some point along the way). Mixing across the front, as well as instabilities of the EGC, drive intense water mass modification over the Greenland shelf area, and can bring Atlantic-origin waters up onto the inner shelf. This process may be responsible for the formation of intermediate waters that spill over the shelfbreak and form strong currents along the upper continental slope [*Pickart et al.*, 2005]. Eddies are also formed in the Denmark Strait region by the descending overflow [*Bruce*, 1995; *Spall and Price*, 1998], and these strongly influence the circulation over the shelf.

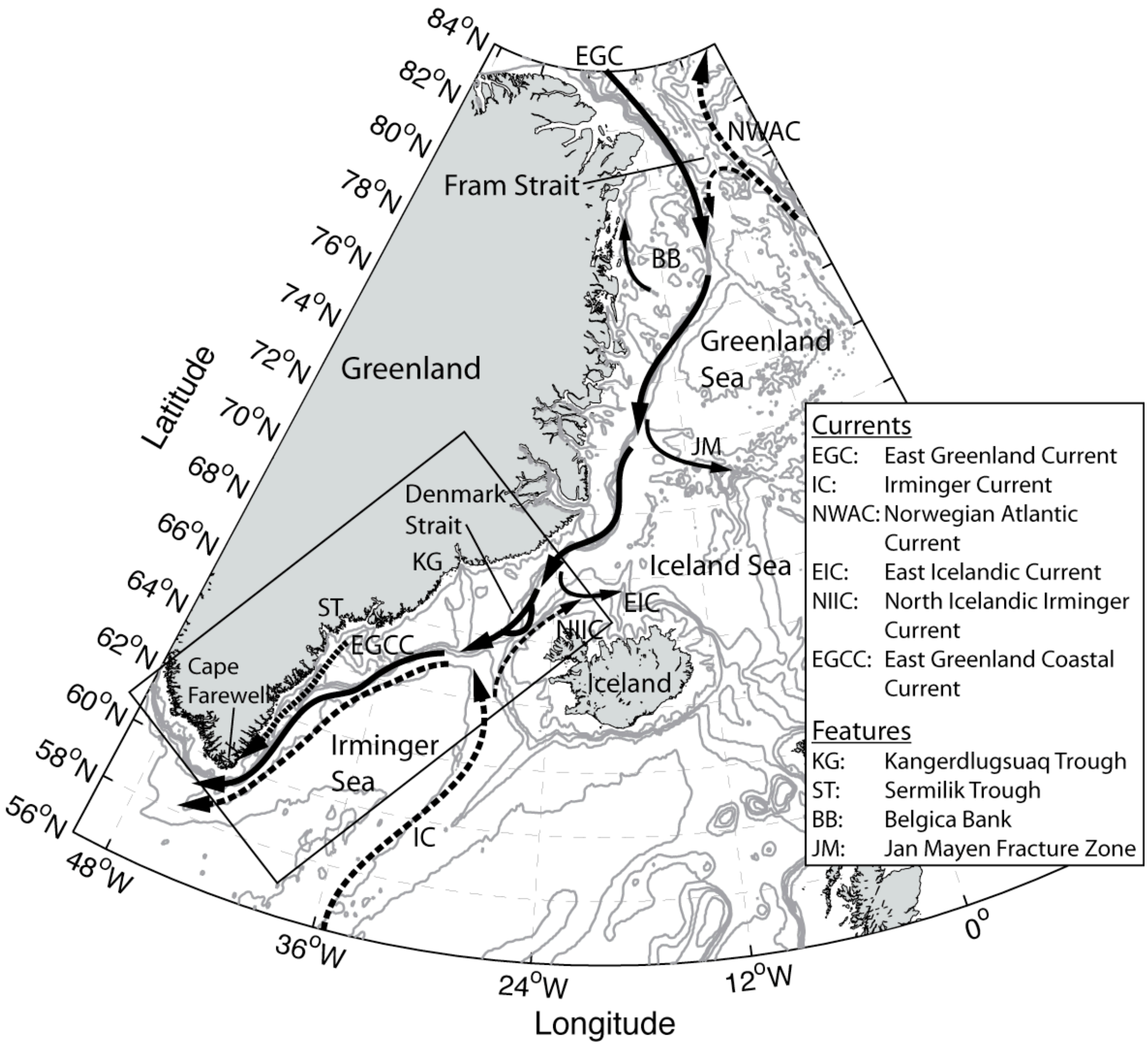

Figure 1.1. Regional map of part of the North Atlantic subpolar gyre showing a schematic of relevant upper layer currents, as well as bathymetric features and geographic names referred to in the thesis. Updating the circulation features in the boxed area is the focus of the remaining chapters in the thesis.

In addition to these oceanic processes, some mesoscale atmospheric processes (i.e. apart from the large-scale positive wind stress curl shown in Fig. 1.2. and the buoyancy-driven EGC) play an important role in the circulation of the Irminger Sea. These include barrier wind events, tip jets, and reverse tip jets, recently discussed by *Moore and Renfrew* [2005]. Not only do these winds provide local buoyancy loss that may lead to deep convection in the Irminger Sea [*Pickart et al.*, 2003], but the barrier winds can also affect the structure and strength of any potential coastal current along the southeast Greenland shelf, a concept discussed in detail throughout this thesis. Fig. 1.2 shows histograms of wind directions observed over one year (2004) at four latitudes along the southeast Greenland coast, illustrating the dominance of northeasterly winds to the north of Cape Farewell. These northeasterly winds are called barrier winds, and are set up by the damming of air against the high Greenland continent, which results in a geostrophic flow of air towards the southwest. The predominant winds at Cape Farewell are southwesterly, reflecting the frequent passage of low-pressure systems that pass the southern tip of Greenland along the North Atlantic storm track. The high variability of winds at Cape Farewell strongly influences the behavior of the shelf circulation and the coherence of any coastal current flow, an idea discussed further in Chapters 2 and 3 below. Fig. 1.2 also illustrates the small spatial scales of the winds in the subpolar gyre.

Despite the potential for these low-salinity currents to move offshore and affect wintertime deep convection in the Labrador and Irminger Seas, and their links to the interior flow and the DWBC system discussed above, the near-shore region of Greenland has remained poorly studied. Recently, however, there has been a renewed interest in the East Greenland shelf region, sparked by the important role that freshwater fluxes seem to play in controlling regional ocean circulation and, ultimately, global climate variability [e.g. *Bryan*, 1986; *Aagaard and Carmack*, 1989; *Curry et al.*, 2003].

The detailed mechanisms by which this freshwater is transported within the polar and subpolar seas remain unclear, as do the precise magnitudes of the freshwater flux. It is thought, though, that boundary currents such as the high-latitude buoyancy-driven Norwegian Coastal Current, or the Alaskan Coastal Current, play a significant role in regional freshwater budgets [*Mork*, 1981; *Weingartner et al.*, 2005]. How these coastal currents interact with the basin scale circulation, however, is also uncertain. The interaction of river plumes (typically thought of as smaller scale coastal currents) with the outer shelf ocean circulation has received more attention both observationally and theoretically [e.g. *Lentz and Largier*, 2006; *Yankovsky and Chapman*, 1997]. On subpolar shelves, freshwater is input not only from rivers but from melting sea ice, meltwater runoff from the mainland, and precipitation, resulting in coastal currents that are much larger scale than the individual river plumes [*Williams*, 2003; *Weingartner et al.,* 1999; *Fong et al.,* 1997].

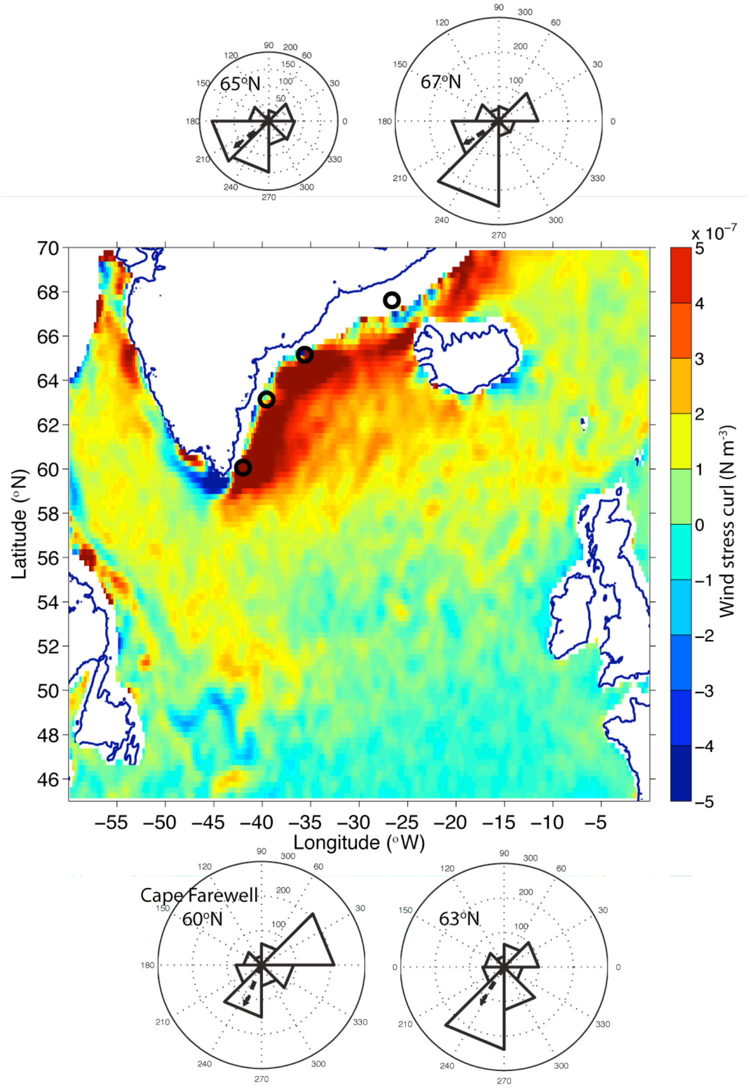

Figure 1.2. Annual average wind stress curl (N m^{-3}) taken from *Risien and Chelton* [2007, available online at *http://numbat.coas.oregonstate.edu/quikcow/*]. Black circles indicate positions for the wind roses. *(insets)* Histograms of wind directions at four latitudes (60ºN, 63ºN, 65ºN, 67ºN) over the southeast Greenland shelf for one year. Data come from twice-daily scatterometer winds observed by the QuikSCAT instrument [available online at *http://ssmi.com/qscat/qscat_browse.html*]. Dashed arrows point in the along-shelf direction for each latitude.

Before delving into previous research on the EGCC in particular, it is beneficial to give an overview of the upper layer circulation shown in Fig 1.1. More information can be found in the review by *Hansen and Osterhus* [2000], and a thorough discussion of the regional water masses is provided in Chapter 2.

In the region of southeast Greenland (boxed region in Fig. 1.1), the Arctic-origin, low-salinity East Greenland Current (EGC) flows southward next to the Atlantic-origin, high-salinity Irminger Current (IC) near the shelfbreak. The combined transport of the EGC, the IC, and the DWBC is one measure of the subpolar gyre strength, with previous estimates in the range of 27-36 Sv, where 1 Sverdrup = 10^6 m^3 s^{-1} [e.g. *Clarke*, 1984; *Bacon*, 1997; *Pickart, et al.* 2005]. North of Denmark Strait, the EGC transport has been estimated at ~27 Sv, partitioned into a wind-driven barotropic component of ~19 Sv and an 8 Sv baroclinic throughflow [*Woodgate et al.,* 1999]. The discrepancy between these numbers reflects the complexity of the region, with its many re-circulations, as well as the lack of direct measurements of velocity, since most studies use conservation of mass along with measured transport estimates to estimate regional volume budgets. An example of this complexity is given by *Holliday et al.* [2007], who showed evidence of a retroflecting part of the EGC as it passes Cape Farewell, which significantly alters the circulation picture for the EGC as it transitions into the West Greenland Current. This retroflection could also bring freshwater into the center of the subpolar gyre more efficiently, yet the behavior of the EGCC as it passes Cape Farewell is still an open question; one that is discussed in Chapters 5 and 6 below.

The study of *Bacon et al.* [2002, hereafter *B02*] focused attention back on the shelf, inshore of the EGC and IC. *B02* described a low salinity ($S \sim 32.5$) wedge of water trapped against the coast, reminiscent of previously observed high-latitude coastal currents. Using vessel-mounted acoustic Doppler current profiler data and two hydrographic stations southeast of Cape Farewell obtained during the summer of 1997, *B02* determined that the jet, which they named the East Greenland Coastal Current (EGCC), transported ~0.8 Sv. They suggested that this was mainly a seasonal feature resulting from coastal runoff. In 2001 the same feature was sampled with higher resolution hydrographic measurements and was reported to transport 2 Sv of water [*Pickart et al.,* 2005]. This volume flux was surprisingly large, on the same order of the 1-2 Sv carried by the EGC in the vicinity of Denmark Strait [*Hansen and Osterhus*, 2000]. Furthermore, using the data from the *Pickart et al.* [2005] study, the associated freshwater transport of the EGCC (referenced to a mean salinity of $S = 34.956$) was 57 mSv, almost 50% of the annual mean freshwater export from the Arctic Ocean through Fram Strait [*Aagaard and Carmack*, 1989]. Although this was a synoptic estimate, 57 mSv equals about four times the mean Alaska Coastal Current freshwater transport of 400 km^3 yr^{-1}, which constitutes a significant fraction of the freshwater entering the Arctic Ocean through Bering Strait [*Woodgate and Aagaard*, 2005].

Measurements of the EGCC prior to 1997 and 2001 are sparse in both time and space; the oldest that exist date back to the joint Icelandic-Norwegian cruises of the 1950's and 1960's reported by *Malmberg et al.* [1967]. Using geostrophic velocities referenced with current meter data from shelf moorings, they found a transport of 1.6 Sv for the EGCC, although they referred to it as the East Greenland Current [*Malmberg et al.*, 1967]. A recent review of these and other historical CTD data confirmed the presence of the EGCC along the southeast coast of Greenland [*Wilkinson and Bacon*, 2005; *Holliday et al.,* 2007]. When the surface 33.5 isohaline was used as a proxy, the EGCC appeared to follow the 500 m isobath closely [*Wilkinson and Bacon*, 2005]. However, low surface salinities do not necessarily represent solely the EGCC feature, but could suggest the presence of melting sea ice that occurs along the path of the EGC and IC. More recent drifter studies suggested a two-branched system on the East Greenland shelf with two distinct southward velocity cores: one located close to shore that is likely indicative of the EGCC, and the other at the shelf break presumably associated with the EGC and IC [*Reverdin et al.,* 2003; *Jakobsen et al.*, 2003]. These observations were based on very few drifters, however, all of which entered the shelf from the interior Irminger Sea south of Denmark Strait, presumably by wind drift or mixing.

1.3 Data

Despite the growing interest and the available historical data, many basic questions regarding the EGCC remain unsatisfactorily answered. This motivated a field program, undertaken in the summer of 2004, to investigate the EGCC south of Denmark Strait. It resulted in the first high-resolution survey of the coastal current (station spacing on the order of 5 km), carried out with the ice-strengthened vessel *RRS James Clark Ross*. The main goals of the cruise were to establish the existence of the coastal current, determine to what extent it was driven by coastal runoff (as surmised by *B02*), and obtain a basic description of its along-shelf evolution. The plan was to occupy a set of transects from Cape Farewell to Denmark Strait, which would enable investigation of the current's origin, evolution, dynamics, and importance to the regional freshwater system.

The 2004 cruise took place in the fourth and final year of a broader project entitled "Is Labrador Sea Water formed in the Irminger Basin?". The observations obtained in 2004 are the main source of data used in this thesis and are described in detail in Chapter 2. Additional sections occupied in the first three years of the project (2001 - 2003) are also used in Chapters 2 and 3, and provide some temporal context for the more extensive observations of 2004. This project fit into the larger scale aims of the Arctic-Subarctic Ocean Flux (ASOF) study, a multi-institutional, international collaboration focused on improving our understanding of the key fluxes between the Arctic and Atlantic Oceans. A basic understanding of these fluxes is needed in order to recognize any changes that may happen in a climate change scenario and to understand the forces that drive that variability.

Other sources of data are introduced as needed, and include satellite observations of sea ice concentration, wind records from the QuikSCAT scatterometer (both come from passive microwave instruments that penetrate through clouds), and a historical database of nutrient observations in the Denmark Strait region, among others.

Chapter 2

Hydrographic and velocity structure of the East Greenland Coastal Current

2.1 Introduction

The primary aim of this chapter is to provide the first detailed description of the EGCC in terms of its salinity, density, and velocity structure, both in the across-shelf and along-shelf directions. Historical records of the EGCC, of which there are few, commonly refer to the coastal current as the EGC, obfuscating the distinction between the two flows that will become apparent in this and subsequent chapters. An emphasis, then, is placed on objectively defining the EGCC when it can be distinguished from the EGC to elucidate discussion of when the two currents may actually interact more fully. The description of the EGCC in this chapter then leads to a deeper understanding of the primary forces controlling the behavior of the EGCC and its variability. Parts of this chapter come from *Sutherland and Pickart* [2007], with more discussion included here as well as a more detailed analysis of the θ/S structure of the EGCC and EGC (Fig. 2.15).

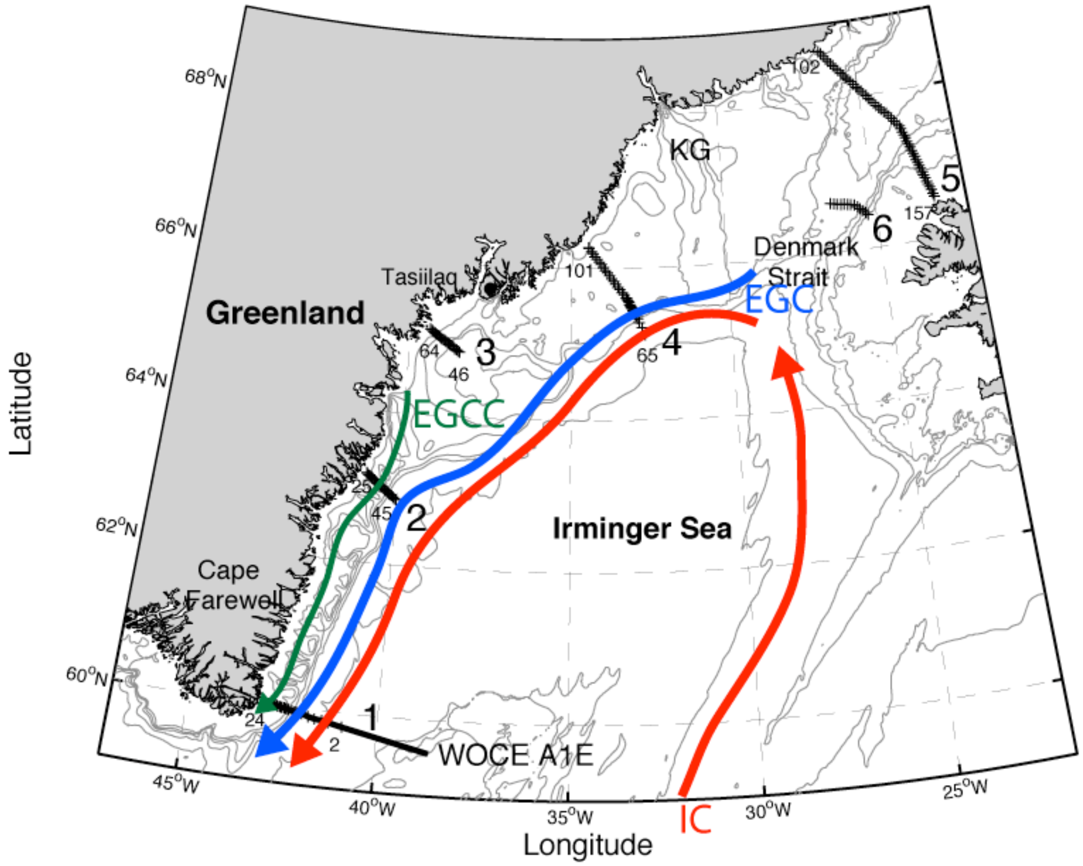

Figure 2.1. Map of JR105 station locations (+ symbols) and the WOCE A1E transect (solid line) off Cape Farewell. The 200, 350, 500, 1000, 2000, and 3000 m isobaths from the GEBCO bathymetric database are shown in light grey [*IOC et al.,* 2003]. Large numbers refer to JR105 sections, while the smaller numbers identify individual stations. KG denotes the location of the Kangerdlugssuaq Trough, while colored arrows denote the major upper layer currents schematically, similar to those in Fig. 1.1, but see Fig. 2.14 for an updated version of this circulation scheme.

2.2 Data and methods

The main source of data for this study comes from a July-August 2004 cruise on the ice-strengthened vessel *RRS James Clark Ross* (JR105) along the transects shown in Fig. 2.1. Six sections were occupied with a total of 170 hydrographic stations taken at high cross-stream resolution (3-5 km), with a Seabird 911+ conductivity/temperature/depth (CTD) system. Water to measure dissolved oxygen, salinity, and nutrient concentrations was obtained with a 12 x 10 liter bottle rosette. We used the salinity bottle samples to calibrate the CTD conductivity sensor (accuracies are 0.002 for salinity and 0.001°C for the temperature sensor), while the nutrient water samples were analyzed on board for nitrate (NO_3), phosphate (PO_4), and silicate (SiO_4) concentrations with a Technicon AutoAnalyzer. A shipboard thermosalinograph continuously recorded surface temperature and salinity along the ship track. Direct velocity measurements were obtained with a narrow-band, 150 KHz vessel-mounted acoustic Doppler current profiler (ADCP) that ran continuously during the cruise.

A key advantage of this data set is the high-resolution station spacing and the relative proximity to the coast of each inshore station (both on the order of 5 km). This represents the first oceanographic data set of its kind for the southeast Greenland inner shelf between Denmark Strait and Cape Farewell. We also have high-resolution data from transects taken in the summers of 2001-2003 by the *R/V Oceanus* (OC369 in 2001, OC380 in 2002, and OC395 in 2003) on the western end of the WOCE A1E repeat line off Cape Farewell (Fig. 2.1). These data were collected and processed identically to the JR105 data discussed here.

2.2.1 Hydrographic data processing

The CTD station data, consisting of salinity (S) and temperature (T), were pressure averaged to a resolution of 2 db. We then constructed vertical property sections by interpolating those data onto regular grids, with a resolution of 3 km in the horizontal and 10 m in the vertical, using a Laplacian-spline interpolation scheme. Potential density (σ_θ) and potential temperature (θ) fields, referenced to the sea surface, were constructed from the gridded sections at identical spacing.

Bottom depth profiles along the ship track were obtained from the ship's multibeam sonar system, except during times of rough sea state when the CTD altimeter data were used to determine the water depth at the station sites. Most CTD stations attained a maximum depth of less than 5 m from the bottom. The bottom profile for the portion of each section from the inshore-most station to the Greenland coast was interpolated from the General Bathymetric Chart of the Oceans (GEBCO) one-minute gridded bathymetric data set [*IOC et al.,* 2003].

2.2.2 Velocity data processing

The calculation of geostrophic velocities requires density differences that are available from the gridded σ_θ fields, but the main challenge is determining the reference velocity after integrating the vertical shear. This was done by using the concurrent direct velocity measurements taken by the shipboard ADCP, which introduced several additional processing steps. First, in order to reference geostrophic velocities to a suitable ADCP velocity, the effect of the tides and other ageostrophic motions in the ADCP data must be minimized. The barotropic tidal signal was estimated and subtracted out of the velocity data as part of the shipboard processing using the *Egbert et al.* [1994] tidal model (TPXO6.2). The model has shown good results in previous studies in this region [see *Torres and Mauritzen*, 2002; *Pickart et al.,* 2005]. Errors associated with the de-tiding procedure come largely from inaccuracies in the bathymetric data available for the Greenland shelf, so tidal velocities there may be biased by several cm/s [*Torres and Mauritzen*, 2002]. The high velocity of the currents we are studying, O(50 cm s^{-1}), gives us confidence that detiding errors will be insignificant; their contribution to error estimates for the transport values is discussed in Appendix A.

Second, although care was taken in trying to sample perpendicularly across the main jet features on the shelf and slope (whose mean path is expected to parallel the isobaths), maximum velocity vectors were sometimes oriented at an angle to the transect line. By rotating each velocity section into a streamwise coordinate system, a methodology originally developed for Gulf Stream studies, any bias associated with how the current changes its orientation with respect to the bottom bathymetry is minimized [*Halkin and Rossby*, 1985; *Fratantoni et al.*, 2001]. Such a coordinate transformation was applied to the JR105 ADCP data following the steps outlined by *Fratantoni et al.* [2001]. Care was taken to keep the observed jet features on the shelf (the EGCC) and over the slope (the EGC/IC system) separate in the analysis.

The de-tided and rotated ADCP velocities were interpolated onto the same regular grid as the hydrographic variables. Surface ADCP bins were excluded and the maximum depth of observations was 400 m off the shelf or 85% of the total bottom depth in water less than 400 m deep. Absolute geostrophic velocities in the alongstream direction, U_{abs}, were calculated by combining the geostrophic velocities, U_g, with the alongstream ADCP velocities, U_{adcp}. The method we used matches the average velocity of U_{adcp} and U_g over the depth range of available ADCP data at each horizontal grid point, such that

$$U_{abs}(x,z) = U_g(x,z) + U_{ref}(x) \tag{2.1}$$

where the reference velocity, U_{ref}, is defined to be

$$U_{ref}(x) = \frac{1}{h}\int_h U_{adcp}(x,z)dz - \frac{1}{h}\int_h U_g(x,z)dz \tag{2.2}$$

which equals the difference between the mean ADCP velocity and geostrophic velocity over the depth range h. In all of the JR105 sections, $U_{ref} \neq 0$, which implies that using solely the baroclinic velocities would inaccurately estimate the speed of both the EGCC and EGC. Throughout the rest of the paper, we refer to the alongstream absolute geostrophic velocity, U_{abs}, simply as velocity, and explicitly define other velocities as they are needed.

2.3 EGCC hydrographic and velocity structure

Several previous studies have documented the θ/S properties of waters near the East Greenland shelfbreak and their along-shelf evolution [e.g. *Krauss*, 1995; *Rudels et al.,* 2002]. On the offshore side of the EGC/IC system is a water mass historically referred to as Irminger Sea Water [*Clarke*, 1984] with approximate θ/S properties of 4-5°C and $S \sim 35$. This is believed to be a product of mixing between the EGC and IC, influenced as well from heat loss due to intense atmospheric forcing during the winter months. In the interior of the basin lies Northeast Atlantic Water, a Gulf Stream remnant water with $\theta > 7$°C and $S > 35$, that has undergone little modification since first entering the region along the Reykjanes Ridge as part of the northward-flowing Irminger Current. For simplicity, we combine the two Atlantic-influenced water masses into a single, saline Atlantic Water (AW) type identified in Fig. 2.2 with $\theta \sim 4.5$-6.5°C and $S \sim 34.8$-35.1.

The cold, low salinity waters near the shelfbreak and on the shelf originally derive from the Arctic and can be classified into three water masses: Polar Intermediate Water (PIW), Polar Surface Water (PSW), and warm Polar Surface Water (PSWw) [*Rudels et al.,* 2002]. PIW is the densest of these, defined as water with $\sigma_\theta > 27.70$ and $\theta < 0$°C that comes from the colder parts of the Arctic Ocean thermocline. PSW is lighter with $\sigma_\theta < 27.70$, but can be very cold, with $\theta < 0$°C. However, melting sea ice warms and freshens this PSW, which also warms slightly on its way south due to air-sea interaction. This transformed water mass, PSWw, can exhibit a range of θ/S properties depending on the processes modifying it, although in general PSWw is lighter than PSW and warmer than $\theta > 0$°C, as shown in Fig. 2.2.

2.3.1 Defining the EGCC

The main goal of this section is to provide an objective definition of the EGCC as a component of the Irminger Sea boundary current system. To accomplish this we utilize not only the θ/S properties and water masses described above, but we also present vertical sections of the hydrographic properties and velocity from JR105. We emphasize this descriptive aspect of the study since older studies, based on sparser data, could not consistently distinguish between the EGCC and the EGC.

We start with the EGC, where numerous definitions have been used in the past based on hydrography: *Pickart et al.,* [2005] used the 34.9 isohaline to distinguish the EGC from the IC, while *Nilsson et al.,* [2006] considered just the freshest part of the EGC using $S < 34.5$ as their EGC delimiter. Older studies also commonly looked at the freshest part of the EGC only ($S \sim 34$-34.9), if the current was distinguished from the IC at all [*Clarke*, 1984; *Krauss*, 1995]. In retrospect, some of these studies were probably sampling part of the EGCC and not recognizing its distinct nature from the EGC. Using these past studies as a guide, we use the 34.8 isohaline to mark the boundary between the EGC and IC.

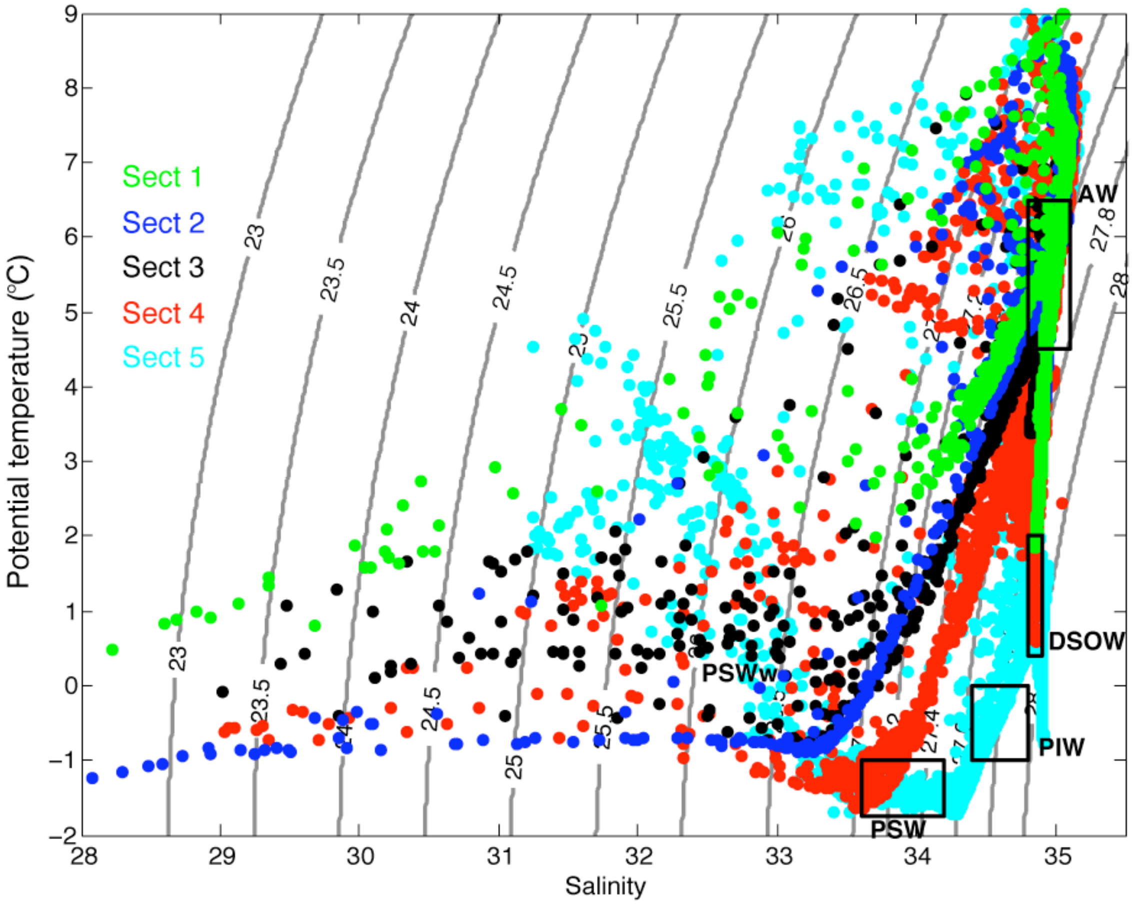

Figure 2.2. θ/S diagram for the entire JR105 data set indicating Irminger Sea and southeast Greenland shelf water mass definitions, which are Atlantic Water (AW), Polar Surface Water (PSW), Denmark Strait Overflow Water (DSOW), Polar Intermediate Water (PIW), and warm Polar Surface Water (PSWw). See text for discussion and specific water type property ranges.

Objectively defining the EGCC as a distinct feature from the EGC is a separate issue, since their salinity ranges can overlap. Thus, to distinguish the EGCC from the EGC in this study we use a combination of velocity and salinity criteria. Specifically, we define the horizontal limits of the EGCC by where the velocity decreases to 15% of the maximum inner jet velocity. This defines the width, W_{obs}, of the observed current, while the depth, h_{obs}, where the 34-isohaline intersects the bottom is taken as a vertical scale for the EGCC. For example, at Cape Farewell the EGCC is outlined by the inner green box in Fig. 2.3, which contains the 14 cm s^{-1} isotach that is 15% of the 95 cm s^{-1} maximum velocity observed. Defined this way, the EGCC has a width scale, w_{obs}, of 30 km and a depth scale, h_{obs}, of 75 m.

Similarly, the EGC is outlined by the outer green box that is drawn to satisfy the same velocity criteria used for the EGCC (in this case to capture the 9 cm s^{-1} isotach since the max velocity ~ 60 cm s^{-1}), and the salinity criteria $S < 34.8$. The boxes are meant only as guides to show where the salinity and velocity criteria are used to delineate the EGC from the IC and the EGCC. Transports and freshwater fluxes, as well as the depth and width scales of the two currents, are computed using the gridded data that satisfy these specific velocity and salinity criteria.

Vertical sections of salinity and velocity for all the JR105 transects, displayed in Fig. 2.3-2.7, are the best indicators of the current; these two fields are shown in relation to each other to illustrate the basic structure of the EGCC. Temperature, although an important identifier of water masses, plays a relatively small role in controlling the density of the upper-layer boundary currents in the subpolar region.

Discussion of the possible reasons for the differences in the hydrographic and velocity structure along the path of the EGCC is deferred until section 2.4 of this chapter, as is an explanation of the variability seen in the EGCC at Cape Farewell during the summers of 2001-2003.

2.3.2 Section 1 – Cape Farewell (60°N)

We start in the south at Cape Farewell to facilitate comparison with previous observations of the EGCC. Fig. 2.3*a* displays the salinity field and illustrates several important features. First, the strong front near stations 10-11 separating polar origin water and Atlantic-influenced high salinity water is the EGC/IC front, although the surface expression of the front is found 40 km farther offshore. The near vertical isohalines distinguish the AW, with $S > 34.8$ in the IC, from the EGC waters with $S < 34.8$. No PSW exists this far south, as it has been modified extensively along the path of the current becoming PSWw as shown in Fig. 2.2.

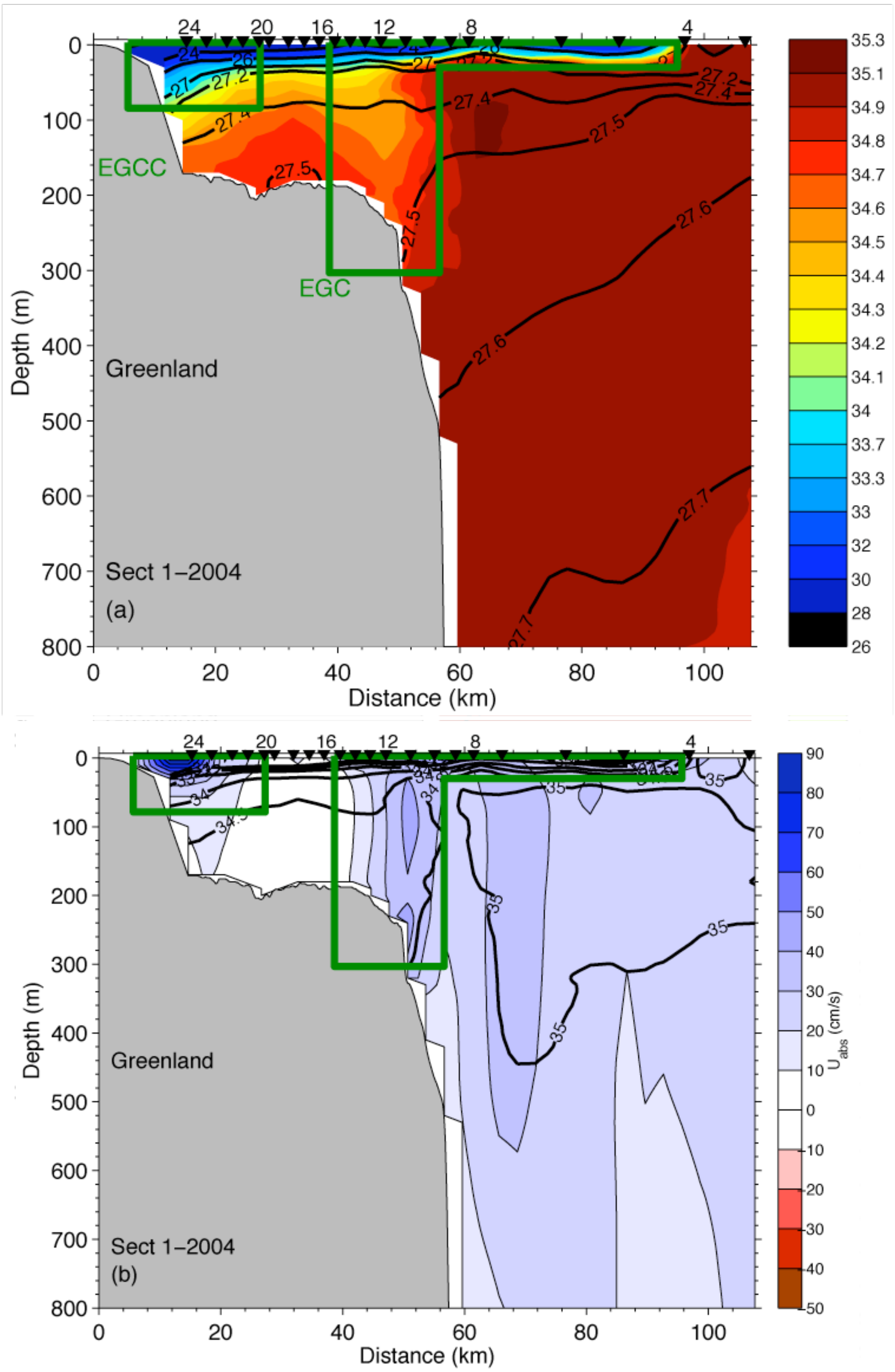

Figure 2.3. *(a)* Salinity field (color) from 2004 JR105 section 1 near Cape Farewell (60°N) with select isopycnals (kg m^{-3}) contoured in black. Boxes outline the boundaries defined in the text for the EGCC and the EGC. Black inverted triangles mark the numbered CTD stations. *(b)* Alongstream absolute velocity, U_{abs} (color, cm s^{-1}), for 2004 JR105 section 1 where $U_a > 0$ denotes equatorward flow. The isohalines (34, 34.5, 34.8, and 35) used in defining the currents are contoured in black.

Inshore of station 20, a very fresh wedge of water, $S < 32$, lies over the shelf roughly 20 km shoreward of the EGC/IC front. This is the front associated with the EGCC. The 34-isohaline descends to a depth (h_{obs}) of about 75 m at the coast, which is much shallower than observed in 2001 when $h_{obs} \approx 110$ m (Pickart, et al. 2005), or in 1997 where observations showed no water with $S > 34$ at the innermost CTD station (B02). Another feature seen only in 2004 is the low-salinity surface waters that extend out from the shelfbreak with an average depth of about 10 m. This is roughly the mixed layer depth (computed where $\sigma_\theta - \sigma_{\theta,surface} > 0.125$ kg m^{-3}), which varies in the shelf region from 6-10 m, suggesting the important influence of wind and/or other mixing processes to the EGCC and EGC. This feature also implies that using surface hydrographic or satellite data to infer the position of the EGCC can be misleading, since in this case the 34-isohaline outcrops almost 100 km from the coast, while the two currents are actually found much closer inshore. Mixed layer depth estimates in the region just offshore (east of station 4) of this fresh, surface cap are much deeper and average about 60 m.

The absolute geostrophic velocity section shown in Fig. 2.3*b* supports the salinity section in distinguishing the EGC from the EGCC. Associated with the low salinity wedge on the inner shelf, a distinct jet is observed with maximum velocities > 90 cm s^{-1} and significant alongstream flow throughout the water column. Note that we did not cross the entire current, so that extrapolation was necessary to obtain volume and freshwater transport values of the EGCC at this location (see below). A region of near-zero velocity separates the EGCC from the high velocity EGC core centered near the salinity front at station 11. Offshore of the EGC near station 7 is a deep-reaching velocity core that likely corresponds to the IC. In previous studies, the IC and EGC were reported as a merged system in velocity, though they were easily distinguished in θ/S space [*Pickart et al.,* 2005]. In 2004, however, the two currents are distinct in their velocity signals as well.

2.3.3 Section 2 – near 63° N

Section 2 is located approximately 350 km to the north on the narrowest part of the southeast Greenland shelf at 63°N (Fig. 2.1). Again, a wedge of fresh water dominates the salinity structure in Fig. 2.4*a* over the shelf, although it is much deeper at the coast ($h_{obs} \approx 200$ m) than the wedge seen at Cape Farewell. The water found here contains a stronger core of modified PSW, with the freshest water shown in Fig. 2.2 much colder, $\theta < 0$°C, than at section 1. The influence of warm, salty water is still present though, with the eroded PSW core on a mixing line with AW. The EGC/IC front on this section is located near stations 37-38. Inshore of this front, mixed layer depths are deeper than observed at section 1, ranging from 10 - 20 m, possibly in response to the stronger wind forcing that occurred during the occupation of this transect, but still shallower than offshore of station 40 where the average mixed layer depth is ~50 m.

Associated with the sloping isohalines of the low salinity water on the shelf is a strong velocity signal (Fig. 2.4*b*) with maximum values near the surface exceeding 100 cm s^{-1} and near-bottom values up to 30 cm s^{-1}. Using the velocity and salinity criteria for defining the EGCC, we find that the majority of the flow found at this section is identified as part of the coastal current, shown in Fig. 2.4*b* (inner green box).

Near the shelfbreak it is difficult to isolate the EGC (compared to the distinct EGC seen farther south in Fig. 2.3*b*). The confusion in nomenclature between the EGCC and EGC is most evident here, since many previous investigators would call the observed flow at section 2 the EGC, while we reserve that for the shelfbreak portion alone. Bathymetry may play a part in this as the shelf is very narrow here (about 40 km wide versus > 100 km farther north), thus bringing the EGC and EGCC flows in close proximity. This may also explain why the velocities measured at section 2 are so large (the largest observed during the survey). We address the distinction between the EGCC and EGC later in this chapter, as well as the reason for the large velocities observed at this location.

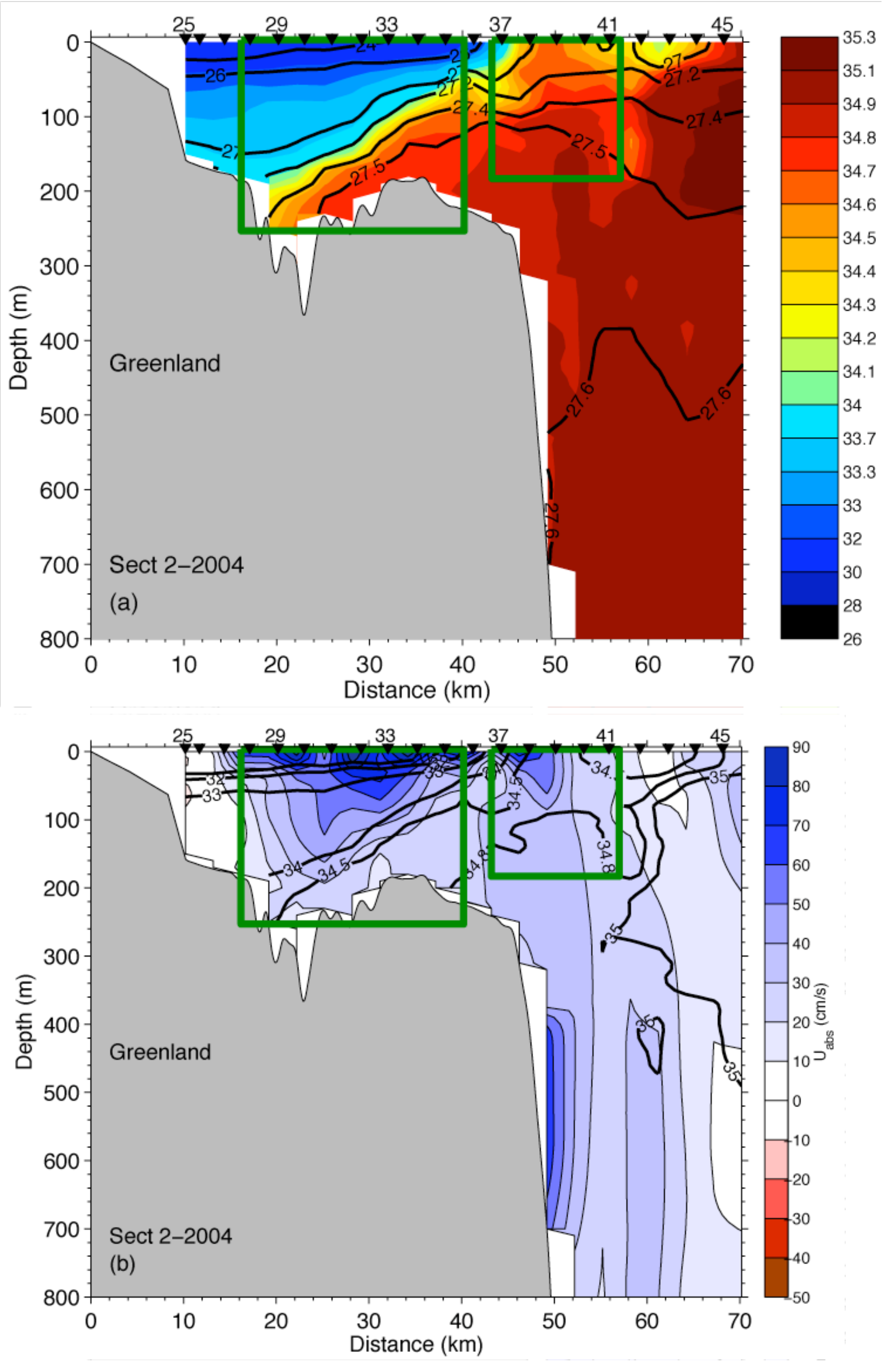

Figure 2.4. Same as Fig. 2.3, except for 2004 JR105 section 2, which is near 63°N.

2.3.4 Section 3 – near 65° N

At this latitude the shelf contains an 800 m deep basin, and the JR105 section sampled only the inshore part of this basin (which extends very close to the coast), missing any shelfbreak flow. This implies that the current observed at section 3 is exclusively the EGCC. However the bathymetric influence of the basin extends out to the shelfbreak, so that a portion of the EGC could be diverted inshore around the basin. This notion is supported by studies showing southward-directed drifter tracks on both sides of the basin [*Reverdin et al.,* 2003; *Jakobsen et al.,* 2003].

As in the sections to the south, we observed a fresh wedge of water at section 3, indicative of the EGCC. The freshest water shown in Fig. 2.5*a* is again the coldest, falling in the PSWw regime, although, unexpectedly, it is warmer than observed at section 2 as seen in Fig. 2.2. Another surprise is the presence of salty water, $S > 34.8$, found occupying the majority of the subsurface water column near station 46, far inshore of the shelfbreak. This is also suggestive of flow diverting from the shelfbreak around the basin and bringing with it AW influence from the EGC/IC system, a notion supported by the thermosalinograph data in Fig. 2.8.

The velocity data in Fig. 2.5*b* display a surface intensified jet with maximum velocities near 60 cm s^{-1}. At this location the EGCC is over 300 m deep and 30 km wide, although the 34-isohaline intersects the bottom near 150 m, which is comparable to other sections. Another notable feature in Fig. 2.5*b* is the subsurface velocity maximum observed on the western edge of the basin near station 48. This might represent a deep cyclonic circulation around the basin, although it is uncertain since the other side of the basin lies outside of our station data.

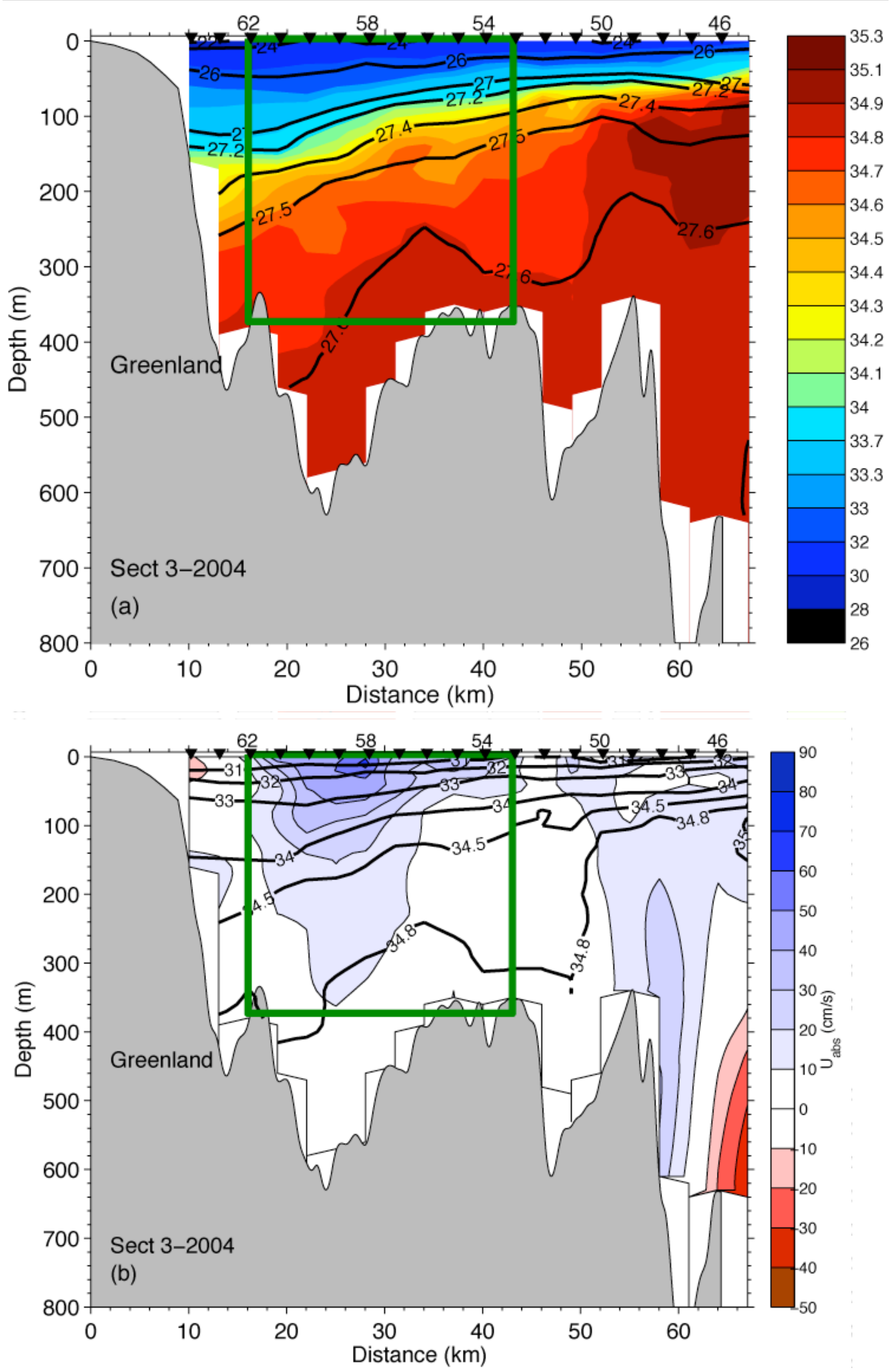

Figure 2.5. Same as Fig. 2.3, except for 2004 JR105 section 3, which is near 65°N.

2.3.5 Section 4 – near 66° N

Section 4, which lies north of Tasiilaq where the shelf reaches its widest point, is the closest the JR105 data come to the area covered historically by *Malmberg et al.* [1967] and more recently by *Nilsson et al.* [2006]. Fig. 2.6*a* displays the observed salinity field that has a large wedge of fresh water with $S < 34$ occupying a good portion of the 100 km wide shelf down to a depth of 150 m. Some fresh water also resides in the vicinity of the shelf break, yet the dominant features there are the two lenses of salty water, $S > 34.8$ (centered at stations 73 and 79 respectively), likely associated with AW eddies originating from the IC. Such features have been observed previously [*Rudels et al.,* 2002; *Pickart et al.,* 2005] and represent a source of AW influence reaching onto the shelf. If these features mix isopycnally, the salty influence will extend beneath the fresh wedge and modify the subsurface waters of the shelf. Eddy activity at this latitude has been observed in drifter studies as well [*Krauss*, 1995], suggesting that warm, salty intrusions onto the shelf are common in this region.

The θ/S characteristics of the water at section 4 (Fig. 2.2) indicate the presence of pure PSW, some modified PSWw, and a strong AW influence. Also note the densest water here is similar to Denmark Strait Overflow Water (DSOW, see Fig. 2.2), a dense water mass with $\sigma_\theta > 27.8$, $\theta > 0°\text{C}$ and $S \sim 34.8\text{-}34.9$. This dense water signature comes from two sources; one obviously is the DSOW itself, as we sampled deep enough to catch some of the DWBC along the Greenland slope. The other source is from the recently described East Greenland Spill Jet that forms from dense water spilling off the shelf, originally discovered at this same location [*Pickart et al.,* 2005].

The freshest and coldest water is located on the inner shelf, shoreward of station 93, where the low salinity wedge attains its maximum depth. Coincident with this deepening is a surface-intensified jet (Fig. 2.6*b*). In this sub-wedge, salinities are < 32 and the maximum velocity is ~ 60 cm s^{-1}. This is the EGCC and it is separated spatially from the shelfbreak flow. The previous studies of *Malmberg et al.* [1967] and *Nilsson et al.* [2006] sampled only sparsely near this location, and consequently resolved only the large-scale signature of the fresh wedge of water.

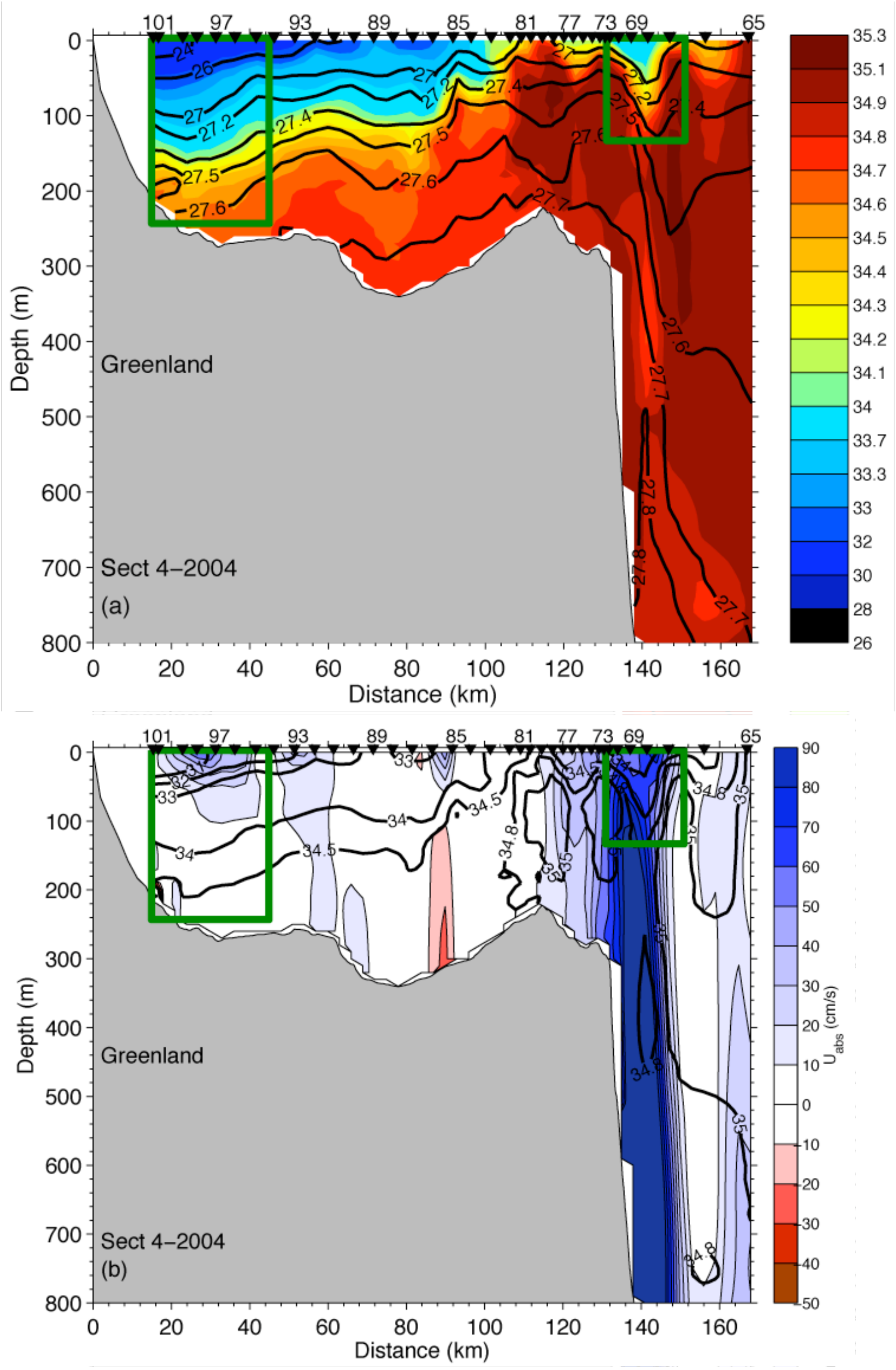

Figure 2.6. Same as Fig. 2.3, except for 2004 JR105 section 4, which is near 66°N.

Both studies referred to the corresponding flow as the EGC, while in fact with tighter station spacing and closer proximity to the coast, we find that the EGCC exists even this far north. Note that the seaward edge of the fresh water wedge, defined by the outcropping of the 34-isohaline near station 83, is not associated with a strong jet (Fig. 2.6*b*). This is another example of the care one must take when considering only surface data to describe the EGCC. In this section there is actually weak flow associated with most of the fresh wedge.

By contrast, the EGC is confined to a shallow depth near the shelfbreak, centered near station 69 in Fig. 2.6*b*, and adjacent to the salty lenses noted above in the salinity field. The strongest flow observed near the shelfbreak actually resides just over the slope centered at a depth of 500 m near station 69; this flow is identified as the East Greenland Spill Jet previously described by *Pickart et al.* [2005] at this exact location. The subsurface velocity maximum in Fig. 2.4*b* on the upper slope is likely a spill jet remnant as well. The IC is usually observed at this latitude; we assume its absence is due to the limited offshore extent of the transect and the presence of the strong spill jet feature.

2.3.6 Section 5 – north of Denmark Strait (68° N)

Section 5 was occupied north of Denmark Strait, extending from the Greenland coast to the Icelandic coast; however, the focus here is on the northwestern portion of the transect only. The dominant feature of the salinity field in Fig. 2.7*a* is the EGC front located near station 128. The isohalines descend about 200 m indicating the presence of the EGC in the middle of the basin upstream of Denmark Strait. The fact that the EGC is situated far offshore of the shelfbreak is not uncommon at this latitude; it has been observed detached from the shelfbreak previously and can re-attach downstream of the strait [*Rudels et al.,* 2002; also see discussion in Chapter 4]. Water with potential density $\sigma_\theta > 27.8$ kg m^{-3} is usually associated with DSOW. On the Greenland side of the EGC front, the water is lighter than this to about 300 m depth, indicating the presence of Arctic-origin surface waters. Farther south at section 4, this isopycnal is situated off the slope near the sill depth of Denmark Strait (~ 600 m) in Fig. 2.6*a.* Unmodified PSW and PIW exist at section 5, corroborated by the θ/S characteristics displayed in Fig. 2.2*a*. The water lying in the AW area actually comes from the Icelandic Irminger Current flowing to the north adjacent to the Icelandic coast (not shown in Fig. 2.7).

Interestingly, even though the upper layer is fresh between the Greenland coast and the EGC front, there is no pronounced wedge akin to the sections farther south. Rather, there is only a slight overall tilt to the 34-isohaline from the EGC front towards Greenland to station 108. Embedded within this tilt is a small region of enhanced thermal wind shear and a weak maximum in velocity centered near station 114 (Fig. 2.7*b*). We take the EGCC to be the flow contained within the inner green box in Fig. 2.7*b*, which has velocities up to 30 cm s^{-1} and reaches a depth of 200 m.

By contrast, the EGC signature is very strong at this section, with a surface intensified expression having velocities up to 60 cm s^{-1}. Note the bowl-shaped structure of the deep isopycnals between stations 118 and 130. This corresponds to a recirculation over the deep basin with poleward flow on the western side of the outer green box. Whether or not this is a permanent feature is unknown, but it is clear that at the time of the survey not all of the observed EGC jet continued equatorward. Accordingly, we include the poleward part of the flow in defining the EGC and limit its depth extent to water with $\sigma_\theta < 27.8$ kg m^{-3}, excluding any DSOW water.

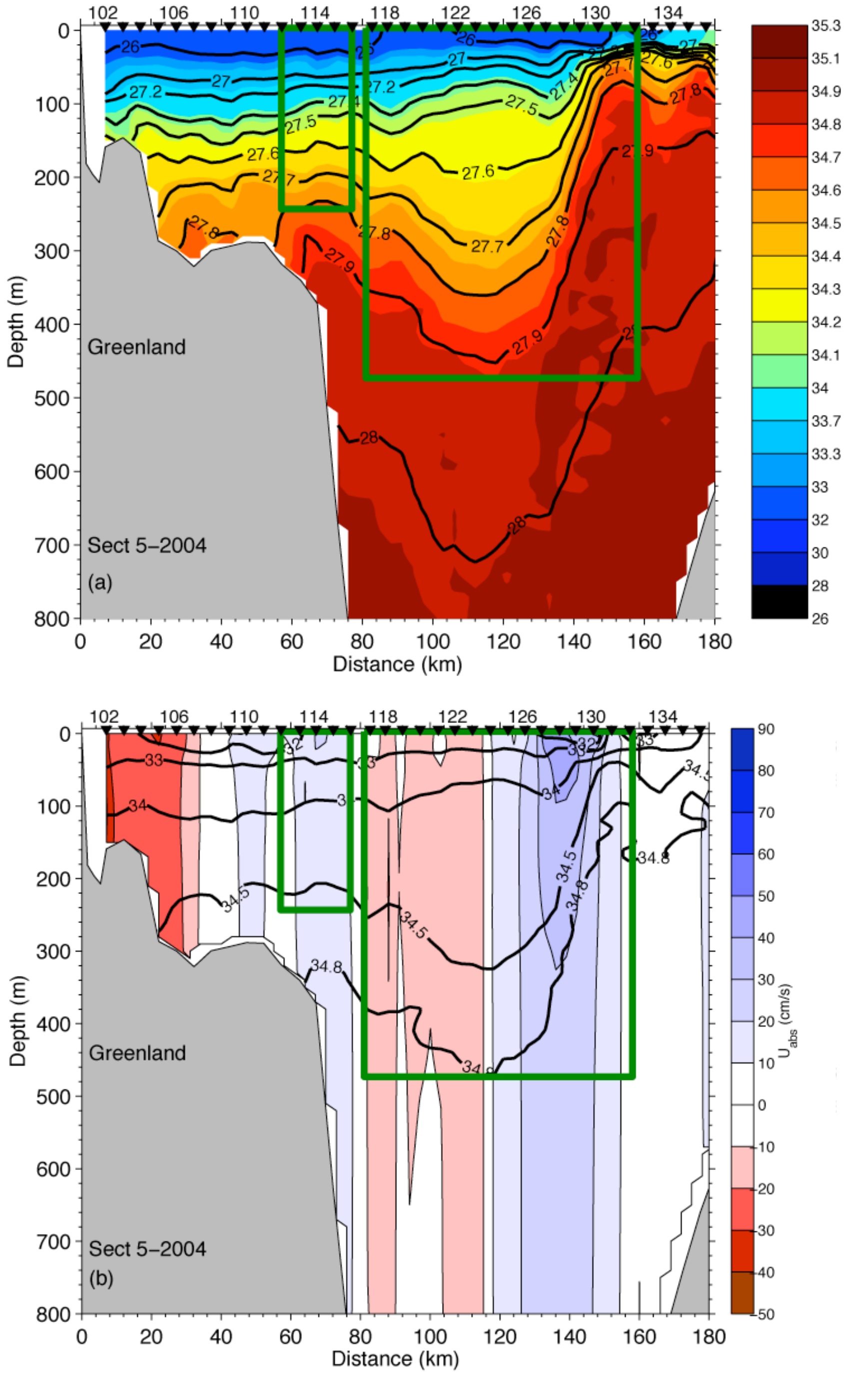

Figure 2.7. Same as Fig. 2.3*a*, except for 2004 JR105 section 5, which is near 68°N.

2.4 Sources of variability in the EGCC

As noted earlier, we observed a very fresh, $S < 32.5$, surface layer of water extending 100 km from the Greenland coast (Fig. 2.3*a*) in the JR105 CTD transect near Cape Farewell. This feature is present as well in the thermosalinograph data collected during the occupation of the transect (Fig. 2.8, discussed below). However, the ship made additional crossings of the shelf and shelfbreak in the vicinity of Cape Farewell during the mooring work offshore, and the thermosalinograph data from six days before the CTD transect shows that the $S < 32.5$ water was confined closer to the coast inshore of the shelfbreak. One possible explanation for this, as well as for the alongstream variability in the volume transport estimates (presented below in Chapter 3), is forcing by the wind, in particular the along-shelf wind stress, τ_{along}. Fortunately, we can investigate the role of time varying τ_{along} on the EGCC at Cape Farewell since data were obtained in the three previous summers (2001-2003) during our field program, as well as in summer 1997 [*B02*].

Other possible mechanisms that can explain the observed variability include the influence of the irregular shelf bathymetry off southeast Greenland, as well as internal variability due to nonlinear processes and instabilities of the current itself. The bathymetric process is discussed briefly in Section 2.5 and is the main topic of Chapter 5, while the effects of nonlinearities on the EGCC is investigated in Section 2.4.3.

2.4.1 Dynamical scales of the coastal current

Numerous theoretical and observational studies have shown that along-shelf winds can affect a buoyant coastal current through an "Ekman-straining" mechanism [e.g. *Fong and Geyer*, 2001; *Lentz and Largier*, 2006]. Downwelling favorable winds steepen the front, tending to deepen and narrow the current as well as induce a barotropic velocity and reduce stratification within the current. Upwelling favorable winds shoal the foot of the front and widen the current through a thin mixed layer that moves offshore at a velocity that scales with the Ekman velocity. Theoretical estimates exist for the depth of the foot of the front, $h_p = (2Qf/g')^{1/2}$, and the width of the current, $W_p = (g' h_p)^{1/2}/f + W_b$, where Q is the transport of the current, f is the Coriolis parameter, g' is the reduced gravity, and

W_b is distance from the foot of the front to the coast [*Yankovsky and Chapman*, 1997]. These estimates have been tested for smaller scale coastal currents, but never for a large-scale flow such as the EGCC.

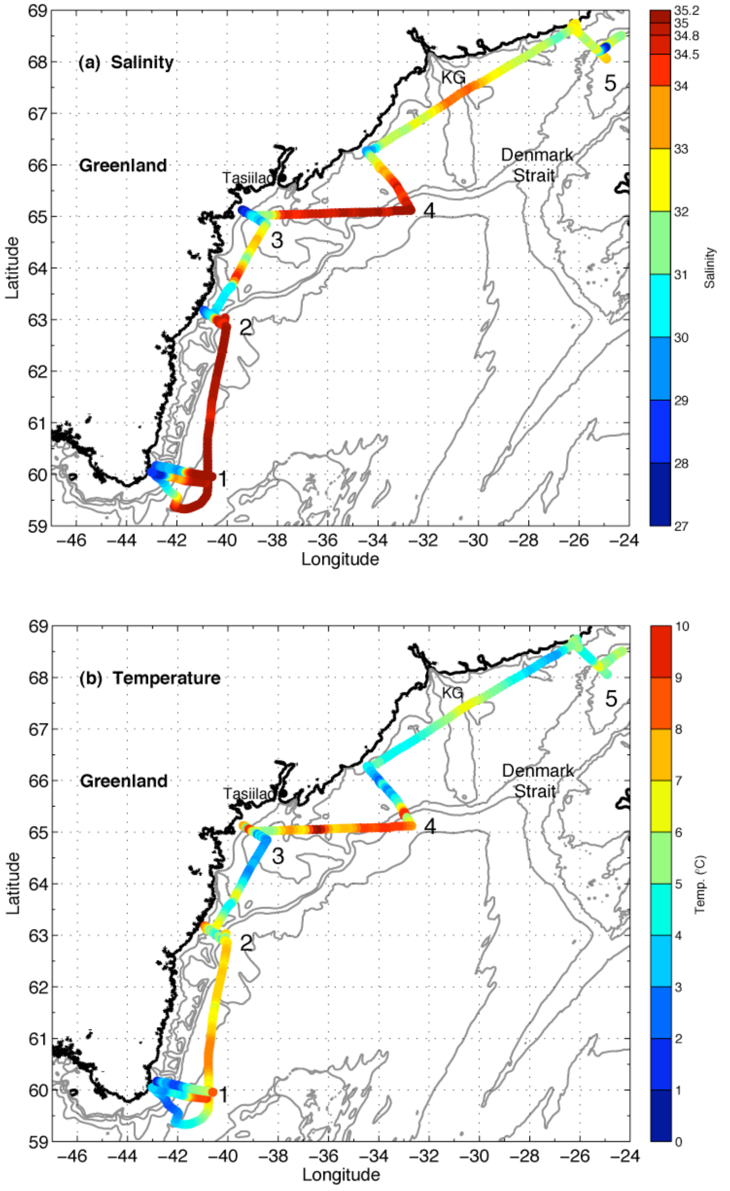

Figure 2.8. *(a)* Surface salinity field, *S*, from thermosalinograph data taken during JR105. The two lines near Cape Farewell are offset to allow visualization; one was taken during the CTD station work, while the other was taken during mooring deployments that preceded the CTD transects. *(b)* Surface temperature field, *T* (°C), from thermosalinograph data taken during JR105.

It is also useful to determine if a buoyant coastal current is “surface-trapped” or “slope-controlled”. The former implies that the current is not influenced significantly by the bottom and may be more susceptible to the wind, while the latter suggests that bottom friction and bottom boundary layers play a large role in controlling the current. Previous studies have also attempted to separate the wind-driven and buoyancy-driven components of a coastal current by defining a wind strength index, $W_s = u_{wind} / u_{buoy}$ [*Whitney and Garvine*, 2005]. W_s compares the wind-driven and buoyancy-driven along-shelf velocity scales. If $|W_s| < 1$, the flow is in a buoyancy-driven state, while for $|W_s| > 1$, strong wind events dominate the flow. These scales are defined and discussed below in Section 2.4.2 with application to the EGCC.

We now test these theoretical ideas with the observations of the EGCC along-shelf flow at Cape Farewell. To be complete, we first display the salinity and alongstream velocity sections at Cape Farewell from 2001-2003 in Figs. 2.9-2.11. They are presented identically to the JR105 sections above.

Table 2.1. The observed depths and widths of the EGCC defined in the text, h_{obs} and W_{obs}, along with A_{on} / A_{off} for each secton.

Section	h_{obs} (m)	W_{obs} (km)	A_{on} / A_{off}
1	75	30	0.18
2	190	24	0.6
3	150	27	0.1
4	110	30	0.02
5	110	20	N/A
1 (2001)	100	28	0.14
1 (2002)	140	24	0.11
1 (2003)	65	21	0.09
1 (1997[a])	110	24	N/A

[a] The 1997 estimates are from Bacon, et al. (2002).

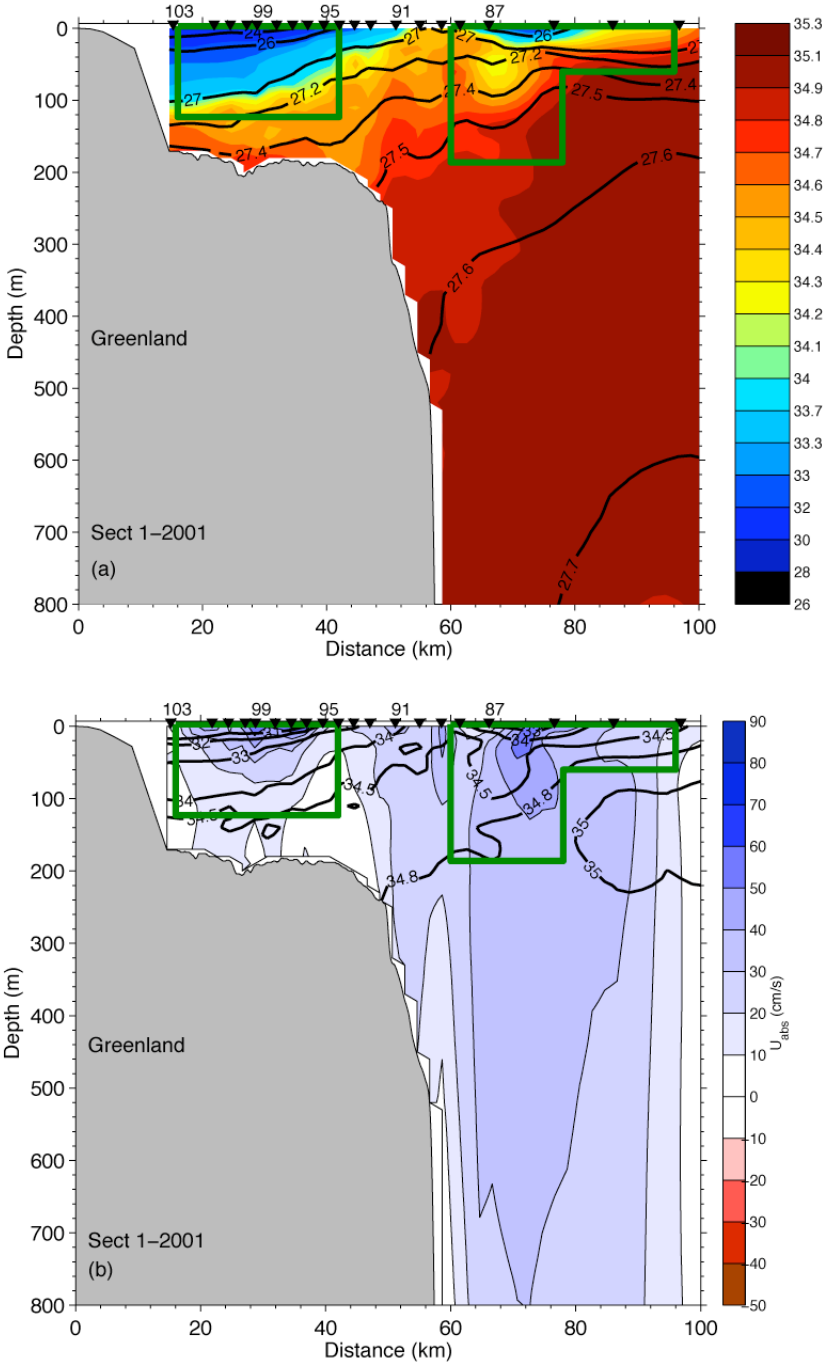

Figure 2.9. Same as Fig. 2.3, except taken in 2001 (OC369) near 60°N at Cape Farewell.

The first feature to note in comparing the different years' salinity fields at Cape Farewell is the pronounced variability in the depth of the 34-isohaline, which is used to delineate the EGCC front. The depth, h_{obs}, where this isohaline intersects the bottom is listed in Table 2.1 (including the 2004 value, Fig. 2.3). In 2003 $h_{obs} = 65$ m, its shallowest position in all years, while in 2002 $h_{obs} = 140$ m. Overall, however, it appears that in the years 2001-2004, the EGCC at Cape Farewell was a surface-trapped buoyant current, at least in summer. To demonstrate this we compare the area of the current located offshore of the foot of the front to the area onshore, following *Lentz and Largier* [2006]. Taking the 34-isohaline as an indicator of the frontal position, the ratio of onshore area to offshore area, A_{on} / A_{off} is << 1 for each section, as listed in Table 2.1. However, note the 2003 alongstream velocity in Fig. 2.11*b* is above zero near bottom and is not contained within the low-salinity wedge that other years' observations have suggested. Even if the 34.5 isohaline is used to capture more of the current in 2003, the ratio A_{on} / A_{off} is still < 1 (and this holds for the other years also), indicating that the current is surface-trapped. We will see in the next section that the bottom may play a bigger role farther north, as this ratio varies along-shelf.

To investigate further the time variability of the EGCC at Cape Farewell, we estimate h_p and w_p using the computed alongstream transports, Q_a (see Chapter 3), reduced gravities, g', and the observed distances from the foot of the front to the coast, w_b. Ratios of the observed depth and widths of the EGCC (h_{obs} and W_{obs} as defined in Section 2.3.1) with the predicted depth and width scales all lie in the range 1-2 (see Table 2.2), with the 2003 data being the one exception below one. Note that in 2003 the depth of the 34-isohaline was shallow, although the equatorward flow extended much deeper (Fig. 2.11), which is why the predicted depth scale is greater than the observed. Overall, however, the predicted scales match the observations quite well, suggesting that the dynamics of the EGCC may be appropriately described by the theoretical ideas developed previously for smaller scale buoyant flows.

Table 2.2. Ratios of the observed depth and width scales of the EGCC to theoretical scales, along-shelf wind stresses, and reduced gravities at Cape Farewell (JR105 section 1) from summer 1997, and 2001-2004. The scales are defined in the text, as is the wind strength index, W_s.

Year	h_{obs} / h_p	W_{obs} / W_p	$\tau_{along}{}^{b}$ (N/m^2)	g' (m/s^2)	W_s
1997 (B02)	1.5	1.4	-0.027	0.038	-0.07
2001 (OC369)	1.4	1.1	-0.011	0.045	-0.13
2002 (OC380)	2.1	0.9	-0.016	0.055	-0.02
2003 (OC395)	0.6	0.9	-0.013	0.012	-0.50
2004 (JR105)	1.4	1.2	+0.022	0.045	0.15
2004 (JR105[a])	1.7	1.8	+0.026	0.045	0.09
2004 (JR105[a])	1.9	1.1	-0.010	0.045	0.03

[a] These data are based only on ADCP sections from crossings at Cape Farewell during JR105.

[b] Along-shelf wind stresses are 2-day averages, where $\tau_{along} < 0$ is downwelling favorable.

Table 2.3. Same as Table 2.2, but for the EGCC at sections north of Cape Farewell in 2004 (JR105).

Section	h_{obs} / h_p	W_{obs} / W_p	τ_{along} (N/m^2)	g' (m/s^2)	W_s
2 (63°N)	1.4	0.7	-0.028	0.037	-0.25
3 (65°N)	1.4	1.1	-0.008	0.037	-0.05
4 (66°N)	1.1	1.7	+0.012	0.037	0.13
5 (68°N)	N/A[a]	N/A[a]	+0.070	N/A[a]	0.25

[a] No estimates were made at this section due to the weak EGCC structure observed.

The transects north of Cape Farewell also behave qualitatively akin to what is expected. The ratios of observed depths (h_{obs}) and widths (W_{obs}) of the EGCC to the predicted scales, h_p and w_p, are all O(1) as listed in Table 2.3. The most notable differences in the EGCC along the shelf arise at section 2, where the EGCC is relatively more slope-controlled: the ratio $A_{on} / A_{off} \approx 1$, compared to $A_{on} / A_{off} << 1$ at all other JR105 locations (excluding section 5, see Table 2.1). Overall though, the EGCC appears to be a surface-trapped current. The EGC, however, can vary from surface-trapped to slope-controlled; this idea is discussed more in Chapter 5 when the laboratory results are applied to the EGC and EGCC system.

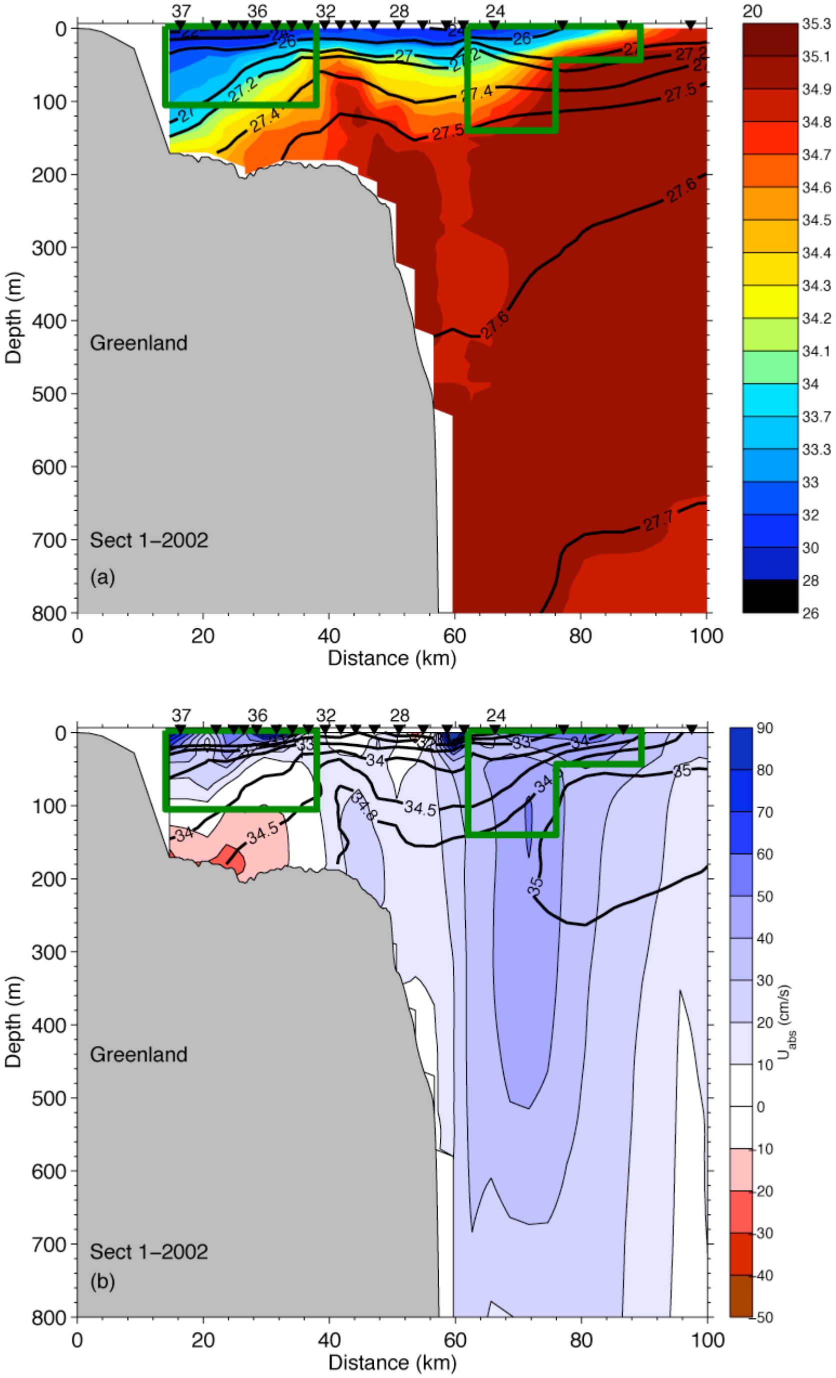

Figure 2.10. Same as Fig. 2.3, except taken in 2002 (OC380) near 60°N at Cape Farewell.

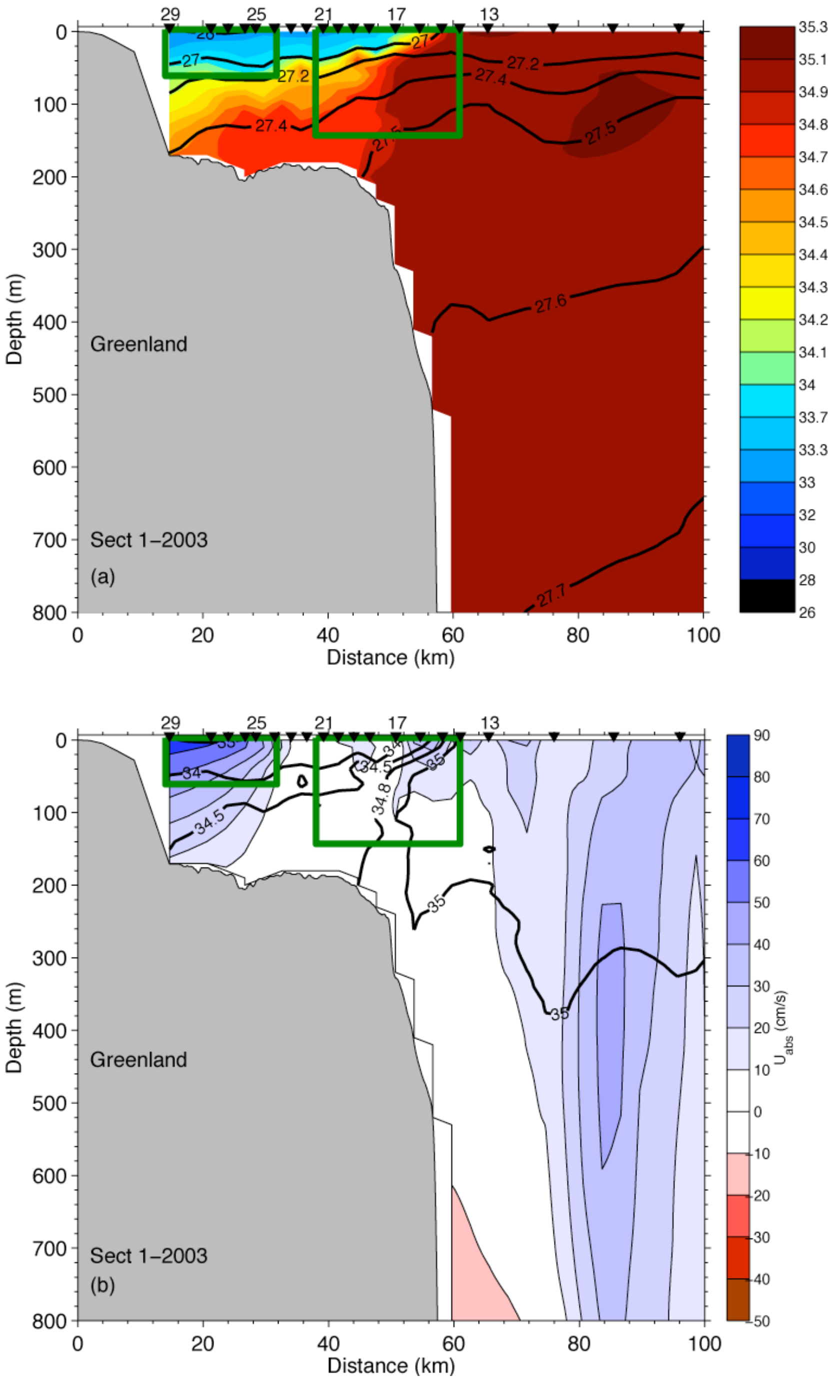

Figure 2.11. Same as Fig. 2.3, except taken in 2003 (OC395) near 60°N at Cape Farewell.

2.4.2 Wind forcing

To begin looking at the role of the wind on forcing the EGCC, we regress τ_{along} versus four variables: the observed depth (h_{obs}) and width (w_{obs}) scales of the EGCC, and the absolute volume and freshwater fluxes for each year. The volume and freshwater fluxes are calculated in the next chapter, but are used here for completeness. These variables, which all come from the summertime data collected near Cape Farewell during the years 1997-2004 described above, are plotted against τ_{along} in Fig. 2.12 and Fig. 2.13, respectively. Wind stresses were calculated from the twice-daily QuikSCAT scatterometer wind fields using a drag formula [*Large and Pond*, 1981], and rotated into along- and cross-shelf components. We define τ_{along} as an average over the two days prior to the time of completion of the CTD section. This averaging time scale was chosen for several reasons. First, the CTD sections generally took 1-2 days to complete. Second, two days is the amount of time it would take an offshore Ekman flux driven by a 0.1 N m^{-2} wind stress to move the entire area of water present on the shelf near Cape Farewell off of the shelf. Essentially, this timescale is equivalent to the wind strain timescale that *Whitney and Garvine* [2005] derived, over which winds must blow to alter significantly a buoyant plume's density structure. Lastly, two days is roughly the decorrelation time scale of the winds estimated at Cape Farewell with QuikSCAT data for the year 2004. Note that this averaging reduces the magnitude of the wind stresses in Fig. 2.12 and 2.13, while in fact the maximum wind stresses during strong wind events in summer can exceed 0.2 N m^{-2} (corresponding to wind speeds in excess of 20 m s^{-1}).

The regressions in Fig. 2.12 and 2.13 suggest that the EGCC is responding to the along-shelf wind stress qualitatively akin to what has been observed for smaller scale coastal currents in mid-latitudes. For a strong downwelling wind, $\tau_{along} < 0$, the depth of the front increases, the current narrows, and the equatorward volume transport increases. The anomalous h_{obs} observed in 2003 (open circle in Fig. 2.12*a*) was excluded from the depth correlation and, to be consistent, the other correlations do not include the 2003 data either. Choosing an isohaline that captures the EGCC in 2003, such as $S = 34.5$, and then calculating h_{obs}, would have corrected the observed depth to be in line with the rest of the data, but to keep things consistent we wanted to use the same definition across all years. A more complicated method may be useful in the future.

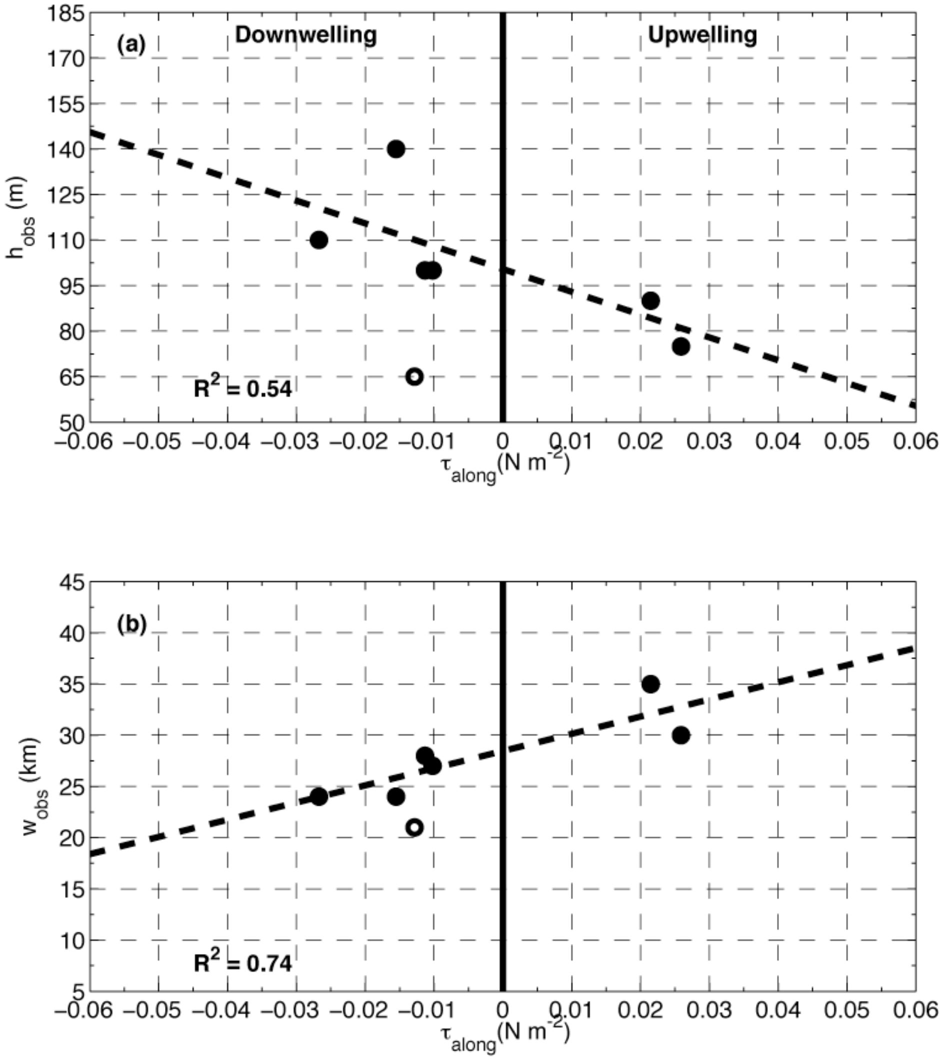

Figure 2.12. *(a)* Depth of the 34-isohaline at the bottom, h_{obs}, which indicates the foot of the EGCC front at Cape Farewell as a function of along-shelf wind stress (upwelling favorable: $\tau_{along} > 0$). The dashed line is a linear fit to the Cape Farewell data. Open circles are data not used in the regression (see text). *(b)* Same as Fig. 2.12*a*, except for the width of the EGCC, w_{obs}, versus τ_{along}.

Note that the freshwater flux (FW_{flux}) has relatively less dependence on the wind stress (Fig. 2.13*b*), implying the importance of the corresponding salinity field to the FW_{flux} calculation. If no low-salinity water is present at the time, the FW_{flux} will not increase substantially even if strong downwelling favorable winds are blowing.

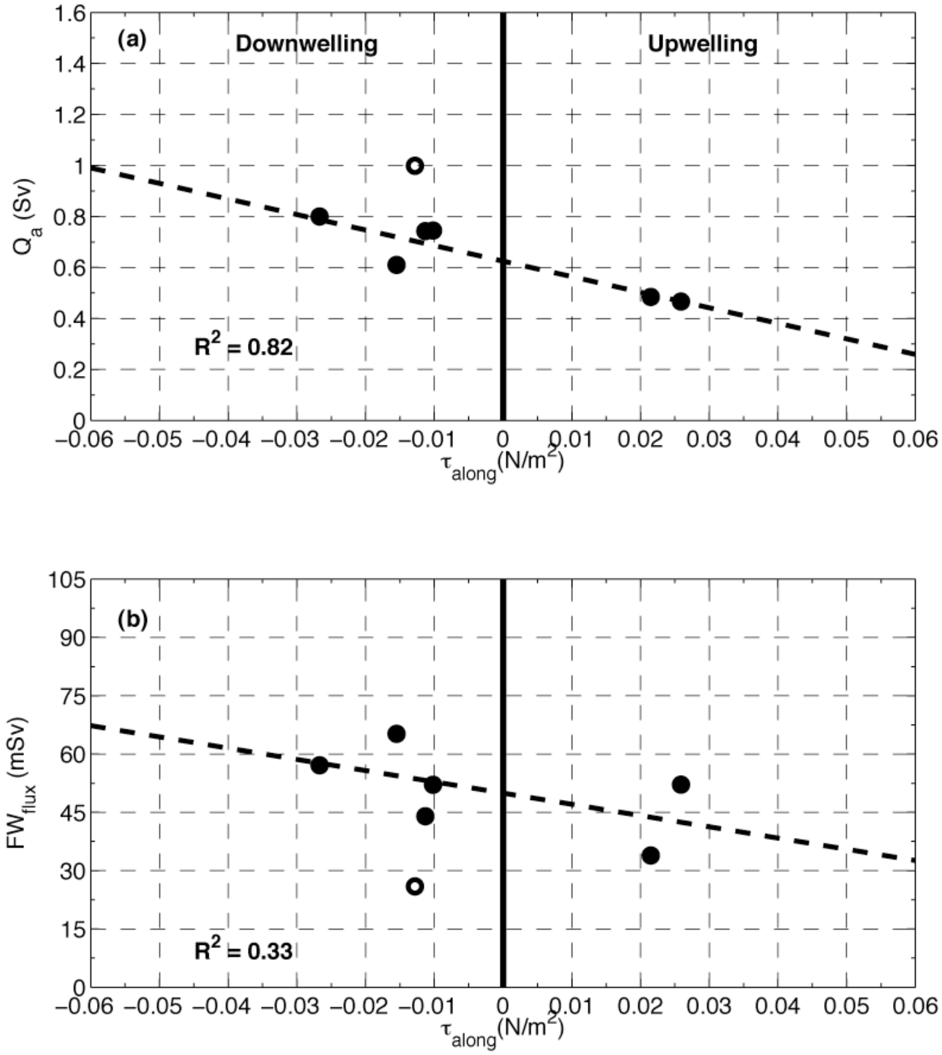

Figure 2.13. *(a)* Same as Fig. 2.12*a*, except for EGCC absolute transport, Q_a, versus τ_{along}. The linear fit is used to adjust the JR105 transports into "no-wind" values as discussed in Section 3.2.3. *(b)* Same as Fig. 2.12*a*, except for EGCC freshwater flux, FW_{flux}, versus τ_{along}.

The total observed ranges in these quantities are a deepening of 70 m, a narrowing of 15 km, and an increase in transport of 0.5 Sv. Clearly the EGCC varies significantly with the wind. Are such wind events strong enough to reverse the coastal current? We can check this by applying the wind strength index ($W_s = u_{wind} / u_{buoy}$) noted above to each crossing of the EGCC to test whether the EGCC is in a more buoyancy-driven or wind-driven state [*Whitney and Garvine*, 2005].

This was done using the observed scales of the EGCC listed in Tables 2.1-2.3. To estimate the wind-driven velocity scale, we follow *Whitney and Garvine* [2005] who use quadratic drag laws to represent the surface and bottom stresses resulting in the simple expression

$$u_{wind} = \sqrt{\frac{\rho_{air}}{\rho}\frac{C_{10}}{C_D}} \cdot U \approx 2.65 \times 10^{-2} \cdot U \tag{2.3}$$

where ρ_{air} is the air density, ρ is the water density, C_{10} is the surface drag coefficient, C_D is the bottom drag coefficient, and U is the wind velocity. The buoyant velocity scale can be estimated by considering a two-layer thermal wind balance where the lower layer is at rest and the upper layer is of thickness h_{obs}. This gives the scale

$$u_{buoy} = \left(\frac{\sqrt{g' h_{obs}}}{f \cdot W_{obs}}\right)\left(2g' Q_a f\right)^{1/4} \tag{2.4}$$

where the first factor is the Rossby radius of deformation, $R = (g' h_{obs})^{1/2}/f$, divided by the current width, W_{obs}, and the second factor includes the reduced gravity, g', the transport, Q_a, and the Coriolis parameter, f, and represents a gravity current speed, $(g' h_p)^{1/2}$.

Taking U in (2.3) to be the same wind velocity used to calculate the wind stresses, the corresponding values of W_s for the EGCC at Cape Farewell are listed in Table 2.2 (Table 2.3 lists W_s for the 2004 sections farther north). Note that $|W_s| < 1$ for all years and sections. This implies that the EGCC is always in a buoyancy-driven state, at least for the times that observations exist. This compares favorably to the results of *Whitney and Garvine* [2005] who showed that for a larger scale coastal current such as the Alaska Coastal Current, strong wind events did not result in wind-driven flow reversals that occur for smaller scale currents such as the Delaware River Coastal Current. The largest

$|W_s|$ occurred in 2003 due to the decreased stratification and relatively high wind speeds; the largest positive W_s occurred during JR105 at section 5 where the strongest upwelling winds were recorded and the EGCC is the least well-defined.

The Cape Farewell section taken in 2004 is notable as having the largest positive W_s at that location, suggesting that it was during this occupation that upwelling winds had the strongest effect on the EGCC structure and flow. Given the same stratification, transport, and structure of the EGCC as observed in 2004 at section 1, U would need to be ~27 m s^{-1} in order to get $W_s = 1$. These are strong winds, but not unreasonable during a storm event. In contrast, given a smaller stratification, such as for OC395 in 2003 where g' was less than one third its 2004 value, less intense winds, on the order of ~18 m s^{-1}, could potentially reverse the EGCC flow according to this simple scaling. Wintertime might be the season for such flow reversals, since the winds are stronger and without any sea ice melt the stratification is lower, but the presence of sea ice might lessen the transfer of wind stress to the ocean.

The wind strength index magnitude, $|W_s|$, for each northern section is < 1, indicating that the buoyancy driven part of the EGCC dominates at these locations as well, even during the strong winds observed during the occupation of section 2. These values are listed in Table 2.3.

2.4.3 Internal variability

Characterized by high velocities that are sheared in the vertical and horizontal over small spatial scales, the EGCC may be susceptible to local instabilities. These instabilities are another possible forcing mechanism that would introduce variability into the temporal and alongshelf structure of the EGCC. Variability of this kind is common in shelfbreak currents, as observed for example by *Fratantoni et al.* [2002]. A complete instability analysis is beyond the scope of this thesis, but in this section we discuss briefly the basic vorticity structure of the flow at each location.

To start, we calculate the ratio of the relative vorticity, in this case $-U_y$ where U is the alongstream velocity and y is the cross-shelf coordinate (subscript denotes partial differentiation), to the planetary vorticity that is defined as the local Coriolis parameter, f. This ratio provides a measure of the nonlinearity of the flow, since it is equivalent to the Rossby number, U / fL, given an appropriate length scale L. The flow at section 2, near 63ºN (see Fig. 2.4), had the highest values of $-U_y / f$ (averaged over the top 200 m of the water column), ranging from -0.6 on the inshore side of the EGCC to 0.6 on the offshore side of the current. The averaging is done to reduce the noise associated with the vorticity calculation. The switch from anticyclonic ($-U_y < 0$) to cyclonic flow ($-U_y > 0$) is expected for a jet feature like the EGCC. Sections 2-4 all exhibited a similar $-U_y / f$ range, -0.4-0.4, except for the shelfbreak area of section 4 (see Fig. 2.6) which had relative vorticities on par with f. In contrast, the northern transect near 68ºN had the lowest relative vorticities, with the ratio $-U_y / f \sim$ -0.2-0.2.

Associated with the highly nonlinear flow at section 2 was evidence for enhanced turbulent mixing due to shear instability, indicated from calculation of the bulk Richardson number, $Ri = N^2 / U_z^2$, where N^2 is the stratification of the water and U_z the vertical shear of the horizontal alongstream velocity. Values of $Ri < 0.25$ indicate regions where mixing is likely, and these are found within the EGCC at section 2, as well as at the boundary between the EGCC and EGC (near station 37 in Fig. 2.4). Enhanced mixing was also observed in the core of the EGCC jet in section 4, with $Ri < 0.25$ found centered near station 98 in Fig. 2.6. Turbulent mixing was also apparent in 2003 at the Cape Farewell section shown in Fig. 2.11, except in this case, it was contained within the bottom boundary layer.

Lozier et al. [2002] found that the growth rate of an unstable front increased with increasing Rossby number, suggesting that the observed EGCC at sections 1-4 might be more susceptible to instabilities. But is the EGCC unstable, given that it is observed to be highly nonlinear in some sections, with enhanced turbulent mixing? Insight into this question can be obtained by calculating the total potential vorticity, Q, of the flow at each location. In this case we are defining Q as the Ertel potential vorticity, which includes not only the relative vorticity term, but also a stretching term (related to the planetary vorticity f) and a tilting vorticity term. These are discussed in more detail in *Pickart et al.*

[2005], though see *Pedlosky* [1987] for a more classical treatment. Once we have calculated Q, we can examine its cross-shelf gradient to see if it changes sign, which is a necessary condition for baroclinic instability to occur [*Pedlosky*, 1987].

From the hydrographic and velocity fields discussed above, we constructed fields of Q, then averaged over the upper 200 m layer, which we designate as Q_{200}. Then we take the derivative of Q_{200} with y. The results are intriguing, showing that $\partial Q_{200}/\partial y$ changes sign only in sections 2 and 3 of JR105, mainly due to the large anticyclonic relative vorticities observed there (otherwise the stretching vorticity term dominates and is positive). At Cape Farewell, only the 2001 section was found to satisfy this criteria, since the EGCC jet in that year was found centered over the shelf more, instead of adjacent to the coast (see Fig. 2.13). Overall, then, the EGCC is found to be susceptible to baroclinic instability, with observations confirming the highly nonlinear state of the flow along with enhanced mixing. These processes likely add to the variability observed in the EGCC, and deserve further consideration for a complete understanding of the EGCC's dynamics and its relation with the EGC.

2.5 Discussion and summary

Although we have shown that the EGCC is present along the entire southeast Greenland coast in summer and that the current responds to strong along-shelf wind forcing, a compelling open question remains: What explains the large length scales and transport of the EGCC on the inner shelf if it is not purely meltwater driven? In other words, what is the origin of the EGCC and what sustains it down the coast as it subject to intense mixing and strong winds? We believe the answer in part lies in the complex shelf bathymetry and its influence on the EGC, as well as the continual melting of sea ice and persistent downwelling favorable winds off southeast Greenland.

Our hypothesis is that the EGC, starting from Fram Strait, flows equatorward generally centered on the shelfbreak, but varies in position due to bathymetric irregularities. South of Denmark Strait, the Kangerdlugssuaq Trough (KG, see Fig. 2.1) is a large canyon feature (approximately 50 km wide and > 200 m deeper than the adjoining shelf) that divides the shelf crossways and strongly influences the path of the EGC. We surmise that part of the time the EGC continues predominantly on its shelfbreak path, while at other times much of it diverts inshore following the isobaths of the KG towards the Greenland continent. Two possibilities then exist for the ultimate formation of the EGCC, without which the original flow would just return along the opposite side of the KG back to the shelfbreak. The first is the diverging isobaths on the western side of the head of the KG trough (Fig. 2.1) that may lead to a splitting of the flow as it crosses the trough and begins to follow the bathymetry. This would lead to an inner branch near the coast and a return branch that flows back to the shelfbreak. The second mechanism involves mixing within the canyon, induced either by local eddy formation or intense frontal mixing. This mixing would alter the stratification, and thus affect the trapping depth of the buoyant flow, possibly allowing it to cross isobaths and emerge as an inner branch. The process of a boundary current encountering a canyon such as the KG trough is modeled in the laboratory and the results are discussed in Chapter 5.

In any event, observations show an inner branch downstream of the KG, which is now called the EGCC; it undergoes additional modification as it receives meltwater runoff and sea ice melt. The two branches (EGC and EGCC) come in close proximity again near JR105 section 2 (63°N) where the shelf narrows to less than 40 km. South of this latitude, bathymetry again likely influences the circulation, where the branches separate again. This is most likely due to a basin feature on the shelf located just downstream of section 2, which is supported by drifter studies showing a similar offshore movement at that location [*Reverdin et al.,* 2003; *Jakobsen et al.,* 2003].

An updated circulation schematic based upon the results of this chapter, and supported by the remaining chapters of the thesis, is shown in Fig. 2.14. The schematic illustrates the main areas where bathymetric features strongly influence the interaction of the EGCC and EGC. The KG trough is identified in Fig. 2.14 as the first major diversion of the EGC onto the shelf, an idea explored further in Chapter 5, while the previously known influence of the Sermilik Trough near section 3 is depicted as well.

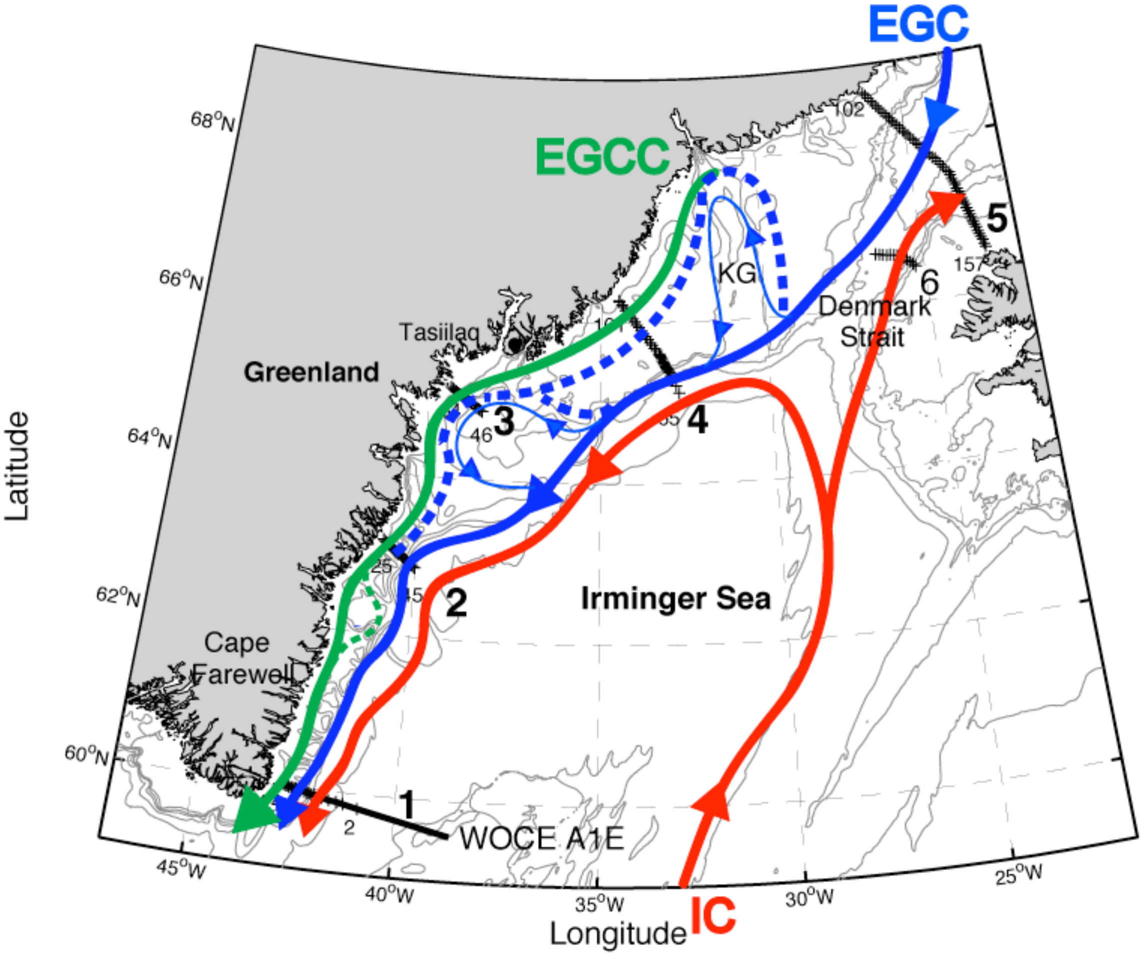

Figure 2.14. Surface circulation schematic for the summertime boundary current system of the Irminger Sea. Solid lines show observed paths of the EGC, EGCC, and the IC, while dashed lines indicate possible flow paths induced by the effects of bathymetry, wind, or internal variability. North of the KG trough the EGCC's presence is uncertain, though it is likely weaker than what is observed farther south.

The line of reasoning that leads to the bifurcation hypothesis for the formation of the EGCC is as follows. First, only a weak EGCC was observed on the shelf north of Denmark Strait (see JR105 section 5, Fig. 2.7) and a coastal current flow has never been previously reported farther north on the Greenland shelf, albeit that region is even more difficult to observe. Second, the θ/S properties of the EGCC closely follow those of the EGC observed at Denmark Strait, suggesting a shared Arctic source (Fig. 2.2 and more detail in Fig. 2.15). Slight differences arise in their hydrography as one moves south from

Denmark Strait as the EGC begins to mix with the AW influenced Irminger Current, while the EGCC likely receives more freshwater influence from the Greenland continent and from melting sea ice. Fig. 2.15 shows a breakdown of the θ/S properties by section and current (EGC vs. EGCC, as defined above) and clearly shows the link between the EGC at section 5 in the north, with the EGCC farther south, and the complete disappearance of polar water at Cape Farewell (section 1).

The next piece of evidence comes from inspection of the thermosalinograph data taken during the cruise. A key advantage of the thermosalinograph data (Fig. 2.8) is its coverage of the shelf where no CTD data exist, which helps in describing the bathymetric constraints on the EGC and EGCC.

The surface salinities shown in Fig. 2.8*a* confirm the presence of fresh water ($S <$ 32.5) on the innermost shelf at all latitudes sampled. Though this fresh water does not necessarily indicate the presence of the EGCC as shown earlier, it does reveal where the EGCC is not located. Downstream of JR105 section 4, note that the freshest waters are confined to the inshore side of the deep basin found at JR105 section 3. This is consistent with the idea that the trough near section 3 (Fig. 2.14) is another location, in addition to the initial interaction with the KG trough upstream, where the EGC might be diverted inshore. Warmer and saltier water that indicates modification by AW is also found on the upstream side of the basin near JR105 section 3 (Fig. 2.8), suggesting that the diversion of the EGC from the shelfbreak inshore brought with it some IC water. During summer 2004 then, it seems that the majority of the flow navigated the inshore side of this basin, consistent with the circulation picture suggested by drifter studies [*Reverdin, et al. 2003*; *Jakobsen, et al.* 2003].

How did the flow get inshore in the first place? Canyons and bathymetric bends have been shown to significantly affect buoyant coastal currents, though the exact behavior depends on the degree of the bathymetric anomaly, the strength of any ambient flow, and the stratification of the flow [*Williams et al.*, 2001; *Chapman*, 2003; *Wolfe and Cenedese*, 2006]. One such bathymetry-induced effect is the separation of a buoyant current if it is unable to navigate across a gap. This may happen to some degree to the

EGC as it approaches the KG trough. Upstream of JR105 section 4, the water in the vicinity of the trough is anomalously warm (*T* ~ 6-7°C, see Fig. 2.8*b*) and salty (*S* > 32.5) compared to the surrounding shelf water (*T* ~ 4-5°C, *S* < 32.5). This suggests that the EGC turns inshore here, carrying with it warmer and saltier water from the shelfbreak where Atlantic-influenced water resides. This is consistent with an XCTD section (not shown) taken in 2002 during OC380, which shows AW present on both sides of the trough, while the center of the trough contains colder and fresher water. Sea ice concentrations observed remotely from the SMMR and SSM/I instruments are consistent with this circulation scheme as well [*Cavalieri et al.,* 2005]. On the other hand, the tracer measurements of *Pickart et al.* [2005] suggest that the EGC can also take a more direct route along the shelfbreak at the seaward edge of the KG trough. This implies that there is a time-dependent bifurcation of the flow associated with the anomalous bathymetry of the KG. One other possibility is that part of the EGC continues equatorward along the shelfbreak, while a shallower part diverts along the edge of the KG canyon to become the EGCC.

Either way, the process is apparently time-dependent and complex. This subject of bathymetric-induced variability is taken up again in detail in Chapter 5 of this thesis, where laboratory experiments are conducted to explore the interaction of a buoyancy-driven current, such as the EGC, with a canyon, to see if the EGCC could be formed by such a process.

In summary, this chapter has presented the first comprehensive description of the East Greenland Coastal Current (EGCC) on the southeast Greenland shelf, primarily using measurements from a hydrographic/velocity survey conducted in summer 2004. We have determined that the EGCC exists along the entire 1000 km long shelf, distinct from the shelfbreak flow of the East Greenland Current (EGC), with a high velocity core (ranging from 50-100 cm s^{-1}) and a characteristic low-salinity, wedge-shaped structure. The single exception to this was near 63°N, where the shelf narrows considerably and the EGC comes into close proximity with the inner shelf EGCC. The flow is highly nonlinear at this location and shows evidence of enhanced mixing at its offshore edge, as well as the potential to develop baroclinic instabilities. The merging of the two currents, when added to the evidence of the EGC bifurcation farther upstream inferred from *θ/S* measurements, satellite sea ice data, and previous drifter studies, suggests that the EGCC is in fact an inner branch of the EGC.

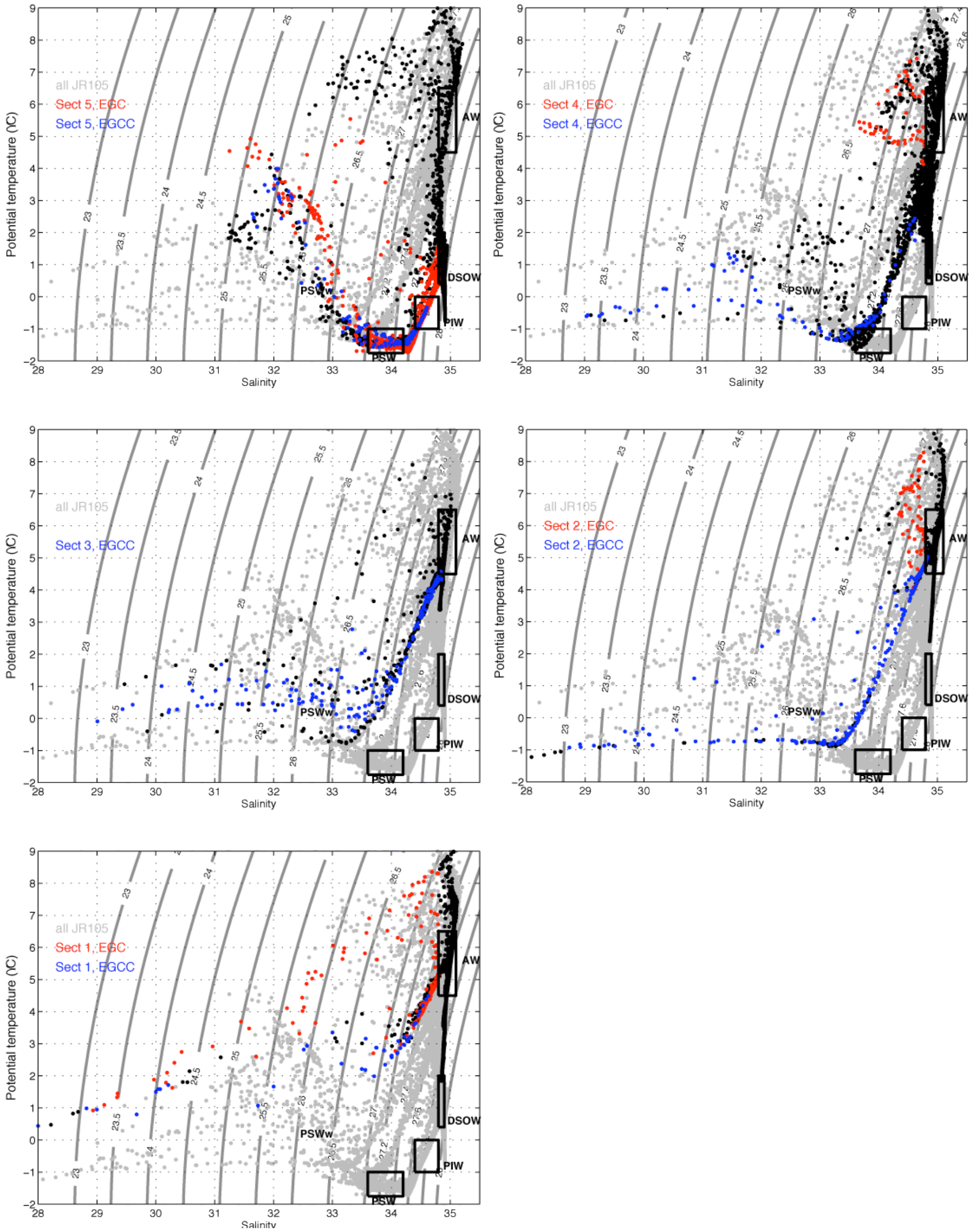

Figure 2.15. *θ/S* properties of each JR105 section broken into the current components as defined in the text. Water masses are labeled identically to Fig. 2.2.

Chapter 3

The volume and freshwater transports of the East Greenland Coastal Current

3.1 Introduction

The aim of this chapter is to calculate the volume and freshwater transports of the EGCC and EGC, making use of the new understanding of the EGCC's hydrographic and velocity structure, as well as its short-term temporal variability that was discussed in Chapter 2. Volume and freshwater transports can aid in improving our understanding of how the circulation in a region might change. This is particularly useful in the subpolar North Atlantic, where numerous changes have been observed in the past decade that would not have been detected without the help of volume budgets.

These changes include the freshening of the northern North Atlantic from the mid-1960's to the late 1990's [*Curry and Mauritzen*, 2005], a rapid increase in ice melt and calving of glaciers from Greenland [e.g. *Krabill et al.,* 1999; *Krabill et al.,* 2004; *Rignot et al.,* 2004], and a new appreciation of the linkages between the freshwater cycles of the Nordic Seas with the circulation patterns of the North Atlantic inflow to the subpolar region [*Hakkinen and Rhines*, 2004; *Hatun et al.,* 2005]. Two recent reviews of the freshwater budgets of the Arctic Ocean have brought new clarity to these issues: *Serreze et al.* [2006] calculated the large-scale freshwater budget of the Arctic including the terrestrial and atmospheric components as an extension of the classic *Aagaard and Carmack* [1989] study, while *Dickson et al.* [2007] focused instead on the freshwater flux terms located at the numerous straits and pathways around the subpolar-polar region.

This chapter aims to improve one component of those works, namely, the liquid freshwater transport along the southeast Greenland coast. A more regional scale view of the freshwater and volume budgets that includes the EGCC as well as the west Greenland shelf and the northeast Greenland shelf is given in *Bacon et al.* [2008]. Note that the estimates presented below represent summertime conditions when salinities are relatively lower at the surface compared to wintertime (biasing the freshwater flux values high), but the velocities are assumed to be less than in winter when the wind forcing is stronger (biasing the volume and freshwater fluxes low). Without a baseline understanding of the transports for the EGCC and EGC system, it would be impossible to recognize the significance of any future change.

3.2 Transports

3.2.1 Volume fluxes

In this chapter, we utilize the definitions of the EGCC and EGC discussed in Chapter 2 (and illustrated in Fig. 2.3 - 2.7) to compute absolute alongstream transports, Q_a (in units of Sverdrups, 1 Sv = 10^6 m^3 s^{-1}), for each current. Previous estimates of EGCC volume transport range from 0.8 Sv at Cape Farewell, measured by B02 in 1997 using geostrophic velocities referenced to the bottom, to 1.6 Sv reported near JR105 section 4 based on CTD data referenced using current meters, although the latter estimate most likely was a combination of the EGCC and EGC sampled at coarse resolution [*Malmberg et al.,* 1967]. Additional historical estimates of the relative geostrophic transport based on the 33.5-isohaline were found to be between 0.2 and 2 Sv at a range of locations on the

East Greenland shelf [*Wilkinson and Bacon*, 2005]. All of these previous estimates of EGCC transport, however, are based on unreferenced geostrophic velocities, which can misrepresent the true transport, or are based on sparsely spaced data that may not have completely sampled the current.

Previous EGC transport estimates exhibit a large range, depending on location, year, and season of the measurement, as well as how the investigator defined the current. A transport budget of the Nordic Seas indicated that the EGC through Denmark Strait carries 1.3 Sv [*Hansen and Osterhus*, 2000]. This number was used in recent work done on the Irminger Sea transport budget, based on data from a 2001 field program, to find a 0.7 Sv transport for the EGC south of Denmark Strait where the EGC and IC first merge [*Pickart et al.,* 2005]. Other transports reported for the EGC are larger and range up to 3.0 Sv [see the table in *Pickart et al.,* 2005], while some studies define the EGC to include the Atlantic-origin Irminger Current, bringing the volume transport estimates to ~13-15 Sv [*Pickart et al.,* 2005; *Holliday et al.,* 2007].

Transports calculated for each JR105 transect are shown in Fig. 3.1*a*. We include individual transport values for the EGCC and EGC, as well as the combined EGC/EGCC system. These are listed in Table 3.1 along with geostrophic transports referenced to the bottom, Q_{geo}, and the error estimates, which are discussed in Appendix A. The adjusted transport values for the EGCC and EGC/EGCC system displayed in Fig. 3.1*a* (bold, solid lines) will be explained in the next section when the effect of the wind is introduced as a factor in EGCC transport variability. We note that the ratio Q_a / Q_{geo} for the EGCC is generally > 1 (as large as 2 for sections 1 and 2). The exception to this is at section 4 near 66°N where $Q_a / Q_{geo} \approx 0.5$, indicating the presence of a poleward barotropic flow at this location.

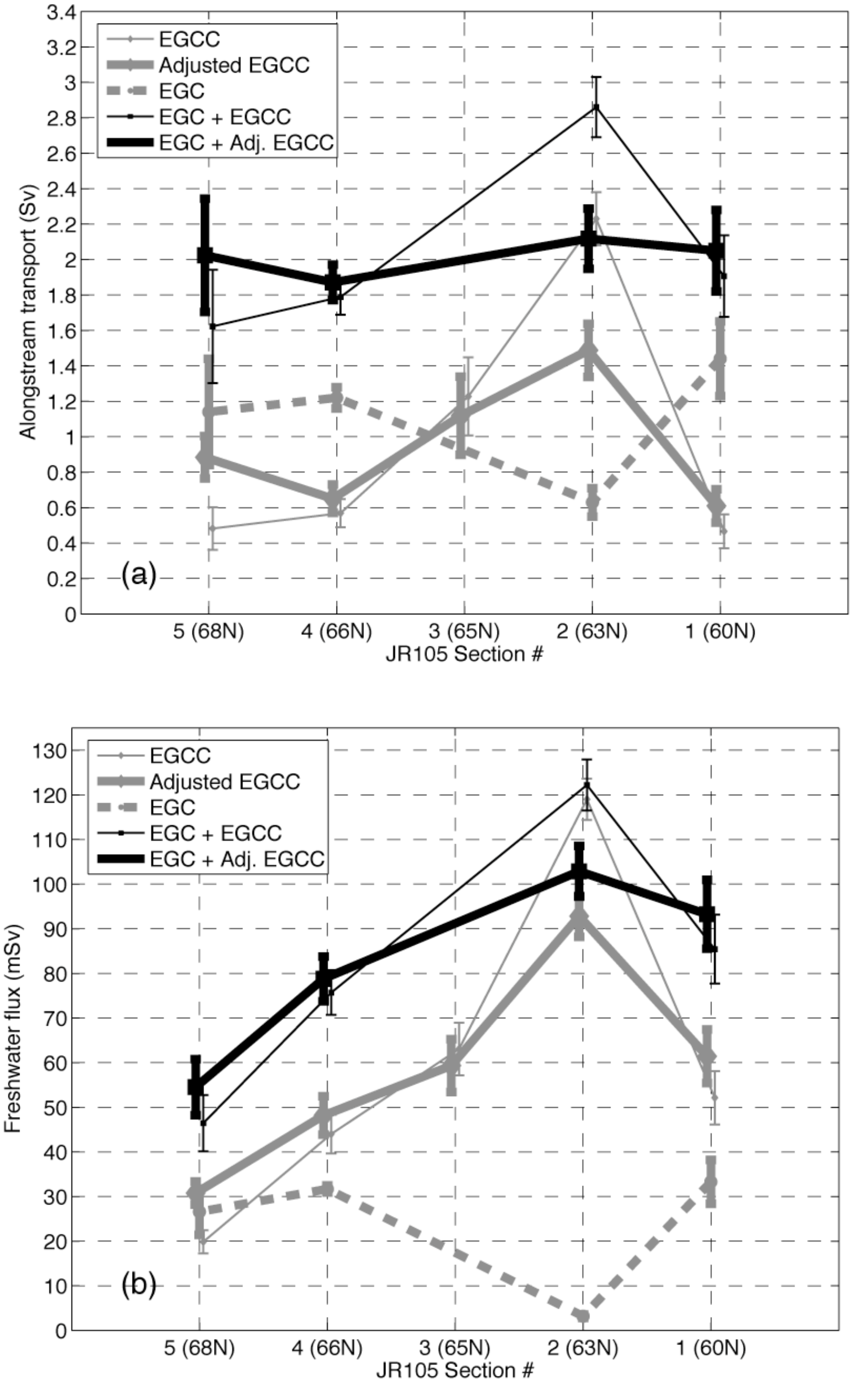

Figure 3.1. *(a)* Alongstream transport, Q_a (Sv), at each section for the currents on the East Greenland shelf: EGC, EGCC, and total EGC/EGCC system. Definitions of each current at each JR105 transect are given in the text. Thin lines show the original, unadjusted values. Thick lines show the wind-adjusted values for the same features; note that no adjustment was done for the EGC data. *(b)* Same as in *a* except freshwater fluxes, FW_{flux} (mSv), for each JR105 section are shown using $S_{ref} = 34.8$.

Table 3.1. EGCC absolute transports, Q_a, geostrophic transports, Q_{geo}, freshwater fluxes referenced to S_{ref} ~ 34.8, and their uncertainties as defined in the text.

Section	Q_a (Sv)	Q_{geo} (Sv)	*Q error* (Sv)	FW_{flux} (mSv)	*FW error* (mSv)
1	0.47	0.2	±0.1 (±0.09[a])	52	± 6.0 (±9[a])
2	2.23	1.1	±0.15	119	±5.7
3	1.23	1.0	±0.22	63	±7.7
4	0.57	1.2	±0.08	44	±4.9
5	0.48	0.1	±0.12	20	±3.6
1 (2001)	0.74	0.4	±0.1	44	±4.2
1 (2002)	0.61	0.9	±0.1	88	±3.1
1 (2003)	0.99	0.2	±0.1	26	±2.0
1 (1997[b])	--	0.84	--	57[c]	--

[a] Standard errors for Cape Farewell sections only in parentheses. All errors are discussed in Appendix A.

[a] The 1997 estimates are from Bacon, et al. (2002).

Progressing equatorward, the EGCC transport (solid, thin gray line in Fig. 3.1*a*) increases roughly four-fold from section 5 north of Denmark Strait, where Q_a = 0.48 ± 0.12 Sv to section 2 near 63°N, where Q_a = 2.2 ± 0.22 Sv. An especially large increase occurs at section 2, followed by an abrupt decrease at Cape Farewell. The transport of the EGC (dashed gray line in Fig. 3.1*a*) through Denmark Strait is 1.1 ± 0.3 Sv, which is well within the published values, especially considering the strong recirculation observed there (see Fig. 2.7). South of Denmark Strait at JR105 section 4, the EGC transport remains similar, though this number must be considered somewhat suspect because of the strong eddy activity present near the shelfbreak at the time of occupation of the section. The anomalous feature in the EGC transport trend is the decrease in volume flux at section 2 near 63°N. Interestingly, this is where the EGCC transport increases substantially, and when the two currents are considered as a single system (solid, thin black line in Fig. 3.1*a*), the anomalous nature of section 2 is reduced (but not completely removed). Other than this increase in total transport at section 2, the combined volume flux of the EGC/EGCC system stays approximately constant, 1.6 - 1.9 (±0.1 - 0.3) Sv, from north to south. Is there a convergence at section 2 or does this just reflect the need for long-term measurements since synoptic sections will inevitably exhibit variability? A clue to answering this question was given in the previous chapter, where it was shown that the along-shelf wind stress played an important role in modulating the EGCC transport. This is sorted out carefully in Section 3.2.3 below.

3.2.2 Freshwater fluxes

Freshwater fluxes, as described below, are actually freshwater flux anomalies and are equivalent to the flux of zero salinity water that must be combined with a flux of water at a reference salinity to equal the observed flux at the observed salinity [*Melling*, 2000]. The freshwater flux anomaly, FW_{flux}, is calculated as

$$FW_{flux} = \iint_{dzdx} U_{abs}(x,z) \cdot \frac{\left(S_{ref} - S(x,z)\right)}{S(x,z)} dxdz \qquad (3.1)$$

where U_{abs} is alongstream absolute velocity, S is the salinity, and $S_{ref} = 34.8$ is the reference salinity chosen to compare with previous estimates of FW_{flux} [e.g. *Aagaard and Carmack*, 1989; *Woodgate and Aagaard*, 2005; *Serreze et al.,* 2007]. Actual freshwater fluxes are equal to the total mass flux minus the mass flux of salt, but are more difficult to estimate due to data inadequacies. Here we estimate the integral in (3.1) using our gridded sections of salinity and velocity, and refer to the resulting freshwater flux anomalies as simply freshwater fluxes.

Since the EGCC is characterized by very low salinities, it could contribute significantly to the region's freshwater budget. *B02* gave a synoptic estimate of the EGCC freshwater flux of 1800 km^3 yr^{-1}, referenced to a mean salinity of 34.956, with an estimated annual mean value of 570 km^3 yr^{-1}. A useful conversion is that 31.54 km^3 yr^{-1} ≈ 1 mSv (10^3 m^3 s^{-1}), so that *B02*'s synoptic FW_{flux} value of 1800 km^3 yr^{-1} is approximately 57 mSv. Their FW_{flux} value increases to about 66 mSv when $S_{ref} = 34.8$ is used. All calculations in this paper are done using $S_{ref} = 34.8$.

Including this synoptic FW_{flux} estimate in the updated freshwater budget of *Serreze et al.* [2006] shows the potential importance of the EGCC for the Nordic Seas.

They calculated a net liquid freshwater export of ~76 mSv to the Nordic Seas from Fram Strait, while *Dickson et al.* [2007] estimated the net liquid export leaving the Nordic Seas from Denmark Strait as ~86 mSv. *B02's* synoptic estimate of EGCC freshwater flux is thus comparable in magnitude to the Denmark Strait outflow, and is much greater than the freshwater fluxes calculated for either the Norwegian Coastal Current, ~8 mSv [*Aagaard and Carmack*, 1989], or the Alaska Coastal Current, ~13 mSv [*Woodgate and Aagaard,* 2005].

In 2004, we found the EGCC FW_{flux} to be 52 ± 6.0 mSv at Cape Farewell, similar in magnitude to the 1997 estimate of *B02*. Along the southeast Greenland coast, however, the EGCC FW_{flux} estimates vary significantly (Fig. 3.1*b*, solid, thin gray line). This is in large part due to the variation in observed EGCC transports: the largest FW_{flux} of 119 ± 5.7 mSv corresponds to the largest Q_a that was calculated at 63°N at section 2. However, the salinity field matters as well. For example, the transport at section 3 is almost twice that observed at Cape Farewell, but its freshwater flux of 63 ± 7.7 mSv is not significantly different due to the very low minimum salinities ($S < 28$) observed in the EGCC at Cape Farewell. Overall the FW_{flux} of the EGCC increases equatorward by 32 ± 6.5 mSv.

By comparison, Fig. 3.1*b* (dashed gray line) shows that the FW_{flux} of the EGC is relatively constant, 26 – 33 mSv, with the exception of section 2, where the current carries almost no freshwater (FW_{flux} = 3 ± 0.4 mSv). As was true for the volume flux, this is the location where the EGCC FW_{flux} increases substantially, and considering the EGCC/EGC system together reduces the anomaly (Fig. 3.1*b*, solid, thin black line). The FW_{flux} of the EGC/EGCC system increases equatorward similar to the EGCC trend, since the EGCC FW_{flux} estimates are all greater than or equal to the EGC FW_{flux}. The net freshwater flux gain is about 39 ± 9.9 mSv, although there is still a significant anomaly at section 2. Can the alongstream trend and net gain of freshwater in our data set be explained by available freshwater sources or by other variable forcing factors such as the wind? We examine this question further below.

3.2.3 Adjusted alongstream transport trends for the EGC/EGCC

The EGCC, although present all along the southeast coast of Greenland during JR105, was seen to vary significantly in its hydrographic and velocity structure at each location in Chapter 2. Using the results from section 2.4.2, we now demonstrate that much of this alongstream variability was due to the time-varying winds during our survey. Furthermore, by adjusting the volume and freshwater transports for these wind variations, the resulting alongstream trends are more meaningfully interpreted.

Considering the Cape Farewell section transports, we can find a "no-wind" value for the EGCC there, i.e. at $\tau_{along} = 0$, $Q_a = 0.66$ Sv in Fig. 2.13*a*. Then we can calculate a percentage increase (decrease) for the transport as the wind stress becomes increasingly downwelling favorable, $\tau_{along} < 0$ (upwelling favorable, $\tau_{along} > 0$). If we assume the same relationship holds for all latitudes during JR105, we can adjust the volume transports at each section for the wind stress observed there. For example, at section 2 the observed transport was 2.2 Sv with a two-day average wind stress of -0.028 N m^{-2}. Since the winds were downwelling favorable, the adjusted transport will be smaller and in this case equals 1.54 Sv, a 33% decrease.

This approach is an empirical one that differs from previous studies that have attempted to estimate the wind's effect on the buoyant current transport. In those studies, the transport is assumed to be linear and is decomposed into wind-driven and buoyancy-driven components that can be estimated separately [*Whitney and Garvine*, 2005; *Lentz and Largier*, 2006]. The critical assumption then is that the winds force a barotropic response that does not affect the density driven flow significantly. This assumption has drawbacks, most notably that any barotropic response will result in a set-up or set-down that will drive a geostrophic response. Our approach uses observations and hence accounts for these feedbacks. Admittedly, however, the range of observed winds in our study is somewhat limited, with only two upwelling events.

Adjusting the EGCC transports for the observed winds during JR105 results in the alongstream transport trend shown in Fig. 3.1*a* (solid, thick gray line). The most dramatic change occurs at section 2 where the anomalous increase in transport is reduced, although not removed. However, when the adjusted EGCC transport values are combined with the transports of the EGC (solid, thick black line in Fig. 3.1*a*), we find that the jump seen previously at section 2 is completely removed. In the adjusted case, the combined EGCC/EGC system has an approximately constant volume transport of 2 Sv along the entire southeast coast of Greenland. This means that, as a combined current system, the volume transport trend is consistent with there being no sources or sinks of mass.

During summer the predominant winds over the portion of the shelf between sections 2 and 4 are downwelling favorable; these are the "barrier winds" caused by the blocking of air masses by the Greenland continent [*Moore and Renfrew*, 2005]. At Cape Farewell, the wind direction shifts much more frequently with the passage of low-pressure systems throughout the year, and in general wind speeds are much higher during winter than summer. Thus, the wintertime inner shelf circulation near Cape Farewell may be most susceptible to wind reversals, as the winds are potentially strong and upwelling favorable then. North of Cape Farewell the winds stay persistently downwelling favorable throughout the winter, but increase in magnitude, so that in general the EGCC should be narrower and more well mixed during that time period. Furthermore, the input of freshwater may be less, so that the overall structure of the current, and its volume transport and freshwater flux, may be altered from the summertime results presented here. Clearly, wintertime measurements of this system are needed to test these ideas.

We can adjust the EGCC freshwater transport trend, shown in Fig. 3.1*b*, in similar fashion to the volume transport adjustment. The resulting adjusted freshwater fluxes for the EGCC and the combined EGCC/EGC system are shown in Fig. 3.1*b* (solid, thick gray and black lines, respectively). The change in the freshwater transport trend is significant. Instead of showing a large increase from section 5 to section 2, followed by a large drop from section 2 to section 1 at Cape Farewell, the adjusted EGCC FW_{flux} trend increases more slowly to section 2 and does not drop off by as much at Cape Farewell. A more dramatic change occurs in the combined EGCC/EGC system where now the FW_{flux} trend increases equatorward from 55 ± 3.6 mSv at section 5 to 103 ± 5.7 mSv at section 2, then stays roughly constant to Cape Farewell. This estimate at section 2 and section 1 is similar to the estimate for the combined EGCC and EGC system computed by *Dickson et al.* [2007] for the southeast Greenland shelf (see their Fig. 1).

The overall increase in the adjusted FW_{flux} along the path of the EGCC/EGC is ~38 mSv, very close to the net gain seen in the original values, but the changes from section to section differ substantially. Overall, the adjusted FW_{flux} trend seems to make more intuitive sense for a region accumulating freshwater all along its path from melting sea ice and meltwater runoff from Greenland. Those and other factors in the EGCC/EGC freshwater budget are discussed next.

3.3 A simple freshwater budget for the EGC/EGCC

South of Denmark Strait, the EGC and EGCC are the only surface pathways of low-salinity water and hence play a major role in controlling the freshwater distribution in the western North Atlantic. Beyond Cape Farewell, part of the flow of the West Greenland Current eventually joins the Labrador Current and takes this fresh signal all the way to the Middle Atlantic Bight off the Eastern USA [*Fratantoni and Pickart*, 2007]. The pathway from the Labrador Sea to the Middle Atlantic Bight has been studied more extensively [e.g. *Loder et al.*, 1998], yet the freshwater budget and pathways on the southeast Greenland shelf, which feed into this larger scale system, have not been detailed. We now investigate the freshwater sources on the southeast Greenland shelf, estimate their magnitudes, and examine whether these inputs can explain the increase in FW_{flux} observed during JR105 (Fig. 3.1*b*).

Four freshwater sources could potentially alter the FW_{flux} along the EGC/EGCC pathway. We write this as

$$FW_{flux} = FW_{adv} + FW_{seaice} + FW_{iceberg} + FW_{runoff} + FW_{PE} \tag{3.2}$$

where the total FW_{flux} equals the freshwater advected from upstream, FW_{adv}, plus the four contributions: FW_{seaice} is the meltwater from sea ice, $FW_{iceberg}$ is the meltwater from icebergs calved off Greenland, FW_{runoff} is the runoff from Greenland that is mainly meltwater, and FW_{PE} is the net precipitation minus evaporation (P - E) over the area. We consider each source term separately below, although we emphasize that these are crude estimates, as they all have large natural variability and a considerable range of values in the literature. By not accounting for the temporal or spatial variability of each term in (3.2), we are essentially assuming that the total annual mean value was available to the EGCC/EGC system during JR105 and that the distribution of the freshwater source is linear down the shelf. We believe the added complexity of dealing with these assumptions is not warranted for the rough budget calculations considered below.

Fig. 3.2 displays the net freshwater gain estimated for the Greenland shelf from 68°N to 60°N. The largest contribution comes from the melting of sea ice, which ultimately is advected from the Arctic Ocean through Fram Strait, then Denmark Strait, and experiences melting along its entire path during summer. By the latitude of Cape Farewell, no significant sea ice concentration is usually observed in late summer, so any ice at Denmark Strait must melt during its transit down the shelf in the EGC/IC and EGCC. Sea ice concentrations from the Nimbus-7 SMMR and DMSP SSM/I passive microwave data support this observation [*Cavalieri et al.,* 2005].

Though improvements in ice-observing satellites and the associated algorithms have largely reduced the uncertainty in the Fram Strait ice volume flux estimate, it is now known that it exhibits a large natural variability of up to ± 30 mSv [*Martin and Wadhams*, 1999]. *Vinje et al.* [1998] reported a sea ice volume flux of 90 mSv based on combining numerical model results with satellite-derived ice drift velocities. However, estimates based solely on observations such as ice-drifting buoys and upward looking sonar, in addition to satellite data from the SSM/I and AVHRR, all fall below those model values [*Kwok and Rothrock*, 1999]. Thus we take the volume flux from *Kwok and Rothrock* [1999] of 75 mSv as being representative of the Fram Strait ice flux, close to the 73 mSv used in the review by *Serreze et al.*[2006]. The observed variability in ice volume flux can be correlated to the phase of the North Atlantic Oscillation (NAO), the predominant mode of atmospheric forcing in this region. In a low phase of the NAO, *Martin and Wadhams* [1999] found that the ice flux through Fram Strait was only 49 mSv and in higher NAO index years, the ice flux increased correspondingly.

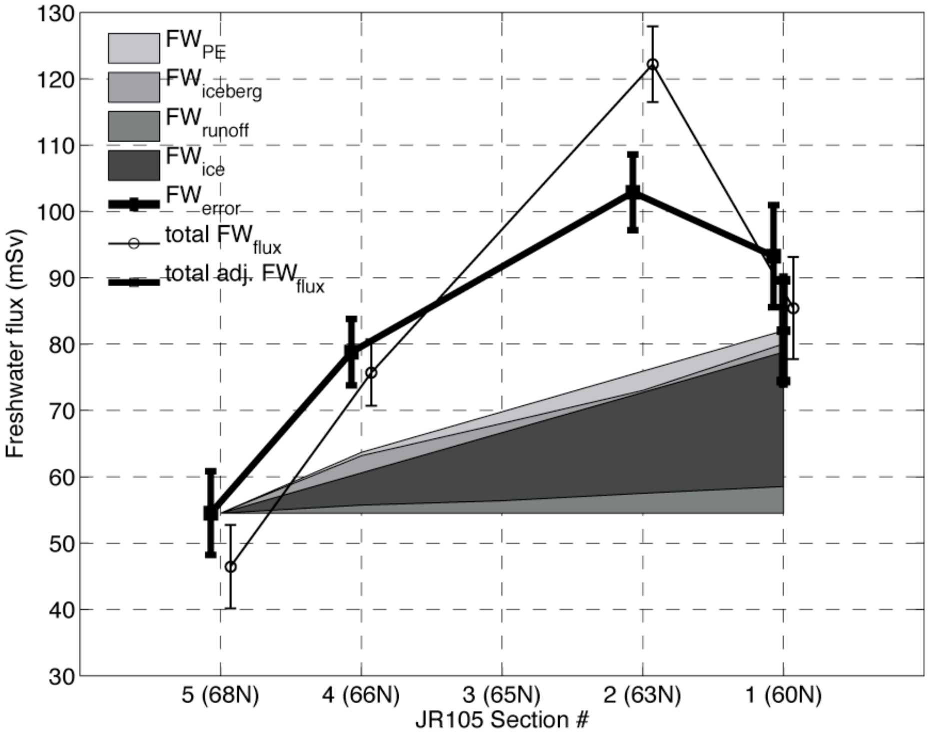

Figure 3.2. The trend in freshwater flux, FW_{flux} (mSv, referenced to $S_{ref} = 34.8$), for the EGC/EGCC system along the East Greenland shelf from 68°N to 60°N, showing the wind-adjusted (bold line) and original (thin line) values. Shading indicates the potential freshwater sources (iceberg calving and melt, sea ice melt, net P – E, and meltwater runoff) available to the EGC/EGCC system along its path, assuming the section 5 FW_{flux} as a starting point.

No previous study has directly estimated the volume of ice passing out of the Nordic Seas through Denmark Strait. As a remnant inflow of Fram Strait ice, the ice flux farther south is usually approximated by looking at the reduction in ice extent. *Aagaard and Carmack* [1989] used a flux of 18 mSv based on ice extent maps, while more recent satellite imagery implies a flux of 19 mSv assuming 75 mSv as a best guess of the Fram Strait flux [*Kwok and Rothrock*, 1999; *Martin and Wadhams*, 1999]. *Dickson et al.* [2007] quote a value of 39 mSv based upon a modeling study, but we stick with observationally based estimates here. From Denmark Strait to Cape Farewell then, 19 ± 7.5 mSv is available to the EGC and EGCC. Whether or not all of this freshwater enters into the currents or stays with them along the entire path is another question; 19 ± 7.5 mSv represents an upper bound.

The remaining three terms in Fig. 3.2 are all the same order of magnitude, and are all significantly less than the sea ice melt term. Runoff from Greenland is mainly meltwater and not riverine; there are high output areas, such as at the mouth of the Kangerdlugssuaq Trough (KG, see Fig. 2.1), that make this contribution similar to point sources like rivers, but for our purposes we take the cumulative input of meltwater along the coastal area and ignore spatial variability. Our estimate of 4 ± 1 mSv is taken from a surface mass balance calculation using a regional climate model of the Greenland continent, and then summed over the JR105 area, 68°N to 60°N [*Box, et al.* 2006; *Box et al.,* 2004]. Evidence of increased melt and enhanced thinning of ice along the Greenland coast, possibly due to global warming effects, is mounting [*Krabill et al.,* 2004; *Krabill et al.,* 1999]. However, the increased freshwater would be an insignificant addition compared with the errors in the rough calculations of the freshwater budget we are considering here.

Solid ice, in the form of icebergs, also originates from the Greenland continent and subsequently melts in the shelf waters. Estimates of iceberg calving rates for this region vary from 1.5 mSv [*Rignot et al.,* 2004] to 2.7 mSv [*Bigg*, 1999]. Several large glacier fields are responsible for the majority of this flux, and evidence is also mounting for an increased calving rate, akin to the increases seen in meltwater production [*Rignot, et al.* 2004]. Since most of this ice will melt by Cape Farewell, we assume the additional freshwater available to the shelf area is the same as the iceberg calving rate and use 2 ± 0.5 mSv as our best estimate in Fig. 3.2. Again, this ignores variation of where and when the icebergs calve and melt, but works well for the budget we are considering here.

The last remaining term is net P - E over the shelf waters (P - E over the Greenland continent is taken into account in the runoff term). Precipitation rates near the Greenland coast have a large range. Next to the coast orographic effects can increase yearly rates to over 2 m yr^{-1}, while over much of the shelf it is more like 0.3 m yr^{-1} [*Box* *et al.,* 2004]. Using those values, and an area of 1.5 x 10^5 km^2 for the 68°N to 60°N shelf (depth < 400m), we estimate a net P - E of 2.5 ± 1 mSv.

Cumulatively, these freshwater sources represent an addition of 27.5 ± 7.6 mSv to the shelf area, and thus to the EGC/EGCC system. This is the right magnitude of increase needed to account for the net gain of 39 ± 9.9 mSv (38 ± 9.9 mSv) in the total EGC/EGCC (wind-adjusted) FW_{flux} values calculated for JR105.

3.4 Discussion and summary

The volume and freshwater transport trends display a more interpretable trend when the EGCC and EGC are considered as a composite system. Accounting for the effect of the along-shelf wind stress on the EGCC flow is fundamental to understanding this system. Winds should influence the EGCC flow more strongly than the EGC since the coastal current is found to be a generally surface-trapped flow over a relatively flatter bottom than the EGC, which is heavily constrained by the shelfbreak. The winds may also play a key role in determining when the EGC moves across the shelf and feeds the EGCC, versus when it remains at the shelfbreak and flows directly equatorward. The persistent downwelling favorable winds observed between JR105 section 4 (66°N) and 2 (63°N) are likely critical to this (see Fig. 1.2), and probably keep the EGCC in a coherent, and observable, form along the southeast Greenland shelf (Fig. 2.14). Correspondingly, any accounting of the volume and freshwater budgets of the Irminger Sea region must include the EGC and EGCC as an integrated system.

We find that when considered together, the EGC/EGCC transports co-vary, carrying a relatively constant 2 Sv of water equatorward along the shelf. This trend emerged only after the effect of along-shelf winds was considered; the significant variability observed in the EGCC hydrographic and velocity structure at each section is related in part to the strength of the along-shelf wind stress, with downwelling favorable winds corresponding to higher transports, and a deeper, narrower EGCC. Interannual measurements (2001-2003) at Cape Farewell showed similar wind-induced variability. A value of 2 Sv is an increase of 0.7 Sv compared to the transport calculated by *Hansen and*

Osterhus [2000], which was needed to balance mass in their Arctic Mediterranean budget schematic. Assuming 2 Sv can be taken as an average for the EGC/EGCC system, some other component of their volume budget must change to compensate. Since the CAA outflow transport was based on the least amount of data and with the highest uncertainties, it is reasonable to assume that the 1.7 Sv assigned to it is too high. A value of 3 Sv for the total surface outflow (CAA plus EGC/EGCC) from the Arctic Mediterranean still seems consistent, then, but with a re-partitioning of transport between the components.

The 2004 survey revealed that the freshwater transport of the EGCC increased from 31 ± 3.6 mSv north of Denmark Strait to 61 ± 6 mSv at Cape Farewell. The net gain in freshwater transport of the combined EGCC/EGC system from Denmark Strait to Cape Farewell, adjusted for the response to along-shelf wind stress, was 38 ± 9.9 mSv. This compares favorably to the magnitude of available freshwater from melting of sea ice and icebergs, meltwater runoff from Greenland, and net P - E. Together these sources can add about 27.5 ± 7.5 mSv to the shelf area during the year.

Fig. 2.14 synthesizes the results of Chapters 2 and 3 schematically, showing the potential paths of the EGCC and its interaction with the EGC and IC at the shelfbreak. More support for this schematic comes in the next two chapters, where we give chemical tracer evidence for the EGCC origins as part of the EGC, as well as the KG as a potential site for EGCC formation.

Chapter 4

The freshwater composition of the East Greenland Coastal Current

4.1 Introduction

The previous two chapters have dealt with the hydrography of the EGCC, its dynamics, and its relation to the EGC south of Denmark Strait. However, the freshwater composition of the EGCC, i.e. what makes it so anomalously fresh compared to the interior of the Irminger Sea, is initially set in the Arctic Ocean itself. The goal of this chapter, then, is to decompose the freshwater composition of the EGCC into quantifiable components and relate them to the circulation of the Arctic Ocean. The freshwater budget given in Chapter 3 was a start, but the methods employed in this chapter will quantify the amounts of sea ice melt and meteoric water (defined here as river runoff, meltwater runoff from Greenland, and net precipitation) that are present in the EGCC and EGC, along with identifying any Pacific Water signal in the current system.

Low-salinity waters exit the Arctic Ocean in two locations: through the west side of Fram Strait in the EGC, and through several small channels and straits of the Canadian

Arctic Archipelago. Although more is known about the former pathway, basic questions still remain about the EGC and its link between the Arctic Ocean circulation and the subpolar North Atlantic to the south. For example, recent observations along the southeast coast of Greenland have revealed a separate branch of the EGC called the East Greenland Coastal Current, EGCC [see Chapters 2 and 3; *Bacon et al.,* 2002; *Sutherland and Pickart*, 2007], which is located inshore of the shelfbreak and advects freshwater equatorward. Presently it is unknown where the EGCC forms, whether it exists year round, and what fraction of the current is due to local (e.g. runoff) versus remote (e.g. the Arctic) sources.

The majority of observations to date of the EGCC are from the summer months, which has limited our understanding of its seasonality and its relationship to the EGC. Nonetheless, hydrographic and velocity data from a series of cruises from 2001-2004 have provided a basic description of the current. The EGCC is characterized by a wedge of low salinity water adjacent to the coast ($S < 34$), which supports an equatorward jet with velocities as strong as 1 m s^{-1} (e.g. Figs. 2.3 - 2.7). The current is approximately 20 km wide, and its spatial scales agree qualitatively with coastal current theory based on mid-latitude river plumes [*Sutherland and Pickart,* 2007; *Lentz and Largier*, 2006]. The volume budget constructed in Chapter 3, which adjusts for the effects of the along-shelf wind, indicated that the combined transport of the undisturbed EGC/EGCC system is approximately 2 Sv. A rough freshwater budget of the region implied that sea ice melt was the biggest contributor to the increased freshwater flux as the current progresses southward.

Bacon et al. [1997] suggested that the EGCC might be formed mainly as a result of meltwater and runoff from the Greenland continent. The more extensive data set noted above suggests that the main part of the flow originates from a bifurcation of the EGC south of Denmark Strait [*Sutherland and Pickart*, 2007]. In particular, when the EGC encounters the Kangerdlugssuaq Trough (Fig. 4.1), a portion of the flow is diverted onshore and continues equatorward along the inner shelf. There is evidence that this is a time dependent process that depends on the strength and spatial scales of the EGC as it encounters the canyon. Chapter 5 below explores this formation process more thoroughly. A similar diversion of water from the shelfbreak to the inner shelf seems to occur farther south as well, associated with the deep canyon near 65.5°N, 38°W that is commonly called the Sermilik Trough (Fig. 4.1). This is suggested from water mass considerations [*Sutherland and Pickart*, 2007] as well from previous drifter studies [*e.g. Centurioni and Gould*, 2004].

The results from the cruises over the last half-decade, together with the historical data analysis of *Wilkinson and Bacon* [2005], indicate that the EGCC is a persistent feature in summertime. There is evidence as well that the current is present year round. *Malmberg et al.* [1967] reported data from a short mooring deployment on the shelf near JR105 section 4 (Fig. 4.1) that suggested an inner shelf flow was present outside of summer, though they identified it as the EGC. Also, several surface drifters released in the winter of 2000 north of Denmark Strait followed the EGC initially [*Bacon et al.*, 2008], but in the northern strait one of them moved onto the shelf and was advected southward by the EGCC (there was a high level of variability most likely caused by the strong winter winds).

Since the EGCC appears to be a branch of the EGC (i.e. it is not simply the result of coastal runoff) and may be present year-round, it likely has a link to the Arctic Ocean. Hence the EGC/EGCC system offers a useful place to examine interannual variations in freshwater entering the North Atlantic from the Arctic. *Steele et al.* [2004] suggested that Pacific Water pathways in the Arctic Ocean might shift under different circulation regimes; these regimes have been shown to be largely controlled by the Arctic Oscillation (AO) [*Proshutinsky and Johnson,* 1997]. This in turn implies that there may be an associated pattern in the freshwater concentrations of the EGC/EGCC. Attempts to relate Pacific Water content of the EGC to changing Arctic Ocean circulation patterns have thus far been inconclusive, however. While significant interannual variability of Pacific Water in the EGC has been observed in the vicinity of Fram Strait [*Jones et al.,* 2003; *Taylor et al.,* 2003; *Falck et al.,* 2005], no relationship to the AO has been found. For example, *Falck et al.* [2005] showed a dramatic diminishment of Pacific Water content from Fram

Strait between 1997 and 2004, but could not relate it to the AO since it was based on only four sections taken between 1984 and 2004.

The main goals of this chapter are two-fold. First, we wish to elucidate the freshwater composition of the EGCC in order to understand better its relationship to the EGC and hence the Arctic Ocean. Second, we aim to quantify the interannual variation of Pacific Water in the EGC/EGCC along southeast Greenland, and relate this to time-varying export pathways from the Arctic Ocean. We apply a suite of methods that have been used previously in the literature, mostly based on tracer techniques [e.g. *Ostlund and Hut*, 1984; *Schlosser et al.* 1994; *Bauch et al.,* 1995; *Jones et al.,* 1998]. These methods are used to calculate the percentages of Pacific Water, Atlantic Water, sea ice melt, and meteoric water, based upon measurements of dissolved nutrients (nitrate and phosphate in particular), oxygen isotopes, salinity, and alkalinity. After examining the EGCC using data from the summer 2004 survey described above [also see *Sutherland and Pickart*, 2007], a compilation of historical hydrographic/tracer sections from the vicinity of Denmark Strait are analyzed to investigate interannual variation of Pacific Water content in the EGC/EGCC from 1984–2004. This is interpreted in light of shifting patterns in the AO.

4.2 Data and methods

The main source of data for the first part of the study comes from a July-August 2004 cruise on the ice-strengthened vessel *RRS James Clark Ross* (JR105) along the transects shown in Fig. 4.1 (blue pluses). Five sections were occupied with a total of 156 hydrographic stations taken at high cross-stream resolution (3-5 km), with a Seabird 911+ conductivity/temperature/depth (CTD) system. Water to measure dissolved oxygen, salinity, and nutrient concentrations was obtained with a 12 x 10 liter bottle rosette. The salinity bottle samples were used to calibrate the CTD conductivity sensor (accuracies are 0.002 for salinity and 0.001°C temperature). Additional details of the hydrographic and velocity data processing are found in section 2.2.

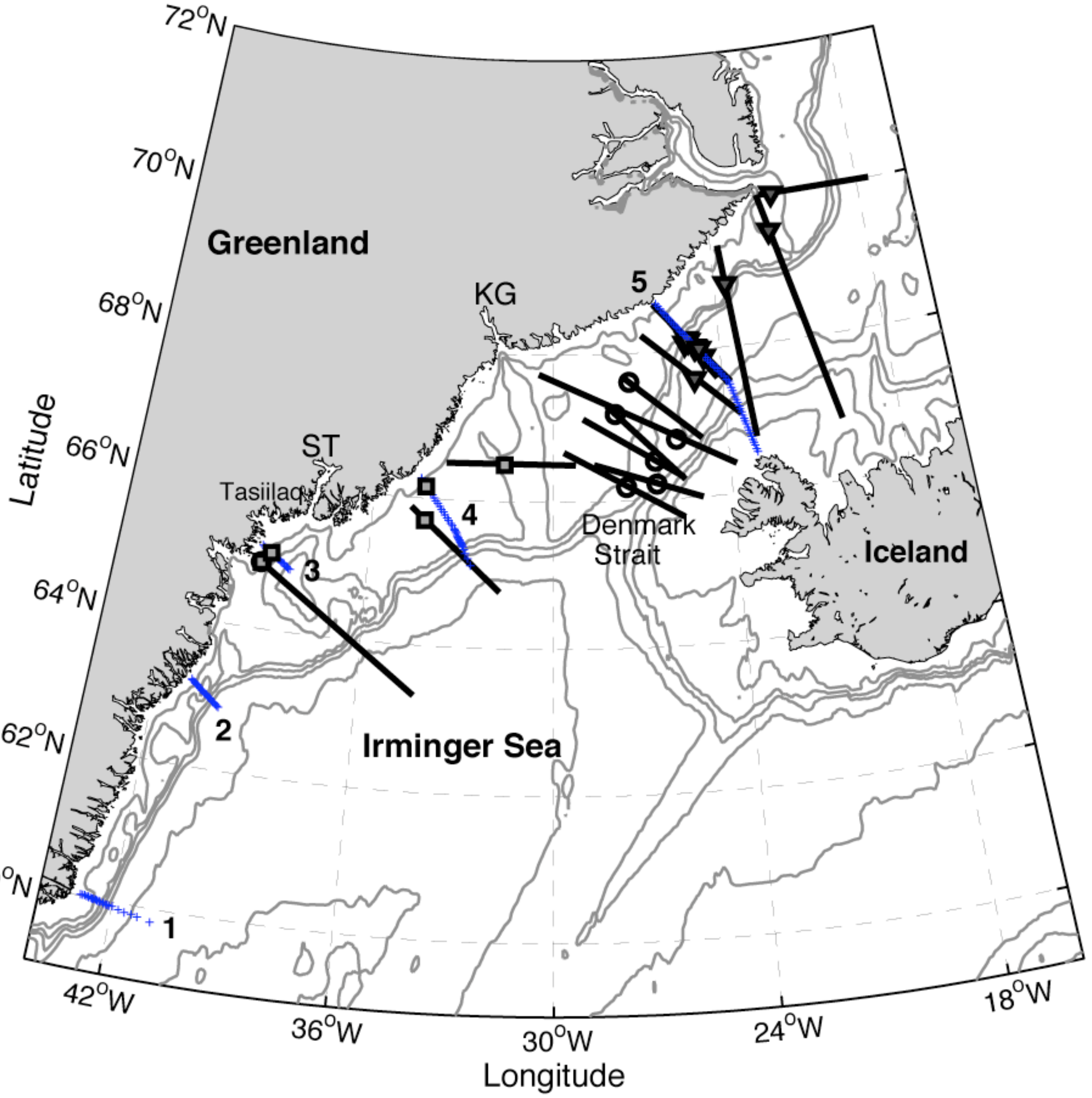

Figure 4.1. Station locations for JR105 (blue pluses) along with section numbers. Black lines show the locations of historic sections where nutrient data were available, coming from several sources [see Table 4.4 for details]. The black marker (square, circle, triangle) indicates the position of the hydrographic front, and hence the EGC or EGCC, for each section, as well as its location (south, sill, north) relative to Denmark Strait. The 200, 400, 1000, 2000, and 3000 m isobaths from the GEBCO database are shown in gray [*IOC, IHO and BODC*, 2003]. KG and ST mark the location of the Kangerdlugssuaq Trough and the Sermilik Trough, respectively.

Nutrients, including nitrate (NO_3), phosphate (PO_4), and silicate (SiO_4), were analyzed immediately on board in duplicate from the bottle samples. The analysis procedure followed the WOCE protocol using a Technicon Autoanalyzer, with precisions close to 1% [*Gordon et al.,* 1993]. Bottle depths were vertically spaced ~25 m apart in shallow water over the shelf (< 200 m deep), while in deeper waters the sample resolution ranged from 100-200 m in the vertical (e.g. see Fig. 4.4-4.6).

Water samples for the determination of oxygen isotope and alkalinity were collected from bottles and analyzed later at the Bedford Institute of Oceanography. Oxygen isotope composition was measured by an equilibrium technique using Micromass Isoprime^{TM} with double injection (two-tier inlet) coupled with an Aquaprep^{TM} system. Data are reported with respect to standard mean ocean water (SMOW) in the $\delta^{18}O$ notation (per mil deviation). An automated open-cell potentiometric titration system was used to determine alkalinity. Alkalinity measurements were calibrated with Certified Reference Material (CRM, Scripps Institute of Oceanography) and the analytical precision was ±4-5 $\mu mol\ kg^{-1}$.

The sampling for oxygen isotope was less frequent than for nutrients, with all of the isotope data derived from bottles shallower than 60 m and at a lower horizontal resolution (i.e. not every station). Less frequent still were samples for alkalinity, which were taken at only 1-2 stations per transect, but were spaced vertically throughout the water column. The effects of these sampling schemes on the results below are minimal, however. Since $\delta^{18}O$ indicates the presence of meteoric waters, such as precipitation or runoff, its utility is limited to the upper water column and the results discussed below seem to capture all the freshwater of meteoric origin (see section 4.3.4). And in the present study, alkalinity is used as a separate tracer only in place of $\delta^{18}O$, in order to assess the sensitivity of the freshwater decomposition results to a particular method.

4.2.1 Analysis methods

The determination of the freshwater composition of a water sample is based upon pre-existing knowledge of that water sample's potential sources. In Arctic Ocean waters, those sources generally include the major rivers that drain into the basin, the inflow from the Pacific Ocean through Bering Strait, sea ice melt, Atlantic-origin water entering through Fram Strait and the Barents and Kara Seas, and any precipitation. Previous studies have used chemical tracers, combined with salinity data, to separate the relative proportions of each freshwater source in a water sample [e.g. *Ostlund and Hut*, 1984; *Bauch et al.,* 1995; *Jones et al.,* 1998]. In particular, the work of *Jones et al.* [2007] and *Taylor et. al* [2003], combined nutrient-based techniques and chemical tracer data to examine the freshwater pathways in the Arctic and along the northeast coast of Greenland. We extend their method to southeast Greenland using data from JR105.

The goal of the freshwater decomposition is to calculate the relative amounts of Pacific Water (PW), Atlantic Water (AW), sea ice melt (SIM), and meteoric water (MW), expressed as fractions. Knowledge of the breakdown in freshwater composition of the EGCC is valuable in understanding its origins, any long-term changes observed in the future, and to aid in the interpretation of the freshwater budget calculated in Chapter 3. The decomposition occurs in two steps. The first is to determine the fraction of Pacific Water. We follow the work of *Jones et al.* [1998], who showed that by examining the nitrate-phosphate (*N-P*) relationship of a polar water sample, the relative amount of Pacific Water could be determined to within ±10%. This technique is successful because as water travels over the shallow Bering Sea shelf entering the Arctic Ocean, it is stripped of its nitrate by biological processes and mixing with nutrient-poor runoff [*Cooper et al.,* 1997; *Jones et al.*, 1998]. This means that a regression line of nitrate versus phosphate will have a different y-intercept (the slope of the regression line is similar for both Pacific and Atlantic-origin waters, since biological processes set the slope in Redfield ratios).

The same biological processes that make the method useful, though, can also be an additional source of error since local denitrification of waters along the EGCC pathway would alter the *N-P* relationship in non-Redfield ratio ways. Also, nitrogen fixation can occur in oxygenated, but nitrate-depleted waters. In addition, the ammonia content of the water may change the total nitrogen concentration, a concept discussed more below along with other uncertainties in Section 4.3.4.

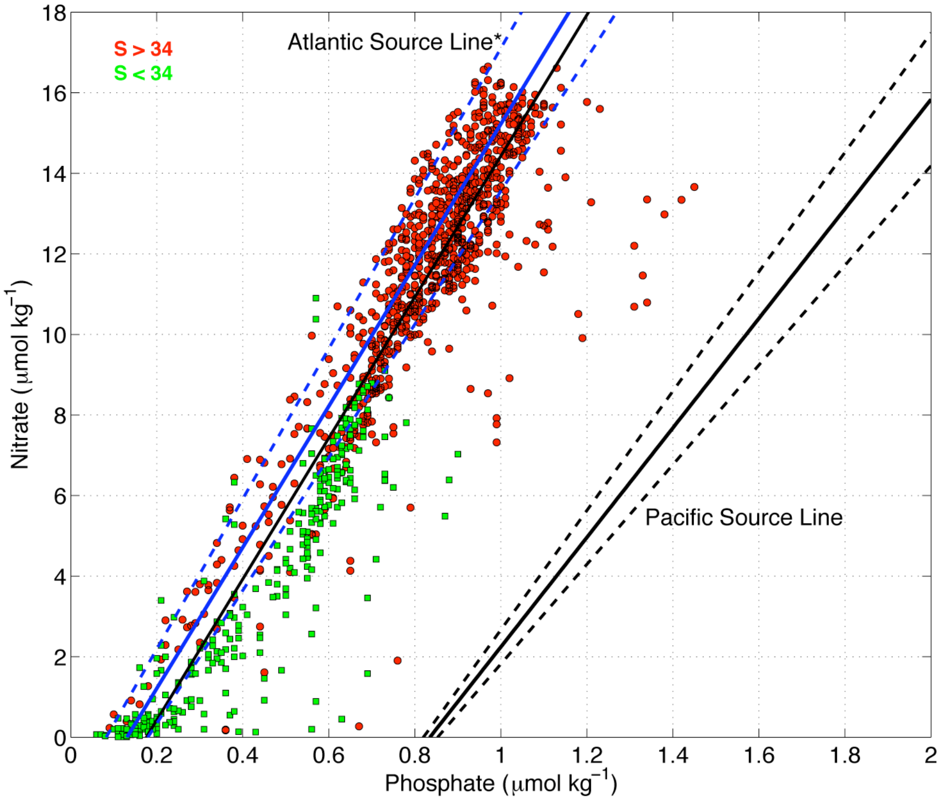

Figure 4.2. Phosphate versus nitrate values for data taken during JR105 in 2004 classified by their salinity (red: $S > 34$, green: $S < 34$). The lines are fits to Atlantic and Pacific source waters with their expected error bounds shown as dashed lines. Blue lines are fit to the 2004 data, while black lines are from *Jones et al.* [2003] for comparison.

Fig. 4.2 illustrates the *N-P* relationship method with the JR105 nutrient data. Dashed lines represent upper and lower bounds (95% confidence intervals) for each source line. This method finds the percentage of PW present in a sample by drawing a mixing line between the PW and AW sources; the latter represents not only AW, but sea ice melt and meteoric waters as well, since SIM and MW have *N-P* relationships that fall close to the AW source line [*Jones et al.*, 1998]. The values of the *y*-intercept and the slope of the PW and AW source lines are listed in Table 4.1, along with their uncertainties.

In practice the fraction of PW, f_{PW}, is calculated using

$$f_{PW} = \frac{PO_4^m - PO_4^{AW*}}{PO_4^{PW} - PO_4^{AW*}} \tag{4.1}$$

where PO_4^m is the measured phosphate value, PO_4^{PW} is the phosphate value the sample would have if it was purely Pacific Water (i.e. on the PW source line in Fig. 4.2), and PO_4^{AW*} is the phosphate value the sample would have if it was Atlantic source water. The star indicates that this Atlantic source water also includes the SIM and MW fractions, since their nutrient relationships are similar.

Table 4.1. End member values (and their uncertainties) used in calculating the Pacific Water fraction, f_{PW}.

	Atlantic Water	Pacific Water
Salinity	35	32.7
NO_3:PO_4 slope	20.7 (±1.4)	12.4 (±2.4)
NO_3:PO_4 intercept	-2.70 (±1.0)	-10.5 (±1.6)

The second step in determining the freshwater composition of a water parcel is to differentiate between the AW, SIM, and MW contributions. This is accomplished using the following set of conservation equations

$$f_{OW} + f_{SIM} + f_{MW} = 1 \tag{4.2}$$

$$O^{18}_{OW} f_{OW} + O^{18}_{SIM} f_{SIM} + O^{18}_{MW} f_{MW} = O^{18}_{m} \tag{4.3}$$

$$S_{OW} f_{OW} + S_{SIM} f_{SIM} + S_{MW} f_{MW} = S_m \tag{4.4}$$

for mass (4.2), salinity (4.3), and oxygen isotope (4.4), where $O^{18}{}_m$ and S_m are the observed values and f_{SIM}, f_{MW}, and f_{OW} are the relative fractions of three unknown water types: SIM, MW, and Oceanic Water (OW). The end member values multiplying the fractions, f, are listed in Table 4.2. To obtain the final fraction of AW, f_{AW}, we subtract the known f_{PW} from f_{OW}. This differs slightly from other methods that solve directly for the AW fraction by reducing the four-component balance to three by using the known PW fraction obtained in (4.1) [*Jones et al.,* 2007]. We show in section 4.3.4 that the difference in the freshwater fractions calculated by these two methods is negligible.

Table 4.2. End member values (and their uncertainties) used in the freshwater composition calculation. The δ^{18}O value is relative to Vienna Standard Mean Ocean Water (VSMOW).

	Oceanic Water	Sea Ice Melt	Meteoric Water
Salinity	34.85 (±0.15)	4 (±1)	0
δ^{18}O (‰)	0.35 (±0.1)	1 (±0.5)	-21 (±2)
Alkalinity (μmol kg^{-1})	2296 (±20)	263 (±20)	1000 (±400)

High-latitude waters of meteoric origins are isotopically light compared to their oceanic counterparts, which makes oxygen isotope data useful as a tracer. Ranges of δ^{18}O values in Arctic rivers, for instance, are -13.3 to -23.8 ‰ [*Ekwurzel et al.,* 2001]. Fig. 4.3*a* illustrates this by showing the δ^{18}O-S relationship for the JR105 data, where any water with a significant fraction of MW will be along a mixing line between OW and MW. The JR105 data show some influence of meteoric water, as well as some influence of sea ice melting and freezing, which tends to change the salinity of the water much more than its isotopic signature (drawn schematically with arrows in Fig. 4.3*a*). Uncertainties in the end-member values for δ^{18}O, listed in Table 4.2, result in the bounds (dashed lines) shown in Fig. 4.3*a*.

The largest uncertainties in the two-step method come in choosing the end-member values for the different source waters. Values in Tables 4.1 and 4.2 are taken from the existing literature [*Jones et al.,* 2003; *Taylor et al.,* 2003; *Ekwurzel et al.,* 2001] with the exception of the AW values. These are estimated from the JR105 hydrographic data set, since in the vicinity of southeast Greenland, the dominant AW source is more likely to be the retroflecting Irminger Current offshore of the shelfbreak [*Pickart et al.,* 2005], than the remote waters of the Nordic or Barents Seas.

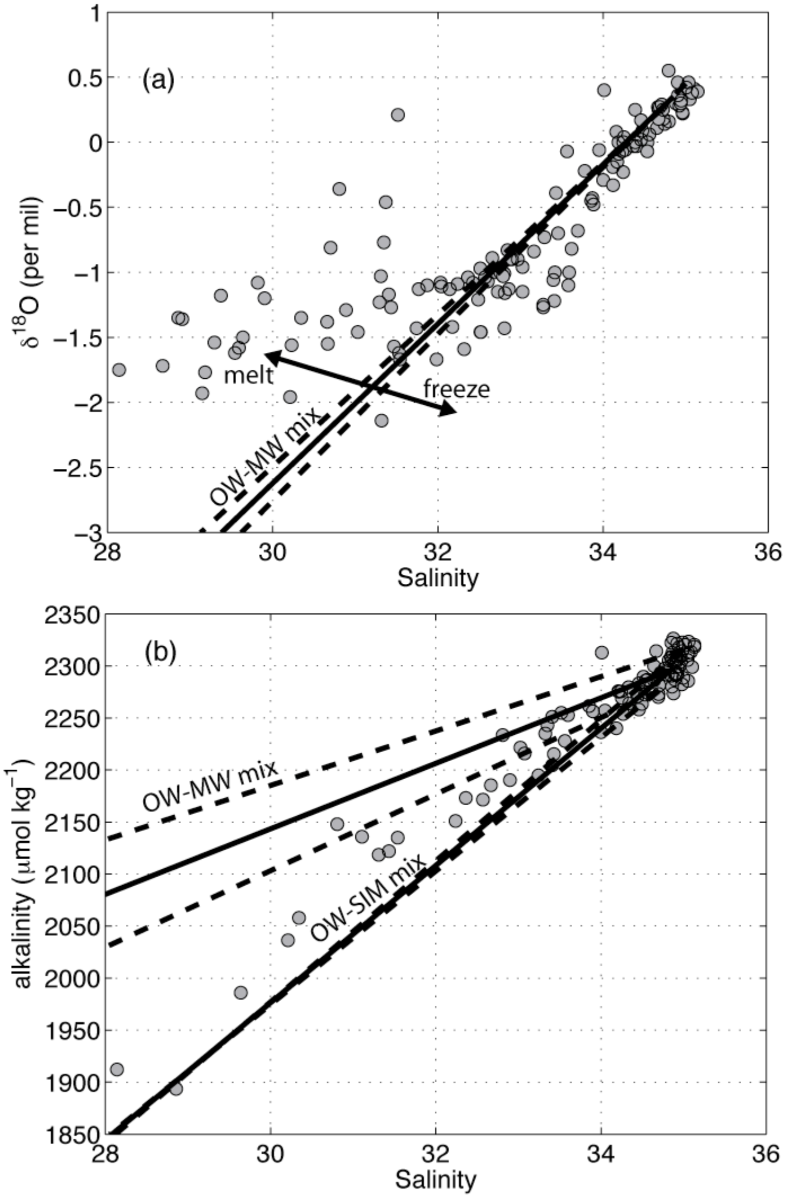

Figure 4.3. *(a)* δ^{18}O versus salinity for JR105 data taken in 2004 (circles). A mixing line (black) between oceanic water (OW) and meteoric water (MW) of zero salinity is shown. Dashed lines show the bounds on the end-member values (Table 4.2). *(b)* Total alkalinity (μmol kg^{-1}) versus salinity for JR105 data taken in 2004 (circle). The upper mixing line is between oceanic water (OW) and meteoric water (MW), while the lower is the mixture of OW with sea ice melt (SIM). Dashed lines show the bounds on the end-member values (Table 4.2).

A more detailed discussion of the uncertainties due to variable end-members is given below in section 4.3.4. We also show a comparison of results using the measurements of alkalinity in place of oxygen isotope in (4.3), where possible, since alkalinity is a good indicator of meteoric water as well. This is illustrated in Fig. 4.3*b*, which shows the alkalinity-salinity relationship using the JR105 data. Note there was considerably less alkalinity data (only 32 samples) available than isotope data. However, the influences of sea ice melt and meteoric water can still be seen in the 2004 data as the measurements fall mainly along either the OW-MW or OW-SIM mixing lines, with some showing the influence of both. Bounds on the mixing lines represent the uncertainties in choosing the end-member values, as listed in Table 4.2.

4.3 Freshwater composition of the EGCC

A primary motivation for this study was to examine the origins of the EGCC by looking at the relative abundances of each freshwater type, determined by the tracer approach described above. If the current were entirely driven by local runoff and ice-melt, then one would not expect to see a signature of Arctic-origin water in the current. We focus on the distribution of Pacific Water in the JR105 sections first, followed by a discussion of the presence of sea ice melt and meteoric water.

4.3.1 Pacific Water

Fig. 4.4 shows the PW fractions calculated for each section (see Fig. 4.1 for section locations), along with the 34-isohaline (dashed lines) and selected contours of the alongstream velocity field (solid lines). The 34-isohaline and the velocity contours indicate the position of both the EGC and /or EGCC features, which should constrain where PW is observed.

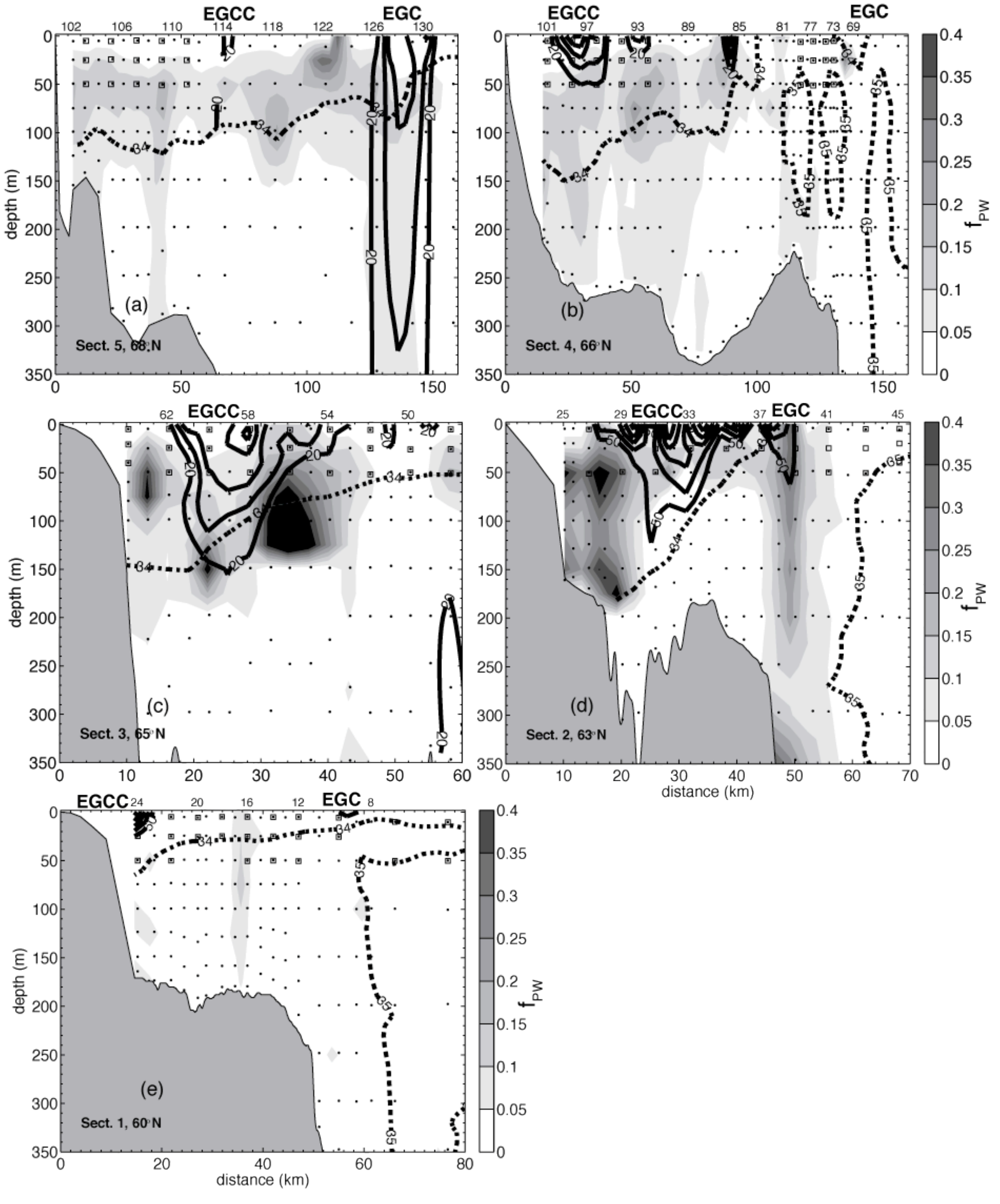

Figure 4.4. *(a-e)* Fractions of Pacific Water, f_{PW} (shading), for each JR105 section along with the 34 and 35 isohalines (dashed lines) and select alongstream velocity contours at 10 cm s^{-1} contour intervals starting with the labeled isotach (solid lines) that indicate the presence of the EGCC or EGC (labeled). Dots indicate nutrient sample locations, while squares are isotope sample locations. Note the horizontal scale changes between panels, but not the vertical scale or color bar. Small numbers refer to the station number.

Starting with the northernmost section near 68ºN (section 5, Fig. 4.4*a*), significant f_{PW}'s are found within the wedge of fresh water ($S < 34$), with the largest values inshore of the EGC. At this latitude, the EGC is situated well offshore in the center of Denmark Strait (see Fig. 4.1). As discussed in previous chapters, there is only a weak signature of the EGCC at this northern location, with slightly enhanced equatorward flow centered at station 114 (near $x = 70$ km in Fig. 4.4*a*). The largest f_{PW} is approximately 0.3, and the average throughout the subsurface layer extending towards the coast is ~ 0.15. Note how the f_{PW}'s are zero near the surface and are eroded in the core of the EGC.

Farther south at section 4 (near 66ºN, Fig. 4.1), similar distributions of f_{PW} are observed (Fig. 4.4*b*). The maximum fraction of PW resides in a subsurface layer within the wedge defined by the 34-isohaline. At this latitude, a strong signature of the EGCC is present over the inner shelf, far inshore of the shelfbreak where the EGC usually resides. Note that there are two velocity peaks associated with the EGCC here, an indication of the EGCC's susceptibility to wind events and its small spatial scales [see Chapters 2 and 3; *Sutherland and Pickart,* 2007]. Associated with each of these separate jets is a subsurface maximum in f_{PW}, suggesting that the PW signal is being carried by the deeper part of the current. The enhanced equatorward flow near the location where the 34-isohaline outcrops ($x = 100$ km) is most likely due to an eddy that contains a mix of northern-origin PW and warm/salty AW from the Irminger Current. Flux of AW onto the shelf at this latitude is commonly observed and is likely related to the formation of eddies either due to the instability of the EGC/IC or by the sinking of the dense overflow water as it exits Denmark Strait [*Pickart et al.* 2005; *Bruce*, 1995]. Two such lenses of Irminger Current water with $S > 35$ (devoid of a PW signal) are situated near the edge of the shelf in Fig. 4.4*b*.

Section 3, located on the inshore side of the Sermilik Trough (ST, Fig. 4.1), shows relatively higher f_{PW} than farther north, but with a similar distribution (Fig. 4.4*c*). Maximum fractions are ~0.3-0.4, but inside the high-speed core of the EGCC the signal is again close to zero, as it was in the main jet features sampled to the north (the EGC was not sampled at this location because the section did not extend far enough offshore).

This reduction of PW fraction is possibly due to an increase in mixing within the jets. This can be tested by looking at the bulk Richardson number, $Ri = N^2 / U_z^2$, of the flow, where N is the buoyancy frequency and U_z is the vertical shear in the horizontal velocity. Values of Ri approaching 0.25 indicate the presence of strong mixing driven by shear instabilities (see Section 2.4.3 for more discussion). Calculation of Ri for the 2004 sections (not shown) suggest that mixing was strong in the EGCC at section 2, particularly on the offshore side, and in section 4, in the center of the EGCC feature.

The reduction in PW is also linked to the additional input of other freshwater components at the surface of the EGC/EGCC as it progresses south along the Greenland shelf (see MW and SIM sections below, Figs. 4.5-4.6). The higher f_{PW} seen at section 3 might be a consequence of the funneling of the EGCC around the Sermilik Trough, i.e. it is a confluence of waters that were spread out farther to the north. At section 2 (63ºN), the shelf reaches its narrowest point, where the EGC and EGCC likely merge to a large degree [see Fig. 2.14]. The distribution of PW shown in Fig. 4.4*d* is similar to that seen at section 3, except for the presence of an eddy-like feature that has significant f_{PW} to depths of 250 m at the shelfbreak. Offshore of this lies AW ($S > 35$), with no PW present.

The biggest change in the f_{PW} distributions measured during JR105 occurs at section 1, off Cape Farewell near 60ºN (Fig. 4.4*e*), where no significant PW fractions were observed. This could be due to a strong presence of Irminger Current water and/or other freshwater components. More likely, the PW signal in the EGC/EGCC system could have been mixed away by the strong winds that regularly occur near Cape Farewell, which help control the structure of the EGCC. As reported in *Sutherland and Pickart* [2007], prior to occupying section 1 the prevailing winds were upwelling favorable. This caused the EGCC to shoal, with its surface signature extending offshore, akin to the manner in which river plumes react to upwelling winds [e.g. *Lentz and Largier*, 2006]. This is seen in Fig. 4.4*e* by the shallow 34-isohaline, which extends beyond the shelfbreak over the AW layer. Only a small velocity signal is seen on the inshore most part of the shelf. This jet is the remnant of the EGCC before the wind event and is also partially the result of continual input of runoff (MW) and sea ice melt. The MW and SIM signals support this idea and are discussed below.

Hence, by Cape Farewell, the PW signal is lost, either due to the thinning of the surface layer and enhanced mixing due to the strong upwelling winds, or to the movement of the PW offshore past the extent of our transect. In summary, during the summer of 2004, the EGCC contained significant fractions of PW, which in turn implies that the current receives significant input from the Arctic-origin EGC. The PW signal was strongest in the subsurface layer and reduced in the core of both the EGC and EGCC. However, the values seen near Denmark Strait (~0.2) were lower than those reported in previous years [*Jones, et al.* 2003; *Dodd*, 2007]. Whether this is due to interannual variability or just the synopticity of the sections is explored below in Section 4.4.

4.3.2 Sea Ice Melt

Fig. 4.5 shows the results of the analysis for sea ice meltwater. Note that the data coverage for calculating f_{SIM} and f_{MW} (below) is less than the coverage for f_{PW}, since that calculation was based on the more frequently sampled nutrients. Squares indicate positions of isotope data, which are all shallower than 60 m. Negative fractions are inferred to mean that net sea ice formation has occurred from that water sample [*Ostlund and Hut*, 1984]. Along the southeast coast of Greenland, most sea ice is advected from the north [*Cavalieri et al.,* 2005], so that any water with $f_{SIM} < 0$ is evidence of polar-origin water that underwent ice formation the previous winter.

This is precisely the case for section 5, north of Denmark Strait, as shown in Fig. 4.5*a*. Values of f_{SIM} ranged from -.04-0, with the most negative values observed inshore of the weak EGCC centered near station 114. Based on hydrographic analysis presented in previous chapters, the surface waters at section 5 were determined to closely resemble Polar Surface Water (PSW), an Arctic-origin water mass modified along its journey by sea ice melt and solar heating [*Rudels et al.*, 2002]. Note that f_{SIM} increases towards zero near the core of the EGCC. Integrated over the upper 60 m, the values of f_{SIM} represent ~2-3 m of sea ice formed.

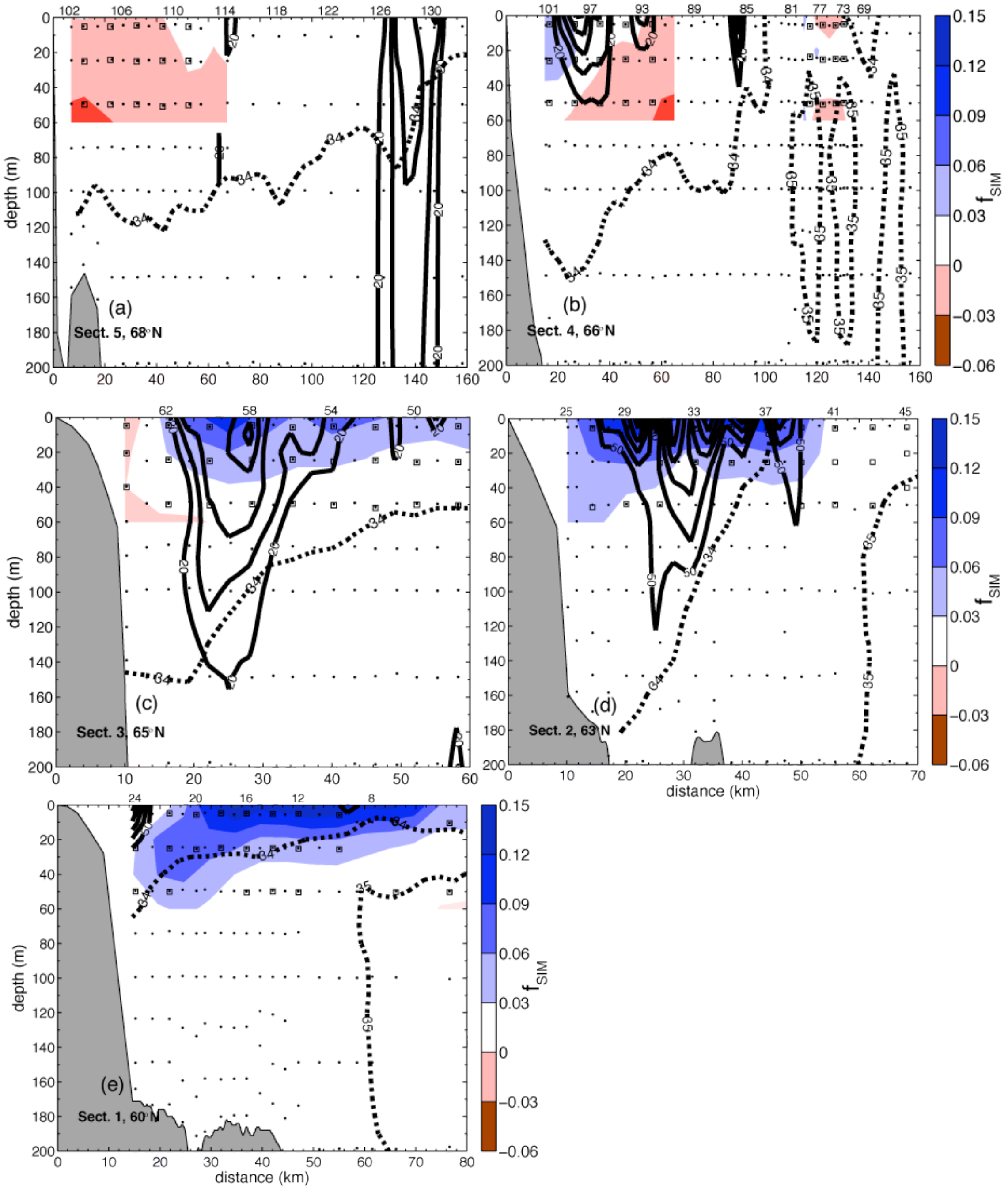

Figure 4.5. *(a-e)* Same as Fig. 4.4, but for fractions of sea ice melt, f_{SIM} (shading), and with a new color scale. Note that the vertical scale has been reduced as well to emphasize the upper water column in all the panels.

Surface waters at section 4, downstream of the Kangerdlugssuaq Trough (Fig. 4.1), reveal the presence of sea ice melt (Fig. 4.5*b*). Values of f_{SIM} are positive closest to the coast, on the inshore side of the main EGCC feature, suggesting that the sea ice advected along with this current has undergone melting. Hydrographic data support this as well with the near surface waters warmer and fresher than at section 5 to the north. Another notable feature at section 4 is the negative f_{SIM} located between the two salty AW lenses near the shelfbreak. This distribution shows that the cross-shelf exchange of AW with fresher, polar-origin water, is a complex process with shelf water getting intertwined with AW filaments.

The sea ice melt process continues to the south over the remaining part of the southeast Greenland shelf. In sections 3 and 2 (Fig. 4.5*c,d*), f_{SIM} values reach ~0.1, with maxima near the core of the EGCC jet and in the upper 20 m of the water column. The deeper extent of positive f_{SIM}'s close to the coast at section 2 is probably a result of the strong downwelling favorable winds that occurred prior to the sampling. These downwelling favorable winds act in the opposite sense of the upwelling winds described above: the current width narrows and the foot of the front deepens as the winds accelerate the current and the Ekman-driven flow drives surface waters toward the coast [see discussion in section 2.4.2; *Lentz and Largier*, 2006].

In section 1 the sea ice melt is observed to extend far offshore (Fig. 4.5*e*), likely a consequence of the upwelling winds that seem to have destroyed the PW signature (as discussed above). Maximum f_{SIM} 's are ~ 0.12-0.15 here, but with no significant levels found inside the EGCC found near x = 15 km. Visual observations during the time of the cruise support this cross-shelf distribution, with floating ice observed far offshore of the shelfbreak.

Previous studies have calculated f_{SIM} near Denmark Strait and Fram Strait. *Dodd* [2007] reported values typically near ~2-3% at Denmark Strait, in line with the observations from section 4 of JR105 (Fig. 4.5*b*). Farther north at Fram Strait, f_{SIM}'s are commonly negative (much like observed in the Arctic) and reached a maximum of ~1-2% in data from the summer of 1998 [*Meredith et al.,* 2001; *Jones et al.,* 2007]. The

JR105 data reveal the importance of melting sea ice to the freshwater composition of the EGC/EGCC system south of Denmark Strait. The meltwater fractions exceed 10% south of 63°N, transforming waters of negative f_{SIM} to waters with positive f_{SIM}.

4.3.3 Meteoric Water

The MW fractions calculated for JR105, and shown in Fig. 4.6, complement the results for SIM and PW discussed above. In general, f_{MW} are greatest at the surface and inshore and decrease towards the open ocean and deeper waters. This observation suggests that the main source of MW to the EGCC is meltwater runoff from Greenland, rather than the influence of Arctic river runoff that would be contained in the EGC as it exits Fram Strait. However, we cannot distinguish between the two MW sources without additional tracers. As such, it is assumed that runoff from Greenland has the same end-member value as Arctic rivers and precipitation. This is justified by the brief discussion of the isotopic signature of Greenland meltwater in Section 4.3.4 below.

The addition of MW to the EGCC is first apparent at section 4 in Fig. 4.6*b*, where f_{MW} reach up to ~ 0.12 on the inshore side of the jet, decreasing offshore. The addition of MW is thus important to the formation of the EGCC, an observation made previously [*Bacon et al.,* 2002]. This meltwater is most likely from the KG fjord region (Fig. 4.1), which is a highly active outlet glacier [*Azetsu-Scott and Tan,* 1997]. Values of f_{MW} are similar at sections 3 and 2 (Fig. 4.6*c,d*), again confined to the near-surface waters. By Cape Farewell, a significant part of the MW signal present farther north is absent (Fig. 4.6*e*), akin to what happened to the PW signal at this location. The MW component is likely much more efficiently mixed into ambient shelf water by the wind as it lies in surface layers primarily. However, the high values seen inshore (near $x = 15$ km) suggest that the 50 cm s^{-1} velocities observed do indicate the EGCC, but in a highly mixed state due to the strong winds prior to the sampling. Recall that almost no PW or SIM was present inside the jet at section 1 (see Fig. 4.4*e*, 4.5*e*).

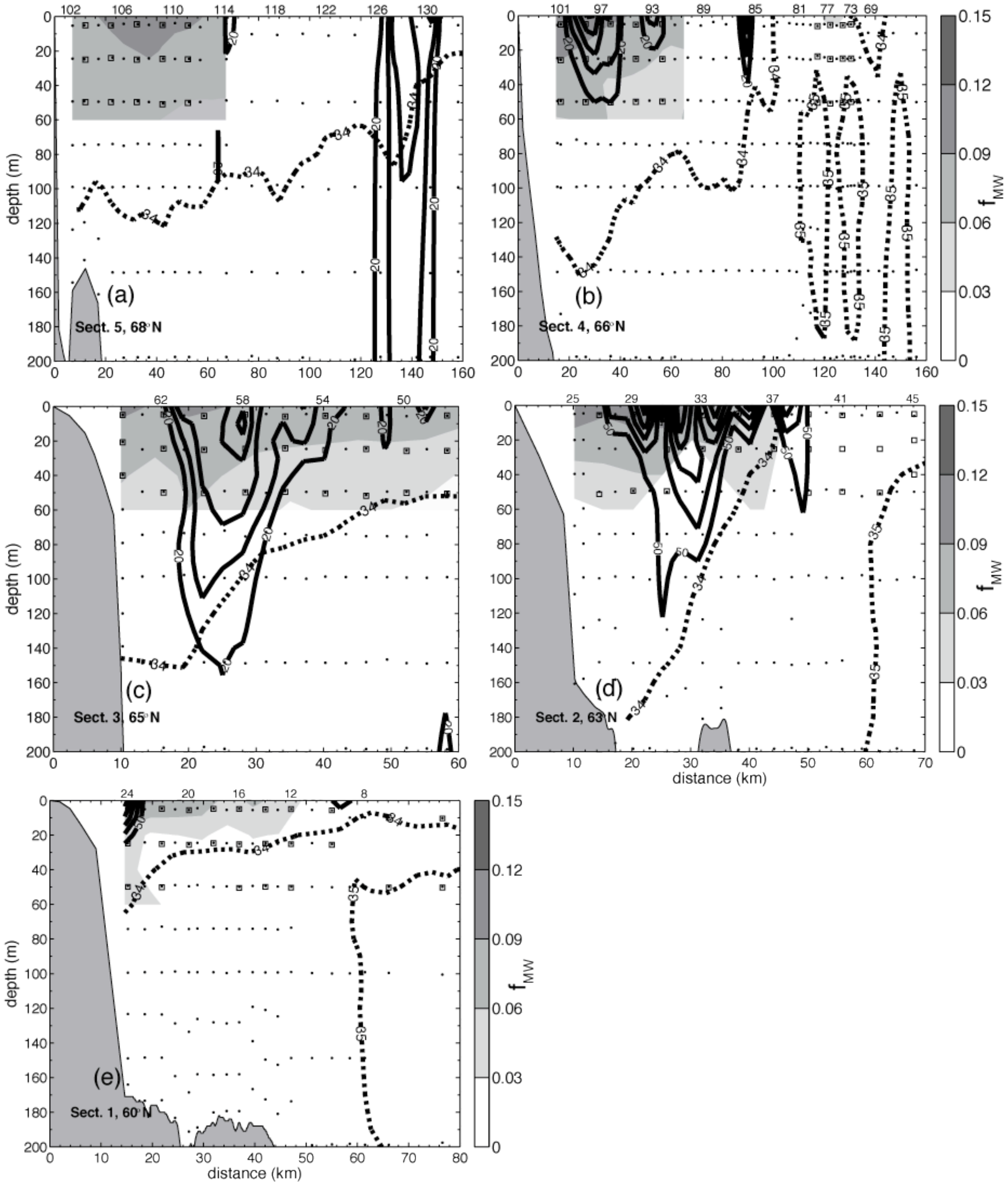

Figure 4.6. *(a-e)* Same as in Fig. 4.5, except for fractions of meteoric water, f_{MW} (shading), are shown with a black and white version of the color scale.

High percentages of MW, $f_{MW} > 10\%$, have been noted before in the EGC near Denmark Strait [*Jones et al.,* 2007; *Dodd*, 2007] and Fram Strait [*Meredith et al.,* 2001; *Taylor et al.*, 2003]. Closer to the Arctic Ocean, the meteoric water fraction represents more riverine water; for instance *Taylor et al.* [2003] found that in 1998 the dominant source of MW in Fram Strait was Eurasian river runoff, where they differentiated between river types by using barium as an additional tracer. Along southeast Greenland however, the input of glacial meltwater is likely just as important a source as the river runoff already present in the EGC.

4.3.4 Uncertainties

The above presentation of the freshwater composition of the EGCC, based on the results of solving (4.1-4.4), was limited to a qualitative description of the relative distributions of PW, SIM, and MW for several reasons. The approach relies on choosing the correct end-member values, which must reflect the bulk water properties (salinity, oxygen isotope, *N-P* relationship) of the source region that can vary seasonally and spatially. Previous studies have done sensitivity analyses to test what variable and/or source water elicits the most change in the composition [*Taylor et al.* 2003; *Bauch et al.*, 1995]. We do not repeat these analyses here for JR105. The biggest errors most likely arise in calculating f_{PW} in (4.1), which are on the order of ±10%. This uncertainty comes about through errors in determining the slope and intercept of the AW/PW lines in Table 4.1 (also see Fig. 4.2), and/or through local processes, such as denitrification or nitrogen fixation, on the Greenland shelves that could modify the nutrient relationships away from the source region definitions. *Jones et al.* [2003] outlines these possible processes affecting the *N-P* relationship.

Given these bounds on the accuracy of the f_{PW} calculation in (4.1), we can test the sensitivity of the remaining freshwater fractions, f_{MW} and f_{SIM}, to the choice of method used above. We do this by showing the difference between the results as calculated above (in 4.2-4.4), versus the results found from two similar, but slightly altered, methods. The first alternate method is exactly the same as outlined above in (4.1-4.4), but uses alkalinity instead of δO^{18} as a tracer of meteoric water. Alkalinity has been used successfully to identify runoff pathways in the Arctic, since the major rivers have been shown to have a unique alkalinity signature, as illustrated previously in Fig. 4.3*b* [*Anderson et al.* 1994; *Anderson et al.* 2004]. The alkalinity end-members used here (see Table 4.2) come from *Anderson et al.* [2004], although the published range for Arctic rivers is ~800-1400 μmol kg^{-1} [*Jones et al.* 2007; *Anderson et al.* 1994]. The alkalinity value for glacial meltwater is uncertain, so again we assume the value is the same as for rivers and precipitation.

The second method used for comparison is again similar to the steps taken in (4.1-4.4), but solves the four-component balance for f_{PW}, f_{AW}, f_{MW}, and f_{SIM} directly. This is done by using (4.1) to calculate f_{PW}, then taking the terms associated with it in (4.2-4.4) to the right hand side and replacing f_{OW} with f_{AW}. The salinity end-member values for AW and PW, listed in Table 4.1, come from the existing literature, as do the δO^{18} values chosen, which -1‰ and 0.35‰ for PW and AW, respectively [*Bauch et al.,* 1995; *Ekwurzel et al.,* 2001; *Jones et al.,* 2003]. This is the method employed by *Jones et al.* [2007], except we utilize δO^{18} conservation instead of alkalinity.

Table 4.3 lists the results of this sensitivity analysis in terms of the difference between the calculated f_{MW} and f_{SIM} for each new method relative to the original method. In both cases, the original f_{SIM} values are greater than those found with the alternate methods, while the original f_{MW} were are less. Whether this implies that the original method is biased to give slightly higher (lower) fractions of SIM (MW) is an important question. However, the range of mean differences found, -0.015-0.036, is small compared to the limits on the accuracy of calculating f_{PW} discussed above. It is also comparable to changes observed in the sensitivity analyses of previous studies, on the order of ~5% [*Taylor et al.,* 2003; *Bauch et al.*, 1995].

Table 4.3. Means and standard deviations of the difference (Δ) in f_{MW} and f_{SIM} using two additional methods discussed in the text. (*Alk-O18*) is based on 32 stations, spread over all the sections, where both tracers were measured, while (*AW - OW*) used the data used in the calculation of 4.1 - 4.4.

	$(\Delta f_{SIM})_{\text{Alk-O18}}$	$(\Delta f_{MW})_{\text{Alk-O18}}$	$(\Delta f_{SIM})_{\text{AW-OW}}$	$(\Delta f_{MW})_{\text{AW-OW}}$
Δ_{mean}	-0.015	0.036	-0.01	0.011
$\Delta_{std.dev.}$	0.03	0.04	0.01	0.01

Numerous other tracers have been utilized in the past to examine Arctic freshwater pathways, including silicate [*e.g. Stefansson* 1968; *Codispoti and Lowman* 1973; *Anderson et al.* 1994], the ratio NO/PO [*Wilson and Wallace* 1990], PO_4* [*Ekwurzel et al.* 2001], and barium [*e.g. Taylor et al.* 2003; *Dodd* 2007]. Adding these tracers to this analysis, however, would introduce more uncertainties since silicate (as does nitrate, phosphate, and barium) levels depend on biological activity, and NO/PO and PO_4* are not suitable for near surface waters where oxygen can be exchanged with the atmosphere.

Without more information on the variability of the EGCC and its freshwater sources, a more quantitative analysis is unwarranted, although several recent studies have begun to make progress in unraveling these variations. *Yamamoto-Kawai et al.* [2007] have shown the importance of using the total dissolved inorganic nitrogen content (DIN), which includes ammonia as opposed to nitrate only, in calculating PW fractions offshore of the Chukchi Sea shelf in the Arctic Ocean. A more complete suite of measurements including total DIN should improve the accuracy of the f_{PW} calculation to better than 10%, as well as accounting for apparent $f_{PW} > 100\%$ reported in the southern Canada Basin. As noted above, it has also been assumed that meltwater runoff from Greenland, included as meteoric water in this study, has the same end-member values as the river runoff and precipitation parts of MW. A start on assessing this issue has been done using oxygen isotope measurements from the KG fjord glacier system (Fig. 4.1). The 1993 cruise reported by *Azetsu-Scott and Tan* [1997], and the 2004 cruise discussed by *Dodd* [2007], both had extrapolated $\delta^{18}O$ values near -20 ‰ (with variations of ±1-4‰), which are comparable to the variations seen in MW measurements taken from the Arctic [*Bauch et al.* 1995].

4.4 Interannual variability in the Pacific Water signal

The usefulness of calculating the fraction of Pacific Water in the EGC/EGCC system extends beyond investigating the origin of the water masses it advects. Once the EGC exits Fram Strait with its PW signature, it carries with it information on aspects of the Arctic Ocean circulation prior to that time. While *Jones et al.* [2003] reported f_{PW}'s that were consistently near ~90% from 1997-1999 in the vicinity of Fram Strait, *Taylor et al.* [2003] noted that data from 1987 showed a maximum of only 52% PW. Recently, *Falck et al.* [2005], showed that the PW fraction decreased dramatically in 2004 north of Greenland, compared to similar sections taken in 1984, 1990, and 1997. In light of such time-varying PW fractions in the vicinity of Greenland, it is worthwhile to try and link these interannual variations to possible changes in Arctic export pathways.

What controls the amount of Pacific Water present in the EGC? *Steele et al.* [2004] argue that the PW pathways in the Arctic are strongly affected by the Arctic Oscillation (AO), which is defined as the leading mode of an empirical orthogonal function decomposition of the 1000-mb pressure field over the wintertime northern hemisphere [AO data available at *http://www.cpc.ncep.noaa.gov/*]. In particular, during persistent positive AO phases, the anticyclonic Beaufort gyre weakens and shrinks in size, allowing more PW to leak along the boundary towards Fram Strait as well as via the Transpolar Drift Stream (see Fig. 4.10 below). When the AO switches to a strongly negative state, the enhanced Beaufort gyre effectively limits the amount of PW that can cross the Arctic basin, and the PW input is either stored in the large gyre or is drained preferentially through the Canadian Arctic Archipelago (CAA). These two states of the Arctic Ocean were described in detail by *Proshutinsky and Johnson* [1997], who focused mainly on the surface circulation and sea ice drift that are linked directly to the atmosphere. In the Arctic, PW is found from the surface to depths of 250 m, so its circulation is directly linked to the atmospheric circulation as well.

Three types of Pacific Water occupy portions of the Arctic Ocean halocline [e.g. *Coachman et al.,* 1975; *Shimada et al.,* 2001*; Steele et al.,* 2004]. Following the nomenclature of *Steele et al.* [2004], these are: summer Bering Sea Water (sBSW), Alaskan Coastal Water (ACW), and winter Bering Sea Water (wBSW). These different PW types form by different processes and in different seasons, and are believed to spread in distinct pathways, though they all occur in water depths less than 200 m and seem to respond to AO forcing [*Steele et al.* 2004]. Importantly, these halocline waters make up part of the subsurface EGC as it exits Fram Strait, with Polar Surface Waters in the most near surface layer [*Rudels et al.,* 2002]. In the Arctic Ocean, the geographical boundary between the influence of Pacific-origin waters and Atlantic-origin waters is usually defined by the Transpolar Drift Stream, the cross-Arctic flow that has been shown to respond to changes in the AO index. [*e.g. McLaughlin et al.,* 1996]. These shifts in the axis of the Transpolar Drift Stream, and the fact that correlations between the Arctic Ocean circulation above 200 m and the atmosphere reach up to 80% [*Proshutinsky and Johnson,* 1997], strongly suggest that the distribution and advection of PW is causally linked to the seesawing AO index. This connection is illustrated in Fig. 4.10 below where it is discussed in reference to Section 4.4.2.

It is worth noting that *Falck et al.* [2005] found no significant correlation between the “disappearance” of PW at Fram Strait in 2004 (when the maximum f_{PW} was ~20%) and the relatively larger percentages found previously, with the AO index. However, their study considered only a small number of sections, limiting their ability to make such a comparison. Since we showed above that there is a strong PW signal in the EGC/EGCC system along southeast Greenland, we can test again the relationship between the AO index and the PW signal in the vicinity of Denmark Strait, where there is a relative abundance of nutrient data compared to Fram Strait.

The interpretation of the time-varying PW signal at Denmark Strait should be no more complicated than for data collected near Fram Strait. This is because the transit time from Fram Strait to Denmark Strait is fairly quick for EGC waters, taking on average ~6-9 months (based on an average speed of ~ 0.1 m s^{-1}). This is short compared to residence times estimated for the Arctic Ocean, which are on the order of a decade [*e.g. Schlosser et al.,* 1994; *Ekwurzel et al.,* 2001; *Steele et al.,* 2004]. The exact timing is likely more complicated, since for example, part of the EGC feeds the gyre situated over Belgica Bank that forms the Northeast Water Polynya. This may act to delay the propagation of the PW signal down the coast [*Budeus et al.,* 1997; *Falck*, 2001]. This is discussed further below once the PW results are presented for the time series data from Denmark Strait. We do not discuss in detail the specific components of PW that are commonly identified in the Arctic, such as sBSW or wBSW. This is because their identification relies upon examining θ/S relationships that are most likely eroded by the time the EGC reaches Denmark Strait. We instead focus on the quantification of the PW fraction by means of the nitrate-phosphate relationship method, since this should still succeed in separating the PW from the Atlantic-influenced waters (which also includes sea ice melt and river runoff).

4.4.1 Calculation of the Pacific Water signal

The data are taken from twenty-four sections that included nitrate, phosphate, temperature, and salinity measurements. The locations of the sections are shown in Fig. 4.1 (black lines), identified by their proximity to Denmark Strait as either northern (shaded triangles), sill (open circles), or southern (shaded squares) sections. They include sections 3-5 of JR105 that were discussed above in detail, and cover the time span of 1984, 1987-1999, 2002, and 2004. The 2002 data come from a May cruise aboard the *IB Oden*, reported on extensively by *Jones et al.* [2007]. The 1998 data are from the ARK-XIV2 expedition aboard the *R/V Polarstern*, and have been previously discussed by several authors [*Meredith et al.* 1998; *Taylor et al.* 2003*; Dodd* 2007]. The rest of the data come from *Jones* [pers. comm., 2007] and from the archives of the National Oceanographic Data Center [*Boyer et al.* 2006; data available at *http://www.nodc.noaa.gov/*]. Most of the northern sections are from Icelandic repeat cruises along the standard Kögur section; for details of each cruise see Table 4.4.

Table 4.4. List of cruises from which nutrient data was obtained (via pers. comm. or the NODC [*Boyer et al.,* 2006]) for use in examining Pacific Water signals in Section 4.4. References are given when available.

Year	Month	Location[a]	# stations (*dx*)[b]	Vessel (program)[c]	notes [d]
1984	Sept.	North	4 (40 km)	*Prof. Multanovskyi*	USSR
1987	Sept.	North	5 (20-40 km)	*B. Sæmundsson*	Iceland
1988	Sept.	North	5 (20-40 km)	*B. Sæmundsson*	Iceland
1989	Sept.	North	5 (20-40 km)	*B. Sæmundsson*	Iceland
1990	Sept.	North	5 (20-40 km)	*B. Sæmundsson*	Iceland
1991	Sept.	North	5 (20-40 km)	*B. Sæmundsson*	Iceland
1991	Sept.	Sill	20 (20 km)	*B. Sæmundsson*	Iceland
1993	Aug.	Sill	12 (15 km)	*B. Sæmundsson*	Iceland
1994	Sept.	Sill	10 (20 km)	*B. Sæmundsson*	Iceland
1996	Oct.	North	8 (30 km)	*B. Sæmundsson*	Iceland
1996	Nov.	South	50 (6 km)	*Knorr* (WOCE)	International
1997	Aug.	Sill	11 (10 km)	*Aranda* (VEINS)	Finland
1997	Sept.	Sill	14 (10 km)	*Aranda* (VEINS)	Finland
1997	Oct.	North	8 (30 km)	*B. Sæmundsson*	Iceland
1998	Oct.	North	13 (20 km)	*Polarstern* (VEINS)	*Dodd* [2007]
1998	Oct.	Sill	9 (20 km)	*Polarstern* (VEINS)	*Dodd* [2007]
1998	Oct.	South	10 (20 km)	*Polarstern* (VEINS)	*Dodd* [2007]
1999	Sept.	Sill	3 (25 km)	*B. Sæmundsson*	Iceland
2001	Aug.	Sill	1 (N/A)	*B. Sæmundsson*	Iceland
2002	May	North	10 (30 km)	*Oden*	*Jones et al.* [2007]
2002	May	Sill	6 (30 km)	*Oden*	*Jones et al.* [2007]
2002	May	South	8 (30 km)	*Oden*	*Jones et al.* [2007]
2004	Aug.	North	33 (5 km)	*James Clark Ross*	Sect. 5 in Fig. 2.1
2004	Aug.	South	37 (5 km)	*James Clark Ross*	Sect. 4 in Fig. 2.1
2004	Aug.	South	19 (5 km)	*James Clark Ross*	Sect. 3 in Fig. 2.1
1998	Sep.	Fram Strait	23 (10 km)	*Polarstern* (VEINS)	*Meredith* [2001]
1998	Sep.	75°N	12 (20 km)	*Polarstern* (VEINS)	Germany
1999	Sep.	Fram Strait	16 (15 km)	*Polarstern* (VEINS)	*Taylor et al.* [2003]
1999	Oct.	75°N	6 (20 km)	*Polarstern* (VEINS)	Germany
2002	May	Fram Strait	8 (20 km)	*Oden*	*Jones et al.* [2007]

[a]: Location is relative to the Denmark Strait area (Fig. 4.1) or indicates Fram Strait or 75°N.
[b]: This is the number of stations used in the PW_{equiv} calculation and the average horizontal spacing, *dx.*
[c]: WOCE: World Ocean Circulation Experiment; VEINS: Variability and Exchange in the Nordics Seas.

Vertical and horizontal resolutions varied from section to section (Table 4.4), but they all captured the presence of the EGC (or EGCC in the southern sections) front, with fresher/colder water inshore of the saltier and warmer waters of Atlantic influence. The position of the front is shown for each section in Fig. 4.1, defined as the location where the maximum equatorward geostrophic velocity, calculated from the θ/S data and referenced to the bottom, was found. This velocity criterion agreed well with the position of the sharpest sloping isohalines, another indicator of the EGC front (e.g. see Fig. 4.4-4.6). In general, the frontal position was located near the shelfbreak north of Denmark Strait, but varied in position near the sill, either close to the shelfbreak on the Greenland side or in the middle of the strait. An offshore veering of the EGC as it crosses over the sill is commonly observed, as is true for the Denmark Strait overflow [*J. Girton*, pers. comm., 2007]. Downstream of the sill, the main front is shifted inshore as the EGC splits into the inner shelf EGCC and the shelfbreak EGC.

To quantify the amount of PW present at each section we followed the first step of the freshwater decomposition outlined above, i.e. using Eqn. (4.1). However, the AW* source line was determined for each section independently before solving (4.1). This was done by fitting a line to the N-P data from each section that had $S > 35$, a proxy for AW. Fig. 4.7 shows the composite nitrate-phosphate relationship for all the Denmark Strait sections (yellow circles), and demonstrates why this extra step was necessary. Without accounting for changes in the AW* source line, the estimated f_{PW}'s could be biased. We emphasize, though, that the shifting of the AW* line never exceeded the upper and lower bounds (dashed lines in Fig. 4.7) estimated previously from the JR105 data. In essence, this step tries to account for variability in the AW* nutrient relationship, and should be done for the PW line as well. Since our data are far from the PW source region however, it is impossible to derive a PW fit for each year based only on data from that section. We assume therefore, that the one PW line shown in Fig. 4.7 is satisfactory for all the data, within its estimated upper and lower bounds.

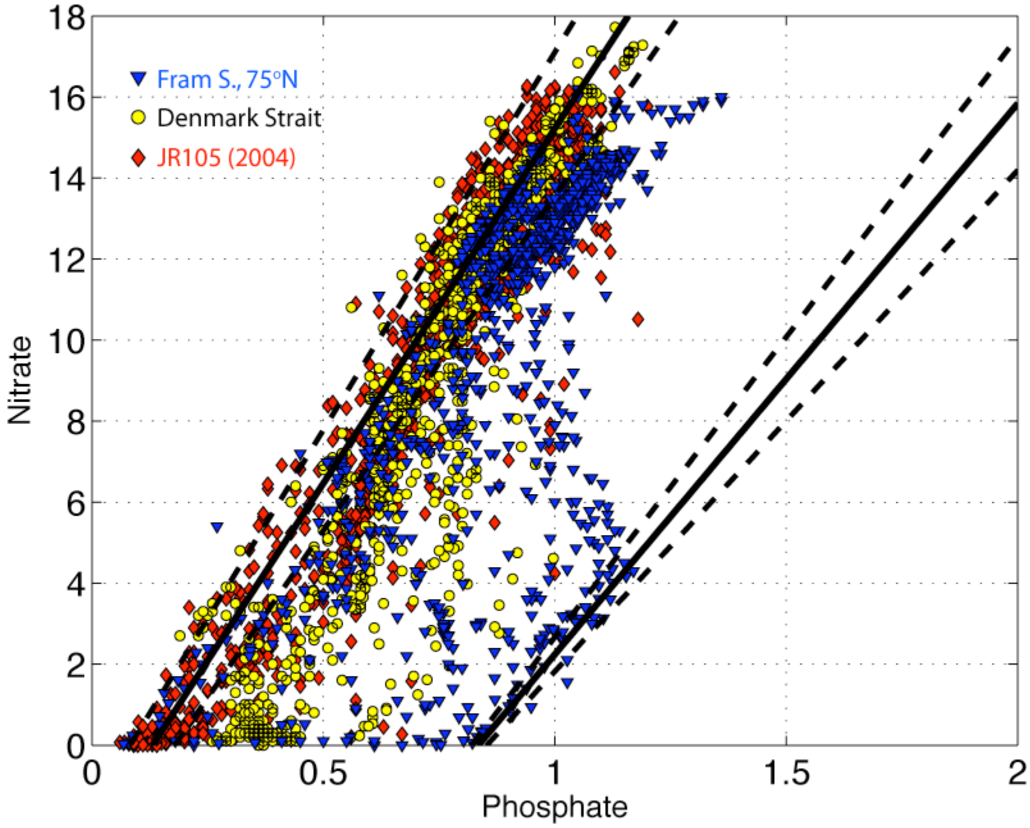

Figure 4.7. Phosphate versus nitrate values for all years of Denmark Strait data (yellow circles) and Fram Strait data (blue triangles). JR105 measurements are shown for comparison (red diamonds), as are the fits to Atlantic and Pacific source waters (black lines), which are the same as in Fig. 4.2.

Once the f_{PW} is calculated for each section, we then convert it to its freshwater equivalent value

$$f_{PW}^{fresh} = f_{PW}\left(1 - S_{PW}/S_{AW}\right) \qquad (4.5)$$

referenced with S_{PW} and S_{AW}, which are the salinities of Pacific Water and Atlantic Water respectively (Table 4.1). The total fresh water equivalent relative to the AW salinity can be calculated as

$$f_{total}^{fresh} = 1 - S_m/S_{AW} \qquad (4.6)$$

where S_m is the measured salinity. We use these instead of f_{PW} from (4.1) to facilitate comparison with other studies, which report PW freshwater inventories. With these variables defined, we have vertical sections of PW freshwater equivalent and total freshwater (FW) content for each year and location.

It is necessary to account for the variations in the coverage of each section over the relevant current feature, e.g., whether or not the entire EGC was captured at the sill sections, since those transects did not survey all the way to the coast (Fig. 4.1). We accomplish this by first integrating f_{PW}^{fresh} and f_{total}^{fresh} in the vertical (0-200m) to get column inventories of PW and FW equivalent (in meters). Next we integrated these in the horizontal to get an area of PW and FW equivalent (m^2). These values were then normalized by dividing by the horizontal extent of the current feature captured, either the EGC in the north and sill sections, or the EGCC in the southern sections. The final normalized PW and FW equivalent inventories are thus defined as

$$PW_{equiv} = \frac{1}{L} \iint_{dx,0-200m} f_{PW}^{fresh} dz dx \tag{4.7}$$

$$FW_{equiv} = \frac{1}{L} \iint_{dx,0-200m} f_{total}^{fresh} dz dx \tag{4.8}$$

where L is the estimated horizontal extent of the current (in meters). This provides a single value for each year/section that can be meaningfully compared, reflecting the amount of PW or FW present. The one exception to this is the 2001 cruise in the sill region, which contained only a single station. For that station, we assumed the data represented a horizontal extent comparable to the station spacing of a similar cruise to that area undertaken in 1999 (see Table 4.4), i.e. $L \sim 25$ km. This normalization introduces the largest uncertainties in the sill sections, since these were the only ones that did not capture the entire current feature, and thus, these PW_{equiv} values have the largest error bars.

Fig. 4.8 displays the results of the calculation for PW_{equiv}, grouped by the section's proximity to Denmark Strait. The range over all years is ~0.5-3.5 m, which is much more than the estimated uncertainty of each value. The uncertainties (shown as error bounds in Fig. 4.8) are found by combining an estimate of the standard error with the initial 10%

uncertainty assumed in calculating f_{PW} in (4.1). The standard error accounts for the synoptic variability, such as observed in years in which two or more sections were taken close to each other in time and location (e.g., 1997, 2004 in Fig. 4.8). An additional 10% error is factored in for the sill section values to represent the additional uncertainty in estimating L there, as discussed above. The fact that the temporal trends in PW_{equiv} from different locations co-vary supports the robustness of the method and the high quality of the data.

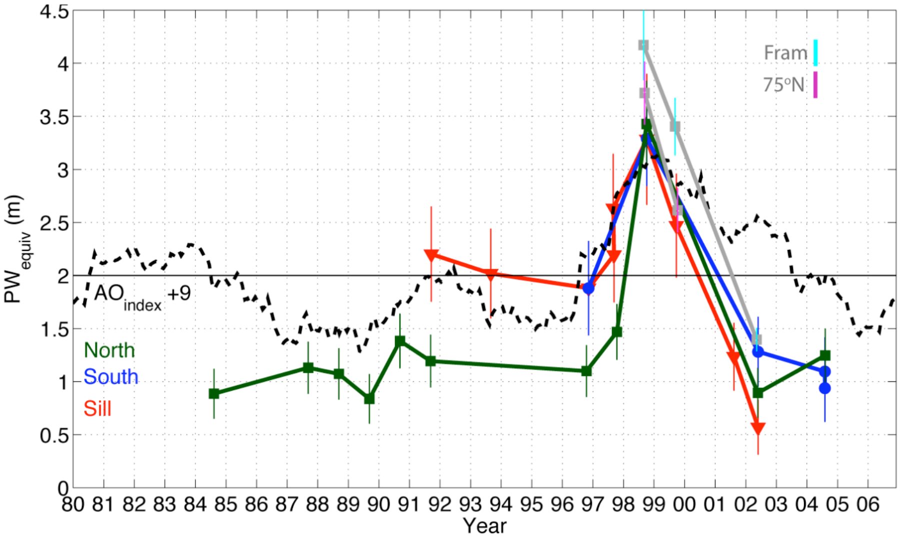

Figure 4.8. Normalized Pacific Water freshwater equivalent inventory, PW_{equiv} (m), as a function of time. The 24 sections from the Denmark Strait area are grouped by location as either northern (green squares), sill (red diamonds), or southern (blue circles). Five sections taken from north of Denmark Strait (Fram Strait and 75ºN) are shown in gray for comparison. The black dashed line is the 3-year running mean of the wintertime Arctic Oscillation index ($AO_{index}+9$), lagged 9 years.

The most striking feature in Fig. 4.8 is the large increase in PW_{equiv} observed in the later 1990s, where it reached values of 3.2-3.4 ± 0.4 m. The subsequent dramatic decrease supports the observations of *Falck et al.* [2005] at Fram Strait, where a correspondingly large decrease in PW abundance was found in 2004. Several additional sections from the 2002 *Oden* cruise, located between Fram Strait and Denmark Strait, also showed similarly low proportions of PW present [*Jones et al.,* 2007]. To make sure the large pulse in Fig. 4.8 was not predominantly the result of a single anomalous cruise in Denmark Strait in 1998, we calculated PW_{equiv} and FW_{equiv} from five additional sections occupied north of Denmark Strait in the years 1998, 1999, and 2002. Three of these additional sections come from Fram Strait (the 1998 is from the same cruise as the 1998 Denmark Strait sections), and the other two were occupied across the EGC at 75ºN (1998, 1999). See Table 4.4 for cruise details for each section. The *N-P* relationships of these additional data are displayed in Fig. 4.7 and indicate the presence of some "pure" PW at Fram Strait.

The PW_{equiv} values from these northern sections are plotted in Fig. 4.8 (gray lines) in addition to the Denmark Strait data, and match up well with the observations from farther south (keep in mind the short advective time from Fram Strait to Denmark Strait). This supports the notion that the PW signal in the EGC was indeed enhanced in the late 1990s. The fact that the PW fraction generally decreases from Fram Strait to Denmark Strait in a given year (e.g. 1998, 2002) is evidence that the method produces a meaningful signal, and that PW is being mixed away as it traverses southward along the Greenland shelf. The trend of lower PW_{equiv} in northern sections compared to sill sections in the years 1991, 1993, 1996, and 1997 possibly reflects the higher uncertainty in the sill section values, but also the potential that part of the EGC is offshore of the northern sections as it approaches Denmark Strait. This would result in lower values for the northern sections. It might also be due to a sampling bias in the northern sections, which during this time period had the lowest spatial resolution and may not have captured the full PW signal. The normalization in (4.7-4.8) would not account for this type of error.

4.4.2 Link to the Arctic Oscillation

We examine next the correlations between the PW signals in Fig. 4.8 and the wintertime Arctic Oscillation. The 3-year running mean AO index, lagged by 9 years, is included in Fig. 4.8. One immediately sees the intriguing relationship between the lagged AO and the trends in PW_{equiv}. In particular, the AO displayed a similar sharp peak roughly a decade earlier. To investigate this more quantitatively, we linearly regress the values of the AO index with different variables associated with the EGC. Fig. 4.9*a,b* show the results of those correlations. The maximum correlation between PW_{equiv} and the AO was found to be $R = 0.62$ with a lag of 9 years. This is significant at the 95% level (*p*-value) for 15 degrees of freedom (one for each year where data was available). No significant correlation was found between the AO index (at any lag) and the FW_{equiv} values. Fig. 4.9*b* shows the two variables plotted against each other for the AO index plus 9 years. The lack of significant correlation between the freshwater content of the EGC and the AO index is most likely caused by local and seasonal effects that change the amount of freshwater stored in the water column. The major process is sea ice melt during the warmer months, which greatly lowers the salinity of surface waters.

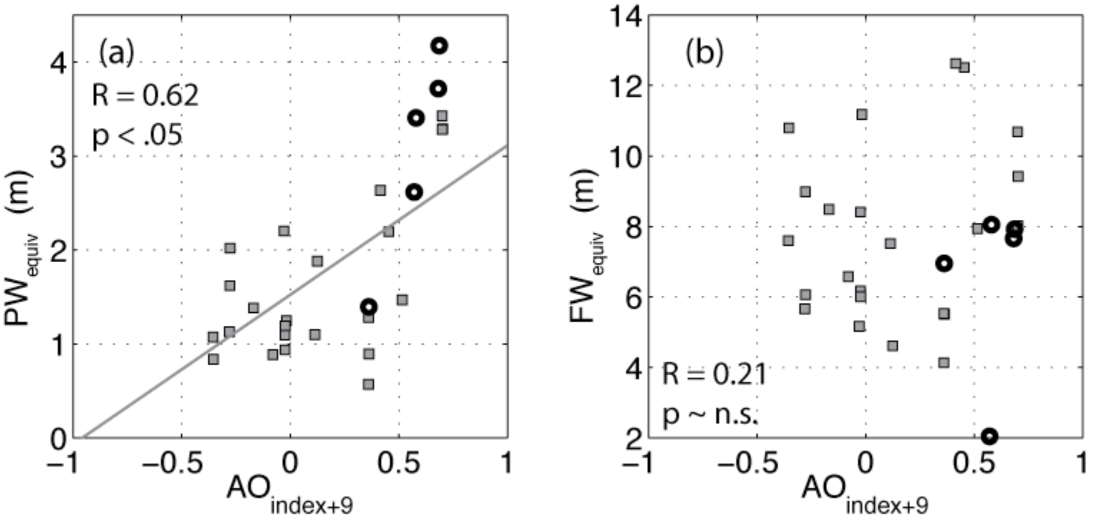

Figure 4.9. *(a)* Correlation of the normalized PW inventory, PW_{equiv} (m), from the Denmark Strait sections (gray squares) and the 9-year lagged wintertime AO index. The best-fit regression line to these data is shown in gray. Black circles show the corresponding values for the Fram Strait and 75ºN sections. Correlation coefficients (*R*) and the significance of the correlation (*p*) are shown. *(b)* Same as in *a* except for the normalized FW inventory, FW_{equiv} (m), which showed no significant correlation.

We believe that the significant correlation between the PW_{equiv} and the lagged AO index reflects a difference in the pathways and mixing history of the Pacific Water resulting from changes in the predominant atmospheric forcing of the Arctic, as discussed above and shown schematically in Fig. 4.10, which is taken from *Steele et al.* [2004]. In the positive AO state (weak Beaufort gyre), there is a more direct route for Pacific-origin water to enter Fram Strait via the transpolar drift, and hence one would expect a stronger presence of PW in the EGC (larger values of PW_{equiv}). In the negative AO state (stronger Beaufort gyre), *Steele et al.* [2004] argue that more of the Pacific-origin water exits the Arctic through the Canadian Arctic Archipelago, implying the EGC would receive less PW (smaller values of PW_{equiv}). On the other hand, the regression could also point to a threshold behavior, where during high AO states a significant amount of PW is released, while during low-neutral AO states no clear dependence is shown.

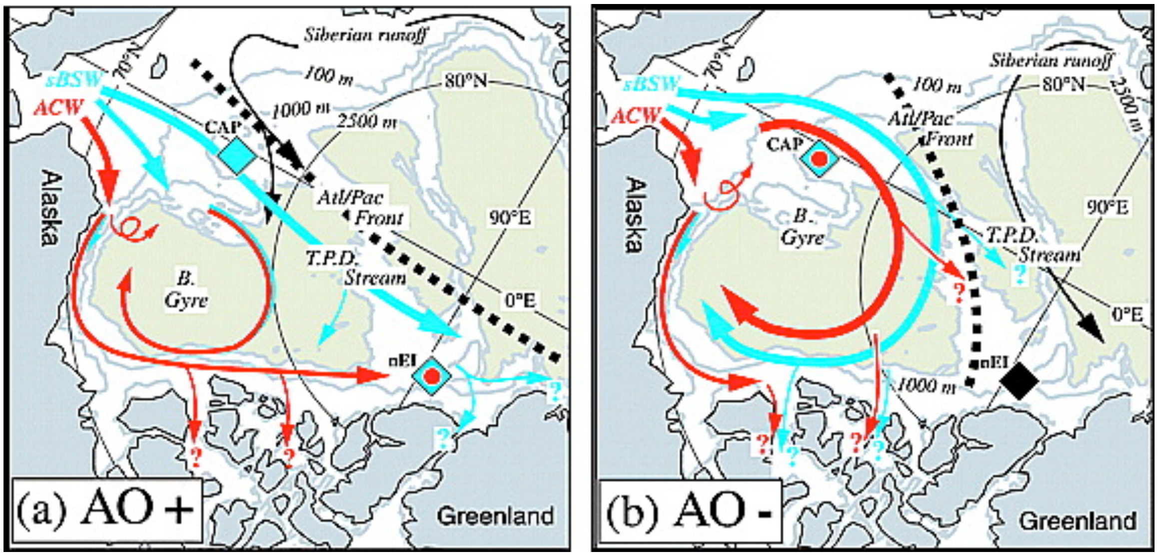

Figure 4.10. Circulation schematic for Pacific Water (broken into ACW: red and sBSW: blue) in the Arctic Ocean during *(a)* positive AO states and *(b)* negative AO states. This figure is taken from *Steele et al.* [2004].

Why is the lag 9 years? Numerous studies have estimated residence times of different water types in the Arctic. *Ekwurzel et al.* [2001] found tracer-derived ages of ~ 8 years for waters just north of Greenland that contained significant Pacific Water fractions. The residence time of waters in the upper 300 m of the Canada Basin, which include the PW layer, was estimated to be ~10.8 ± 3.8 years by *Yamamoto-Kawai et al.* [2007], who based their calculations on a freshwater decomposition similar to that outlined above. These times are generally consistent with the lag computed from Fig. 4.9*a*. However, the different pathways of PW described above likely vary in response to the AO. *Steele et al.* [2004] calculated transit times of sBSW from the Bering Sea to north of Greenland that range from roughly 5 years in the positive AO state, to approximately 10 years in the negative AO state. In reality, the timing for Pacific-origin water to appear in the EGC is complex and likely relies on several factors, including storage in the Beaufort gyre and the state of the western Arctic boundary current. Nonetheless, in an average sense, the lag of 9 years computed here is plausible in light of what is presently known about residence times in the western Arctic. What our results do not shed light on, however, is whether in years of low PW content in the EGC there is a corresponding increase in PW discharge to the CAA. This remains to be investigated.

4.5 Discussion and summary

Using a suite of tracers collected in summer 2004, it has been shown that the waters of the southeast Greenland shelf and slope are partially of Arctic origin. Significant amounts of Pacific Water were found in the EGC and the EGCC from Denmark Strait south to 63ºN. The Pacific Water signal in the EGCC supports the previously expressed notion that this current is an inner-shelf branch of the EGC. By Cape Farewell however, no Pacific Water was observed, suggesting that by this latitude either mixing driven by wind-induced upwelling or cross-frontal exchange with the Atlantic-origin water from the Irminger Sea, had destroyed the Pacific signature. In addition to its link to the EGC, the EGCC is modified by the input of meltwater runoff from Greenland and the melting of sea ice along its path. The use of oxygen isotope data as a tracer, combined with the nitrate-phosphate results, allowed the quantification of these additional sources of freshwater. Fractions of sea ice melt and meteoric water (including meltwater runoff from Greenland, together with precipitation and river runoff from the Arctic) increased southward along the path of the EGCC to maximum values of ~10-12%. The link between these results and the freshwater budget presented in Chapter 3 is explored in the discussion of Chapter 6 below.

The spatial distribution of the Pacific Water, sea ice melt, and meteoric water signals showed a structure closely linked to the velocity and salinity fields of the EGCC. In particular, the high-resolution station spacing during the 2004 cruise showed that each significant PW fraction signal was associated with a jet feature, was enhanced beneath the surface layer, and was eroded in the upper core of the jet. Sea ice melt and meteoric waters showed similar variability on small spatial scales: sea ice melt was surface trapped and influenced strongly by the wind, while meteoric water resided in the surface layer as well and was generally more pronounced towards the coast. Negative sea ice melt fractions observed in waters north of Denmark Strait reflect their Arctic-origins and imply that sea ice was formed from them at some point during the previous winter(s).

By examining historical data taken near Denmark Strait we showed that the PW signal seen in 2004 was in fact much weakened when compared with previous years. The data, extending from 1984-2004, indicated large interannual variations in the amount of Pacific Water present in the EGC/EGCC system, with a pronounced maximum during the late 1990s. It was argued that this trend is linked to the circulation of the Arctic Ocean, where the Pacific Water spreads in pathways controlled to a large degree by the Arctic Oscillation (AO). We found that the PW signals near Denmark Strait are significantly correlated with the AO, with a 9-year time lag. Such a lag agrees qualitatively with previous estimates of residence times in the Arctic, which range from 5-11 years. However, no significant correlation was found between the total freshwater content and the AO, suggesting that local and seasonal processes dominate the salinity field over any propagating signal from the Arctic.

The trend in Pacific Water content found near Denmark Strait and its link to the AO index adds another small piece to our growing understanding of the impact of Arctic Ocean variability on the North Atlantic. To understand more thoroughly the complex relationships between the atmospheric forcing, freshwater sources, interior Arctic circulation, and the resulting export via the EGC/EGCC system will require a diverse set of coordinated observations, as well as fully coupled ocean-atmosphere models. Progress continues to be made along these lines, including contributions from the Arctic-Subarctic Ocean Fluxes (ASOF) program.

Chapter 5

Laboratory experiments on the interaction of a buoyant coastal current with a canyon: application to the EGCC

5.1 Introduction

Although the previous three chapters, and previous literature [*Bacon et al.*, 2002; *Bacon et al.*, 2008], have provided a basic description of the EGCC for the summer months over the southeast Greenland shelf, some central questions still remain as to its origins and how it forms. First thought to be a purely meltwater driven current, evidence from Chapters 2 and 3 suggest that the EGCC has similar water mass characteristics as the EGC, as well as a significant Pacific Water signal (see Chapter 4), both of which imply it is mainly a branch of the polar origin EGC [*Sutherland et al.*, 2007; *Bacon et al.*, 2008]. But how precisely does the EGC split into an inner shelf branch and an along shelfbreak branch? What processes, such as bathymetric steering, wind forcing, or hydrodynamic instabilities control this splitting, and where and when does this happen?

It is the goal of this chapter to examine these questions using a set of idealized laboratory experiments. In particular, we focus on one plausible mechanism, flow separation at a canyon, which might drive the EGC to split along the southeast coast of Greenland. The shelf bathymetry off southeast Greenland is highly variable, narrowing in width dramatically from north to south, and cut by numerous large-scale canyons and basins. One large canyon (width ~50 km), the Kangerdlugssuaq Trough (KG, see Fig. 5.1), crosses the entire shelf with depths up to 600 m, while typical shelf depths are ~250 m in this area.

Historically, the hypothesis that the EGC splits into separate branches was hinted at by a set of joint Icelandic-Norwegian cruises [e.g. *Malmberg*, 1985], which suggested that the KG is a key location for the EGC/EGCC system, and may be the spot where most of the EGCC formation takes place. More recently, the hydrographic observations presented in Chapters 2 and 3 have shown distinct EGCC and EGC jets downstream of the KG, but with θ/S characteristics in both currents similar to those in the EGC north of Denmark Strait. Other supporting evidence, including an XCTD section taken in 2002 across the KG, drifters, and satellite-derived sea ice concentrations, were discussed in Chapters 2 and 3.

But even if the EGC follows the isobaths of the KG and sets up a circulation within the canyon, what controls this process, which observations suggest is highly variable on timescales of days to weeks? How does the EGCC form on the inner shelf as a distinct flow separate from the EGC? What happens at the shelfbreak to the main part of the EGC that continues down the coast?

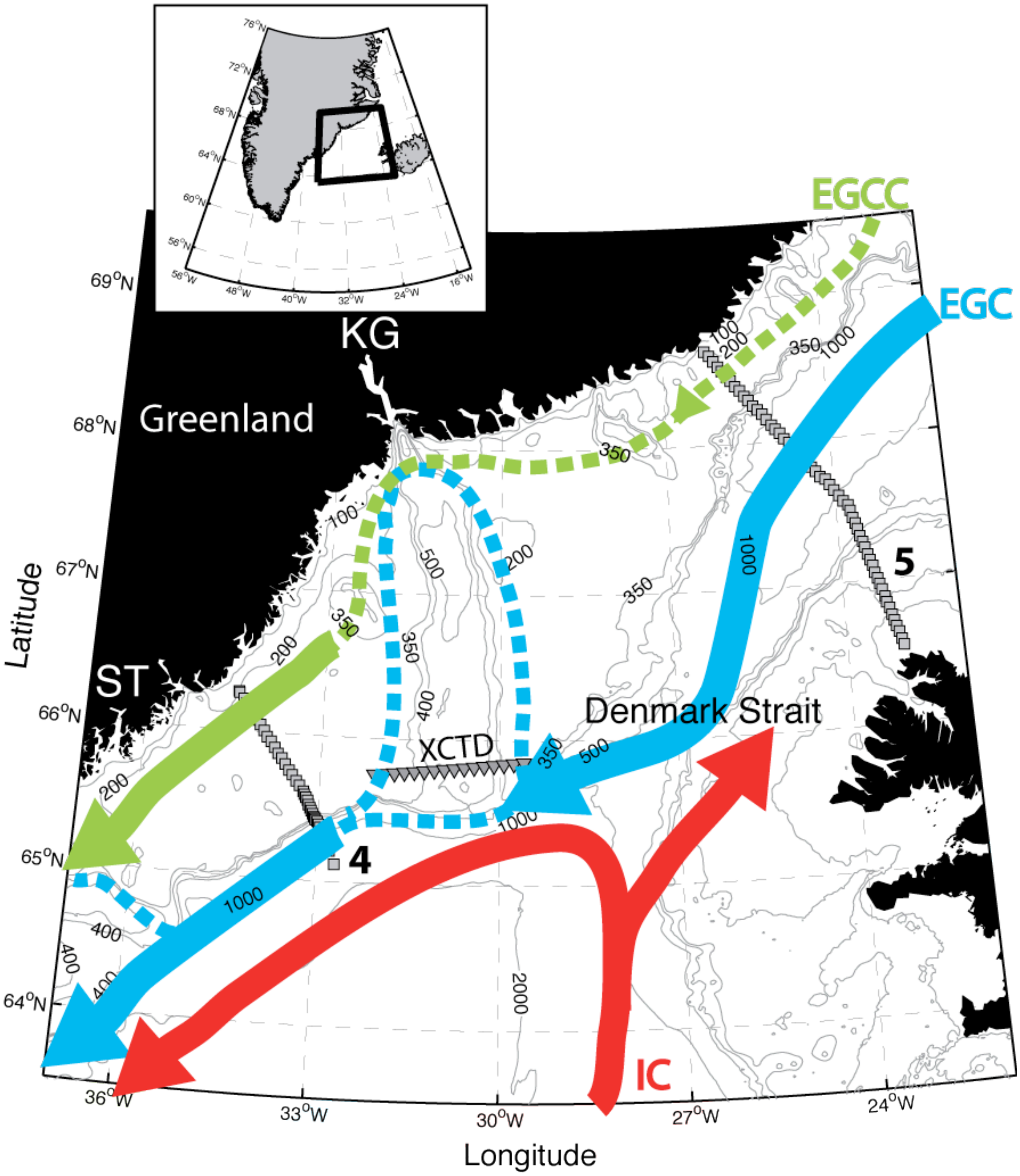

Figure 5.1. Schematic of the major circulation patterns near the Kangerdlugssuaq Trough (KG) region off east Greenland. Dashed lines indicate possible flow paths of the East Greenland Coastal Current (EGCC) and the East Greenland Current (EGC), while solid lines display observed positions of the EGCC, EGC, and the Irminger Current (IC). Selected isobaths from the GEBCO bathymetry dataset [*IOC, IHO, and BODC*, 2003] illustrate the trough region of the KG and the Sermilik Trough (ST). Grey symbols indicate the position of hydrographic stations along sections 4 and 5 taken in 2004, and XCTD labels the 2002 transect.

The central hypothesis of this chapter is that the EGCC stems from a part of the EGC that follows the local bathymetry into the KG, and that this process is time dependent and varies with stratification, wind forcing, and EGC strength. Either through mixing (which would decrease the density difference between the current and the ambient shelf water, thus decreasing the trapping depth of the current: see section 5.3 for discussion of this process) or by following the diverging isobaths at the head of the canyon, part of the EGC appears to become the EGCC, distinct from the recirculation inside of the canyon as well as from the shelfbreak and the offshore flow.

Since observations are scarce on the inner shelf, we rely upon a set of idealized laboratory experiments to model the process of a buoyant flow interacting with a canyon. Note we use the terms buoyant flow, buoyant current, and coastal current interchangeably throughout the chapter. Numerous laboratory and numerical experiments have been done on buoyant currents like the EGC; notably, *Lentz and Helfrich* [2002] described the basic scaling of a coastal current along a sloping bottom in the laboratory, and successfully compared their results to observations (representative of Delaware Bay) and to previous theory [*Chapman and Lentz*, 1994; *Yankovsky and Chapman*, 1997].

The presence of a sloping bottom has a stabilizing effect on coastal currents. Laboratory experiments on coastal currents over a sloping bottom tend to meander and form eddies less than their vertical wall counterparts, and more closely resemble oceanic flows [*Griffiths and Linden*, 1981; *Cenedese and Linden*, 2002]. *Wolfe and Cenedese* [2006] recently explored the stability of a coastal current encountering a bathymetric gap between two sloping bottoms. They found that eddies formed when the gap width exceeded eight times the internal Rossby radius of deformation of the current, but that these disturbances never propagated onto the sloping bathymetry downstream of the gap.

The importance of the width scale of the buoyant flow relative to the scale of the bathymetric feature of interest has been shown previously in laboratory and theoretical studies. Flow separation was found to occur at a bathymetric bend (e.g. a cape) when the radius of curvature was roughly equal to, or less, than the inertial radius of the current, u / f, where u is a velocity scale for the flow and f is the Coriolis parameter [e.g. *Whitehead* *and Miller*, 1979; *Bormans and Garrett*, 1989]. This separation was suggested to be the generation mechanism for gyres observed in the Alboran Sea, with the inflowing Atlantic current separating to form a gyre of width approximately equal to u/f. If no separation occurred, a coastal current trapped to the shore formed and the gyre disappeared. A similar criterion was found to hold for waters near the frontal region that has been observed to cross the Northeast Channel from the Scotian Shelf to Georges Bank, with no separation occurring if the density difference across the front was too small [*Cho, et al.* 2002].

These results are in agreement with the behavior of a reduced gravity, inviscid model of a baroclinic current encountering a cape [*Klinger*, 1994], with separation occurring when $u/f > 0.9*\rho_c$, where ρ_c is the radius of curvature of the cape. These studies provide a context for understanding the EGCC formation process, but none included a sloping bottom, and consequently the role that bottom friction might play in influencing the separation process.

A set of revealing numerical model experiments that included bottom friction showed that for certain strengths of the buoyant inflow, the surface flow separated from a bathymetric bend and moved across the mouth of the canyon, reattaching to the shelf/slope on the downstream side [*Chapman*, 2003]. When the density difference was reduced, and the flow became slower and narrower, the current remained tied to the bathymetry and traveled into and back out of the canyon with no flow across it. However, the model results were sensitive to an imposed background flow: separation always occurred when no background flow was present.

The results and discussion presented here extend those of *Chapman* [2003, hereafter referred to as *DC03*] in a laboratory setting, where no imposed background current is needed to ensure the downstream propagation of the buoyant flow. The findings from the laboratory are then applied to observational data to understand what controls the EGC near the KG canyon region.

5.2 Experimental methods

5.2.1 Laboratory set-up

All experiments were conducted in a clear, round, Plexiglas tank of 1-meter diameter on a rotating, direct-drive turntable with a vertical axis of rotation. Rotation, reported here as $f = 2\Omega$ (s^{-1}) where Ω is the actual rotation rate, was counterclockwise in all runs, and varied between 0.5-2.5 s^{-1}. A total of fourteen experiments were performed with values for the variables of each separate run listed in Table 5.1.

The idealized bathymetry was constructed from hard foam and placed in the tank with one side flush against the wall, as shown in Fig. 5.2. The height of the bathymetry $H = 20$ cm, and the tank was filled to ~18 cm for each experiment. Weights placed on top of the foam kept it in place, while the surface slope of the foam was taped with clear masking tape to eliminate any small irregularities that might disturb the flow. The parameters that describe the shape of the bathymetry, which include the slope, $s = \tan\alpha$, the width of the canyon mouth, W_c, the length of the canyon, L_c, and the radius of curvature, ρ_c, were set to facilitate the easiest comparison to previous studies and the KG region shown in Fig. 5.1. The value of s changes from $s = 0.7$ on the initial slope at line a to $s = 3.3$ along the canyon wall and then back to $s = 0.7$ along line b on the slope at the head of the canyon. $W_c = 25$ cm measured across the canyon at the 1-cm isobath, while $L_c = 31.5$ cm measured perpendicularly from the canyon head to the 0-cm isobath at the canyon mouth.

Buoyant water was pumped from a separate reservoir by an Ismatec pump through a pipe with holes at the end located just below the free surface, as shown in Fig. 5.2. A sponge covered the end of the pipe to minimize any mixing between the buoyant water, which had a density of ρ, and the ambient water of density ρ_a. A Plexiglas wall was inserted next to the source to stop the continual growth of the bulge region, as discussed below, and to force the flow to propagate along the tank wall. Densities, expressed as reduced gravities, $g' = g(\rho_a - \rho)/\rho_a$, were measured before each run and range from 4-23 cm s^{-2}. Pump rates, Q, were varied between each experiment as well and ranged from 4-23 cm^3 s^{-1} (see Table 5.1).

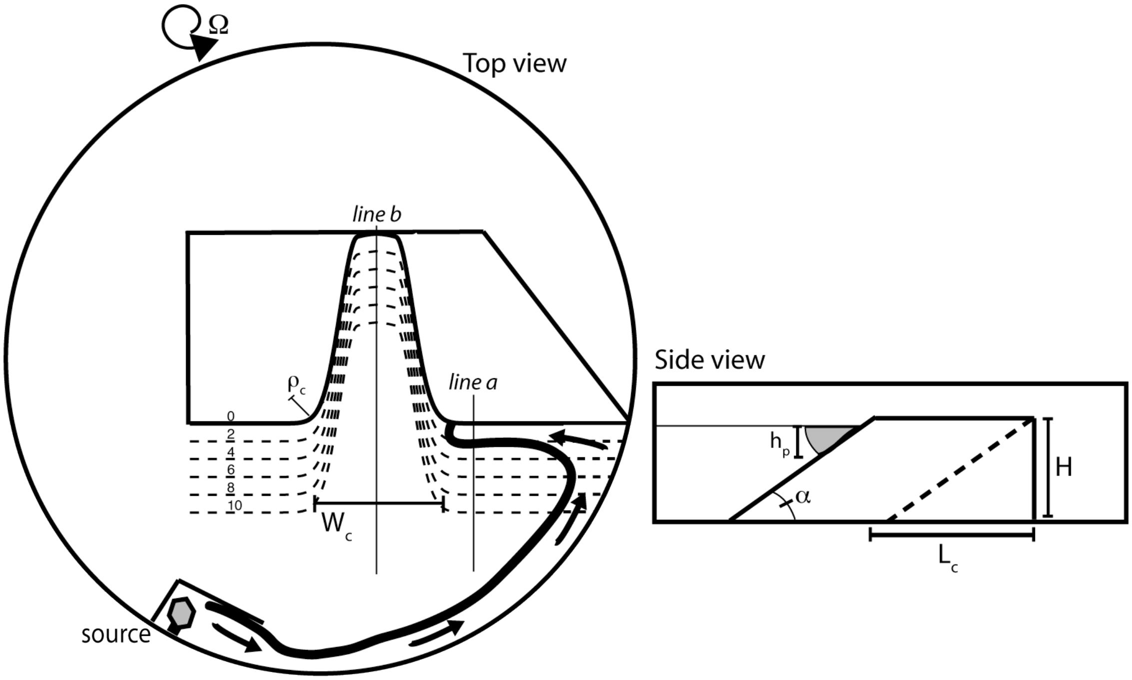

Figure 5.2. *(left)* Top view of the laboratory set-up. The arrows illustrates the path of the buoyant water from the source region, along the tank wall, and onto the sloping bathymetry that is shown by dashed isobaths, every 2 cm. *(right)* Side view of the laboratory set-up. Solid lines show the bathymetry along line *a,* while the dashed line indicates the bathymetry inside the canyon along line *b*. The buoyant current is shaded gray and flows into the page.

An analog video camera mounted on the rotating table recorded each experiment from above. Visual observations were facilitated by dyeing the buoyant water blue (done before the density measurements in each experiment) and seeding the flow with surface particles. These video data were then converted to digital images at 1 frame per second.

Each experiment was run as follows. The tank was filled with ambient water and spun up to solid body rotation. Then the pump was turned on and the dyed, buoyant water initiated the current from the source region. At first, a bulge formed around the source region but was stopped by the Plexiglas enclosure, while buoyant water propagated along the wall towards the model bathymetry. Particles were placed on the surface of the flow by hand continually throughout the experiment. The flow was allowed to evolve until the current propagated past the bathymetry and around the entire rest of the tank, where it then started to interfere with the source region (see Fig. 5.2). At this point the experiment 'ended'. The experiments usually lasted for 6-7 minutes and in all cases this was enough time to allow a quasi-steady state to be reached. We discuss the transition and steady phases of each experiment further in the results section below.

Table 5.1. Variables used in the laboratory experiments. The first three, f, g', and Q, are set *a priori* and are the Coriolis parameter, reduced gravity, and buoyant water flow rate, respectively. The scales h_p and W_d are calculated from these variables.

Run	f (s^{-1})	g' ($cm\ s^{-2}$)	Q ($cm^3\ s^{-1}$)	h_p (cm)	W_d (cm)	Case[a]
1	2.5	10	10	2.2	1.9	A
2	0.5	10	10	1.0	6.3	C
3	2.5	20	10	1.6	2.2	A
4	0.5	20	10	0.7	7.5	C
5	1.0	10	10	1.4	3.7	B
6	2.0	10	10	2.0	2.2	A
7	1.75	10	10	1.9	2.5	A
8	1.25	10	10	1.6	3.2	B
9	1.75	20	10	1.3	2.9	A
10	2.5	23	23	2.2	2.9	B
11	2.5	4	4	2.2	1.2	A
12	1.75	14	20	2.2	3.2	B
13	1.89	10	13.25	2.2	2.5	B
14	1.17	6.43	13.46	2.2	3.2	B

[a]: Case refers to the three regimes of steady state flow behavior observed in the laboratory and are described in detail in section 5.4 in the text and Fig. 5.7.

5.2.2 Observing the laboratory flow

A two-step method was developed to characterize the flow field objectively. The first step was to define when the flow reached a steady state, after an initial transition phase.

After defining a steady state period, we quantified the flow by looking at the position of the front along a line perpendicular to the head of the canyon (line *b,* Fig. 5.2). To determine whether or not the flow reached a steady state, we looked at the rate of increase of the current width along the lines *a* and *b* in Fig. 5.2.

First, though, a method had to be developed to measure the surface flow field and find the position of the front during each run. Fig. 5.3 illustrates the two methods used to determine the position of the front. In Fig. 5.3*a*, a processed video frame shows the tracks of particles from run 7 during an arbitrary time period, t = 67-200 sec. The original image was imported into MATLAB, converted into a black and white intensity image, and edited to isolate the region of interest. Using a particle tracking software package in MATLAB, we next identified the location of the particles at a certain time, (white particles in Fig. 5.3) and then used successive images to follow the particle trajectories throughout a certain time range. Since the particles traced the velocity signal, they also were indicators of the front location at the surface. The majority of particles were clustered near the maximum velocity of the current. Note that the maximum velocity does not correspond to the offshore edge of the buoyant current, but is centered over the sloping interface between the buoyant water and the ambient water, as shown in Fig. 5.4*a*. The offshore distance from the coast to the center of the particle tracks was calculated for 20-second time ranges for each run, along both lines *a* and *b*. This distance is called W_{obs} for line *b* (see Fig. 5.4*a*).

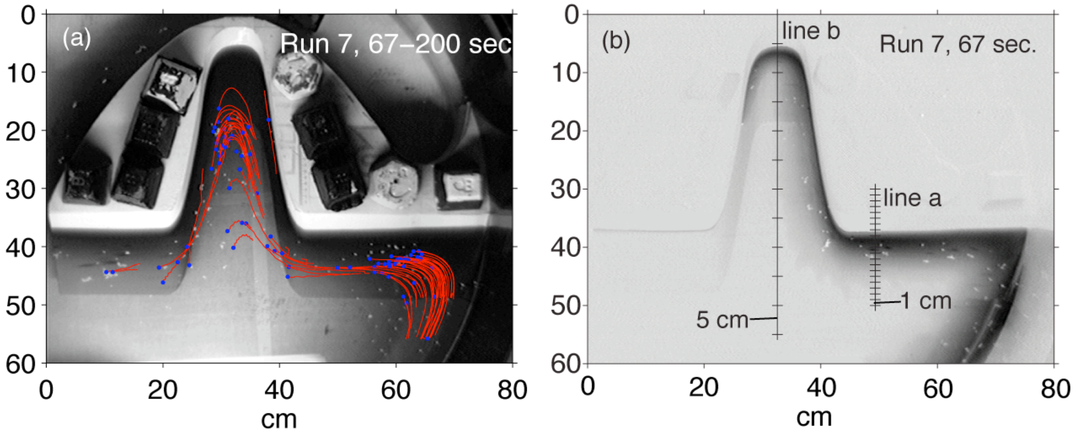

Figure 5.3. *(a)* Top view of run 7 from a video frame at an arbitrary time period, which illustrates the particle tracking method. Blue dots show the end position of each particle track. *(b)* Grayscale image of run 7, obtained at the starting time of *a*, showing the buoyant current location using the dye as a proxy. The two dashed lines are lines *a* and *b* in Fig. 5.2.

The second method to calculate the frontal position was to use the dye in the current. Similar to the clustering of the particles in the velocity maximum of the current, the dye can be used as a proxy for the position of the foot of the front, shown in Fig. 5.4*b*, where the front intersects the bottom at h_p. Fig. 5.3*b* illustrates the second method, showing how, over the foot of the front, the dye appears more intense in color since the depth of the current is at its deepest there. Thus, to compare to the particle-derived frontal positions, we calculated the position of the current from the dye intensity images along both lines in 20-second bins. However, at later times when the current was separated from the canyon slope, the dye method broke down occasionally due to corruption of the intensity images by reflections off the bottom of the tank. Thus the dye method was used only to find the starting time when the current first passed line *b*, as well as for comparison to the particle-tracking method. Visual observations of the depth of the current were also facilitated by the dyed water. Throughout the rest of the chapter, though, we use W_{obs} as calculated from the particle-tracking method.

The particle-tracking method was also used to calculate the surface flow current velocities. Velocities were calculated on the slope upstream of the canyon (outlined region in Fig. 5.4*a*), before the influence of the bathymetric bend was felt, but after the current had equilibrated on the sloping bottom. Velocities at other depths were not measured.

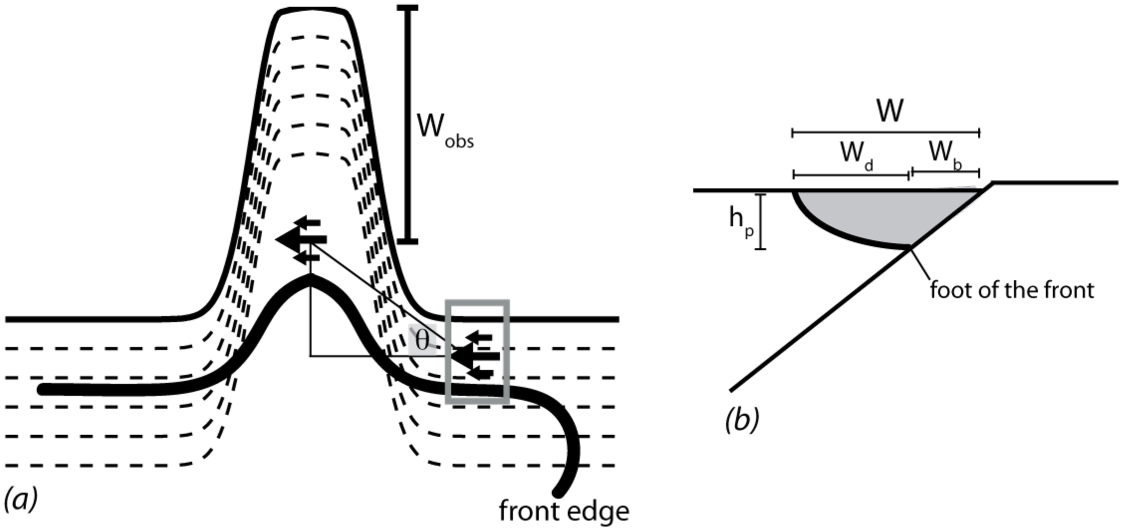

Figure 5.4. *(a)* Schematic showing the variables used to quantify the buoyant current behavior. The edge of the front (heavy line) marks the offshore extent of the current. W_{obs} is the distance from the head of the canyon to the velocity signal marked by the particles, while θ is defined as the front angle. The gray box outlines the region where u_{obs} was calculated. *(b)* Schematic of vertical section through current showing the depth and width scales defined in the text. Flow is into the page.

5.3 Buoyant current scaling and theory

5.3.1 Review of scaling for a buoyant current on a slope

The dynamics of a buoyant current flowing over a slope far from the source region are relatively well understood. *Lentz and Helfrich* [2002] provide the most recent scaling and review of previous work in the laboratory, while *Chapman and Lentz* [1994] originally detailed the basic theoretical framework. A brief introduction to these dynamics was given in Chapter 2 (Section 2.4), where we focused on the winds' influence on the structure of a buoyant current.

The buoyant current is in geostrophic balance in the cross shelf direction, associated with a density front that separates the lighter water onshore from the denser water offshore. Given sufficient time and distance, the front is advected across the shelf by the bottom Ekman layer velocity that is directed offshore. The front is eventually trapped at a location where the thermal wind shear causes a reversal in the bottom boundary layer velocity, stopping the advection of the front across the shelf. This trapping depth, h_p, is given by

$$h_p = \sqrt{\frac{2Qf}{g'}}, \tag{5.1}$$

and was tested successfully in models for many different values of the parameters [*Chapman and Lentz*, 1994; *Yankovsky and Chapman*, 1997]. Once the vertical scale of the buoyant current is set by h_p, two horizontal scales follow. The first one, W_b, is the distance from the coast to the trapping depth and equals

$$W_b = h_p / s, \tag{5.2}$$

where s is the bathymetric slope. The second one, W_d, is the internal Rossby radius of deformation and is the natural scale for the width of the density front, given by

$$W_d = \sqrt{g' h_p} / f, \tag{5.3}$$

where the trapping depth is used as the vertical scale. The total width of the flow is $W = W_b + W_d$ and compares well to widths observed in the laboratory. This scale can also be written in terms of two wave speeds, $c_w = (g'h_p)^{1/2}$, the internal gravity wave speed, and $c_\alpha = sg'/f$, the phase speed of a long topographic wave, as $W = (c_w / f)(1 + c_w / c_\alpha)$ [*Lentz and Helfrich*, 2002]. These scales are illustrated in Fig. 5.4*b*.

One other useful consideration is to quantify to what degree the buoyant current is tied to the bottom: in the "slope-controlled" limit bottom friction is more important, while the current is less coupled to the bottom in the "surface-trapped" limit. *Lentz and Helfrich* [2002] quantify this using the ratio c_w / c_α, which is equivalent to the ratio of W_b / W_d, as well as the ratio of the isopycnals slope, h_p / W_d, to the bottom slope, s [*Cenedese and*

Whitehead, 2000]. For $c_w / c_\alpha << 1$, the current is surface-trapped and its width is W_d, while for $c_w / c_\alpha >> 1$, the flow is slope-controlled and the total width, W, is more appropriate. Recall in Chapter 2 we used the ratio of the area of the current offshore of h_p, A_s, to the area onshore of h_p, A_b, to characterize the degree to which the flow was surface-trapped.

The velocity of the flow also depends on the degree to which it is slope-controlled. Over a sloping bottom, the velocity scale for a buoyant current is

$$c_p \approx c_w \left(1 + c_w / c_\alpha\right)^{-1}. \tag{5.4}$$

This velocity scale is called the propagation speed, and is always less than c_w, though it approaches that limit in the case surface-trapped flow [*Lentz and Helfrich*, 2002]. In slope-controlled currents, the speed approaches c_α.

Observations from oceanic flows support this dynamical framework. For example, the depth and width scales of the Chesapeake Bay coastal current were shown to agree well with these theoretical values even in strongly forced regions, where both downwelling and upwelling favorable winds were common [*Lentz and Largier*, 2006]. More relevant to this study are observations obtained during the summer 2004, which showed that the structure of the EGCC responds much like these smaller scale river plumes to strong wind events, and also compares well with the theoretical scales despite the many assumptions (e.g. steady state, far from source region, no alongshore variations) of the theory [see Chapters 2 and 3; *Sutherland and Pickart*, 2007].

5.3.2 Review of buoyant current separation scaling

Given the basic scales and parameters relevant to buoyant currents on a sloping bathymetry presented above, we turn next to the problem of how flow separates from a bathymetric bend, such as at a canyon or a cape. This problem has been addressed analytically, numerically, and experimentally, with several important scales found that are useful for comparison between the different studies.

These scales include the radius of curvature of the bathymetric bend, ρ_c, which in the present experiments is ~6 cm at the surface, and the inertial radius of the current, u / f.

Several studies have found that flow separation occurs at the upstream edge of a bathymetric feature (e.g. cape, canyon) when ρ_c is less than or equal to u / f [*Bormans and Garrett*, 1989; *Klinger*, 1994; *Cho, et al.*, 2002]. In the laboratory, as mentioned above, the flow speed of a current can be scaled by c_p, so that u / f is equivalent to W_d (as defined in Eqn. 5.3) for surface-trapped flows [*Lentz and Helfrich*, 2002]. This is the same as stating that the flow has a Froude number ($F = u / (g' h_p)^{1/2}$) equal to 1.

Another important scale is the width of the bathymetric feature, which was found to influence the stability of a buoyant current as it encountered a bathymetric gap in the laboratory [*Wolfe and Cenedese*, 2006]. Other experiments looking at a buoyant current encountering a step change in bathymetry have shown that the incident flow can actually split at the depth change, with part of the flow continuing on to the shallower bathymetry, while the rest of the flow turns to stay at a constant depth [*Cenedese et al.*, 2005]. However, those experiments focused on geometries (i.e. a vertical gap and a step) slightly different than the one used in the present study.

The width scale of the current relative to the width of the canyon can be defined as a Burger number, $Bu = W / W_c$, a parameter shown to be important in controlling barotropic circulations near a canyon in models [e.g. *Klinck*, 1996; *She and Klinck*, 2000]. Furthermore, numerical experiments on barotropic current interaction with cross-shelf topography [*Williams, et al.,* 2001] showed that the flow behavior was determined by the strength of the bathymetry (such as a canyon), which depended on the depth scale of the canyon to the ambient shelf depth, and the width scale of the sloping bathymetry. For larger features, they found that the flow followed isobaths, while for smaller depth changes the flow tended to cross the channel bathymetry. Applying their results to the Scotian Shelf crossovers, they concluded that the baroclinicity of the flow was essential for separation to occur and the strength of the bathymetry there prevented purely barotropic flows from separating. In a related study, *Sheremet and Kuehl* [2007] found a hysteresis in the behavior of a barotropic current encountering a gap, where it either separated or not depending upon the previous conditions of the flow field.

The numerical experiments of *DC03*, introduced above, are a primary motivation for the present work, as well as the closest analogue to the buoyant current system off Greenland. *DC03*'s motivation was to explain the loss of transport in the boundary current system from the Labrador shelf to the Middle Atlantic Bight. *DC03* hypothesized that these transport losses occurred at a few specific locations along the buoyant current's path, particularly at bathymetric features such as canyons and capes that would allow offshore leakage. The main conclusion of *DC03* was that the separation process depended critically on the strength of the buoyant flow compared to the ambient offshore current.

5.4 Results

In all fourteen experiments, the buoyant current propagated along the wall from the source region until it encountered the slope area (see Fig. 5.2). Upon reaching the sloping bathymetry, the current slowed and widened, in accordance with previous laboratory experiments of buoyant currents over sloping bottoms. Traversing the length of the slope upstream of the canyon, the flow equilibrated, and the foot of the front approached the trapping depth, h_p, before the flow encountered the canyon.

Along line *a*, we found that the current width scaled with the total predicted width, W, although we also observed a slow widening of the current throughout each run. In previous laboratory experiments, observations of the width of the buoyant current showed that it grew in time like $t^{1/2}$, due to interfacial drag with the ambient water on the offshore side of the plume [*Lentz and Helfrich*, 2002]. Growth of a boundary layer on the inshore side of the current due to viscous drag by the wall should scale like $(\nu t)^{1/2}$, where ν is the molecular viscosity of water, also a $t^{1/2}$ growth. This viscous layer would only explain 1 cm growth per 100 seconds, which is much less than what is observed in the laboratory.

However, at line *b* the flow exhibited a different behavior, shown in Fig. 5.5. During the early stages of each run, the width of the current inside the canyon, W_{obs}, increased rapidly for some time (Fig. 5.5*a*), then slowed to widen at the same rate ($t^{1/2}$) as the current width on the upstream slope (line *a*). This result suggests that the flow goes through a transition phase, with a rapid widening of the current inside the canyon, until it reaches a quasi-steady state.

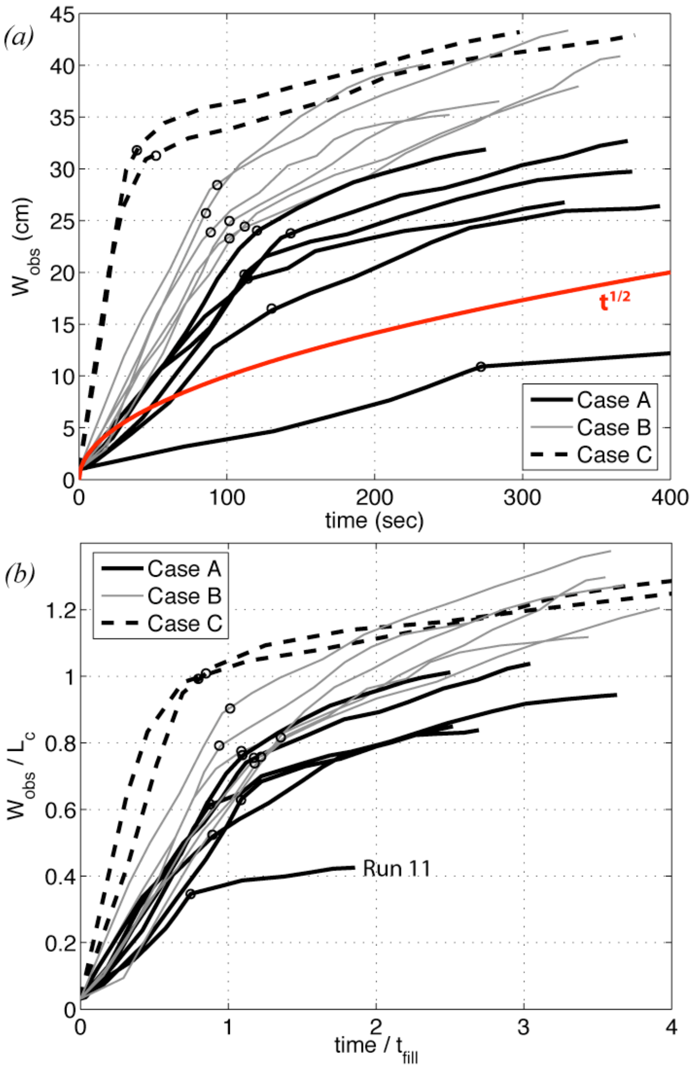

Figure 5.5. *(a)* Current width, W_{obs}, as a function of time. The three cases, *A*-*C*, are differentiated by line type. Open circles mark the beginning of the quasi-steady state for each run. *(b)* Same as in *a*, except the current width is normalized by the length of the canyon, L_c, and time is normalized by the filling time, t_{fill}. A value of W_{obs} / L_c = 1 indicates the front has moved offshore all the way to the canyon mouth.

Fig. 5.5*b* shows the same variables but in a non-dimensional form. W_{obs} is scaled by L_c, the length of the canyon, so that $W_{obs} / L_c \sim 1$ indicates that the front had moved offshore all the way to the canyon mouth. Time is scaled by $t_{fill} = A_p * h_p / kQ$, where A_p is the horizontal area within the canyon out to the position where the canyon width equals $2W$. kQ represents the percentage of inflow that does not exit the canyon region defined by A_p. The value of k was found by assuming $t / t_{fill} = 1$ at the start of the quasi-steady state of each run (open circles in Fig. 5.5*a*), the best fit for k from all the runs was $k \approx 0.23$.

The normalization timescale, t_{fill}, represents the amount of time it would take the buoyant current to fill up the inside of the canyon out to where the canyon width equals twice the current width, if the canyon was filled completely to a depth h_p. Note that in Fig. 5.5*b* not all the steady phases started exactly at $t / t_{fill} = 1$ implying that the transition period is slightly different for each run, but given the approximation in the scales used, the scatter about unity is small. The differences between the transition behaviors of the three cases identified in Fig. 5.5 will be detailed further below, after describing their parameter dependencies.

The observed velocity of the current, u_{obs}, is shown in Fig. 5.6 at two times during each run versus the theoretical scales introduced above. Fig. 5.6*a* plots u_{obs} versus c_w and shows that the velocity of the current, even at an initial time, was much less than c_w, on average $u_{obs} / c_w \sim 0.3\text{-}0.4$. At a later time, the flow slowed down even more, as shown in Fig. 5.6*a*. However, this is in line with previous experiments, and what is expected of a current that is continually widening over a sloping bottom [*Lentz and Helfrich*, 2002]. Fig. 5.6*b* plots u_{obs} versus the propagation speed for a current over a sloping bottom, c_p. Since c_p takes the slope into account, it does a better job of predicting the observed initial velocities with $u_{obs} / c_p \sim 0.8\text{-}1.0$ on average. Again, though, as the experiment progresses, the flow slows down considerably with $u_{obs} / c_p \sim 0.5\text{-}0.6$ for measurements in quasi-steady state.

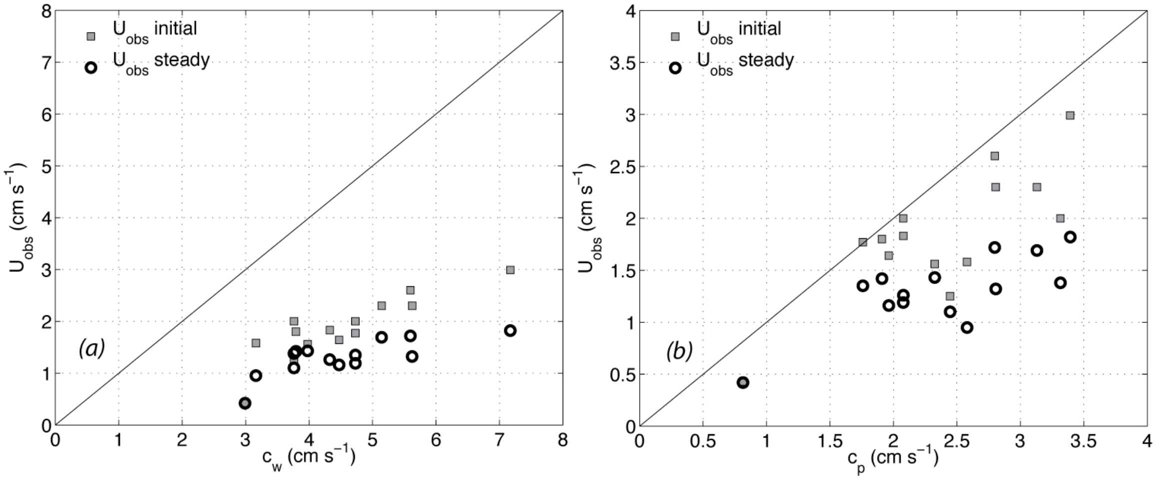

Figure 5.6. *(a)* Observed speed of the current on the upstream slope at an initial time (gray squares) and at the start of the steady phase of each run (open circles), versus the theoretical speed, c_w. The line shows a 1:1 correspondence. *(b)* Same as in *a* but versus the propagation speed of the current, c_p. The line shows a 1:1 correspondence.

5.4.1 Overview of the steady circulation: 3 cases

By examining the quasi-steady phases of all the runs, we found that we could replicate the flow separation positions found numerically by *DC03*. Depending on how far the buoyant current penetrated into the canyon, a distinct accompanying circulation was set up in the head of the canyon, between the main part of the current and the canyon wall. These circulations are most likely related to the processes noted by previous studies on coastal current separation past a bathymetric feature, such as the gyre formation in the Alboran Sea [*Bormans and Garrett*, 1989], or past Tsugaru Strait east of Japan [*Kawasaki and Sugimoto*, 1984].

Fig. 5.7 illustrates schematically the three cases observed, showing the general direction of flow and the frontal position (red lines) overlaid on actual particle trajectories from selected runs. The three circulations differ in the amount of buoyant current penetrating into the canyon, as well as in the circulation present near the canyon head.

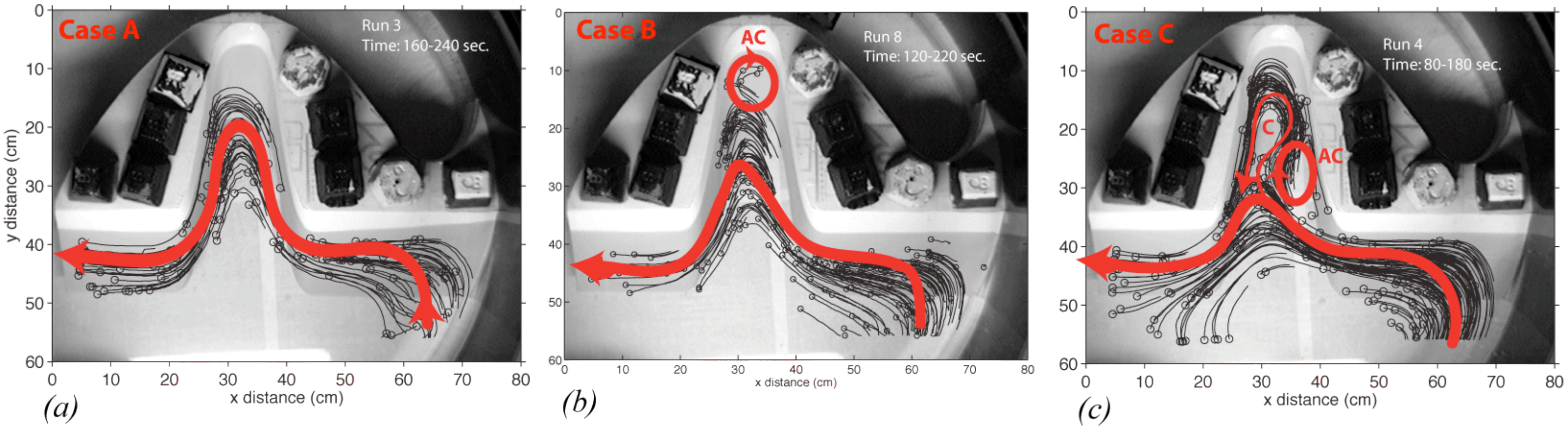

Figure 5.7. Schematic of the three flow patterns observed (red lines). These are overlaid on actual particle tracks from selected runs of each case. The three types are *(a)* Case A, where the greatest penetration into the canyon was observed along with no recirculation; *(b)* Case B, with an intermediate penetration into the canyon and one anticyclonic (AC) eddy formed; and *(c)* Case C, with the current separating across the canyon mouth, with one anticyclonic (AC) eddy formed just past the separation point, and a cyclonic recirculation (C) in the canyon head.

Case A is the “no eddy” case shown in Fig. 5.7*a*, where the flow was observed to follow the bathymetry the farthest into the canyon, with no subsequent creation of a separate circulation in the head of the canyon. Six experiments fell into this category (Table 5.1), and though the exact position of the front along line *b* varied, no particles were observed to cross the canyon mouth in any of these runs.

In Case B, the “one eddy” case shown in Fig. 5.7*b*, the flow did not penetrate as far into the canyon as in Case A. In these experiments, the final position of the front was observed to vary from midway in the canyon to near the canyon mouth. Six runs fell into this category (Table 5.1). Besides the separation of the buoyant current from the canyon slope, these runs also exhibited a closed anticyclonic circulation at the head of the canyon. This eddy feature formed during the transition phase, as part of the current separating from the canyon slope turned to the right to form an anticyclone. Once the steady phase was reached, however, the anticyclone was isolated from the main part of the current. The separating part of the current flowed across the canyon and reconnected to the slope on the other side of it, continuing on to exit the canyon.

Case C, displayed in Fig. 5.7*c*, was characterized by almost total separation of the current from the slope as soon as it encountered the canyon. In the two runs that showed this behavior (Table 5.1), there were two identifiable circulations set up in the head of the canyon during the transition phase. Similar to Case B, an anticyclone formed just downstream of the separation. However, as will be discussed in the next section, the deformation scale of the front limited the size of the anticyclone that was trapped to the upstream canyon wall. Flow that circuited around this anticyclonic eddy then split, either flowing back towards the mouth as a countercurrent, or continuing on cyclonically around the canyon head. This cyclonic flow was then observed to exit the canyon at the downstream bend in the canyon bathymetry and re-join the separated part of the current that passed directly across the mouth. The flow across the mouth was the dominant pathway observed in these runs at quasi-steady state, although the current had a slight curvature into the canyon, as shown in Fig. 5.7*c*.

5.4.2 What controls the separation process?

As noted earlier, the behavior and scales of the buoyant current along the initial slope, line *a* in Fig. 5.2, were in good agreement with the extensive study of *Lentz and Helfrich* [2002]. The focus of this section is on examining the dependence of the flow separation process on these scales, which are set along the initial slope upstream of the canyon.

Tables 5.1 and 5.2 list the relevant scales for each flow behavior observed. Also listed in Table 5.2 is c_w / c_α that varies from 0.1-2.7, which is much lower than the *DC03* range of 3-18, but does span the two limits of c_w / c_α corresponding to the surface-trapped ($c_w / c_\alpha < 1$) and slope-controlled ($c_w / c_\alpha > 1$) cases.

Table 5.2. List of the relevant parameters that were observed to control the flow behavior in the laboratory. These are compared with the previous study of *Chapman* [2003], and with values derived from observations of the EGC/EGCC system.

Case	***Bu*** ***(W / W_c)***	***W / ρ_c***	***c_w / c_a***	***flow across canyon***[a]
Case A	0.18 – 0.21	0.72 – 0.85	0.6 – 2.7	*no*: none to slight
Case B	0.21 – 0.26	0.9 – 1.1	0.5 – 1.3	*yes*: mid-way up canyon
Case C	0.31 – 0.34	1.3 – 1.4	0.1 – 0.2	*yes*: at mouth
DC03[b]	0.4 – 0.5	0.93 – 1.05	3 – 18	*yes*: whole range observed
Ocean[c]	0.3 – 0.7	0.5 – 1.2	1.8 – 13	*yes*: whole range suggested

[a]**:** For laboratory and *DC03* this is for flow during the quasi-steady phase of each run.
[b]**:** Ranges taken from *Chapman* [2003] model results.
[c]**:** Ranges taken from available observations of the EGC north of the KG region.

The first clue to understanding the different cases introduced above comes from re-examining Fig. 5.5, which shows the growth of the current width in time. The runs with the largest penetration into the canyon took the longest time to reach quasi-steady state, i.e. the front moved offshore the slowest during the transition phase of Case A flows. By contrast, the two Case C runs progressed relatively rapidly through the transition period. One experiment, run 11, behaved anomalously compared with the other runs. Run 11 had the smallest reduced gravity and flow rate (Table 5.1) that resulted in a relatively slow and narrow current; this might account for the observation in Fig. 5.5 that it seemed to grow like $t^{1/2}$ at all times, with no fast growth inside the canyon.

The steady state position of the front for each run is quantified in Fig. 5.8*a*, which shows the observed current width in the canyon scaled by the length of the canyon, W_{obs} / L_c, as a function of the predicted current width, W, divided by the radius of curvature, W / ρ_c (where $\rho_c \sim 6$ cm). Run 11, as noted above, displayed the least separation as it had a value of $W_{obs} / L_c \sim 0.33$. There is a clear dependence of the degree of separation, taken as W_{obs} / L_c, on the ratio W / ρ_c. The critical W / ρ_c value, above which the flow moves across the canyon mouth, suggested by Fig. 5.8*a* is equivalent to the value of ~1 found previously using estimates of $u / f\rho_c$ [*Bormans and Garrett*, 1989; *Klinger*, 1994]. We chose not to use u_{obs} to estimate $u / f\rho_c$ because, as shown in Fig. 5.6, the speed of the current diminished continuously during each run due to the widening of the current.

The width used here, W, is greater than u / f, since if u is scaled by c_w it is equal to the deformation radius, W_d, and only part of the total current width. If u is scaled by c_p, the two widths are still not equal in general, by examination of 5.4 and the definition of W. The separation point of the current from the canyon slope was farthest towards the mouth in the two runs of Case C, which had widths slightly larger than ρ_c. In these runs, the main part of the buoyant current was observed to flow almost straight across the canyon mouth.

Another way to look at the degree of separation is shown in Fig. 5.8*b*, which plots the angle of the current, θ, versus W / ρ_c, where the angle of the front is calculated from the position of the front edge at line *a* to that of the front edge at line *b*. This angle is illustrated in Fig. 5.4. Larger angles indicate more penetration into the canyon, while an angle of zero corresponds to flow straight across the mouth. This figure emphasizes that even though the majority of the flow in the two Case C runs did not enter the canyon, part of the flow did curve inwards (see Figure 5.6*c*), indicating some bathymetric influence.

For comparison, three runs of *DC03* that spanned a similar range of flow separation behavior as we observed are plotted on Fig. 5.8. The general trend is the same: as the width of the current increased relative to the radius of curvature, the location where the current separated from the canyon slope moved closer to the canyon mouth. The critical value of W / ρ_c from the present laboratory results and the model results are similar.

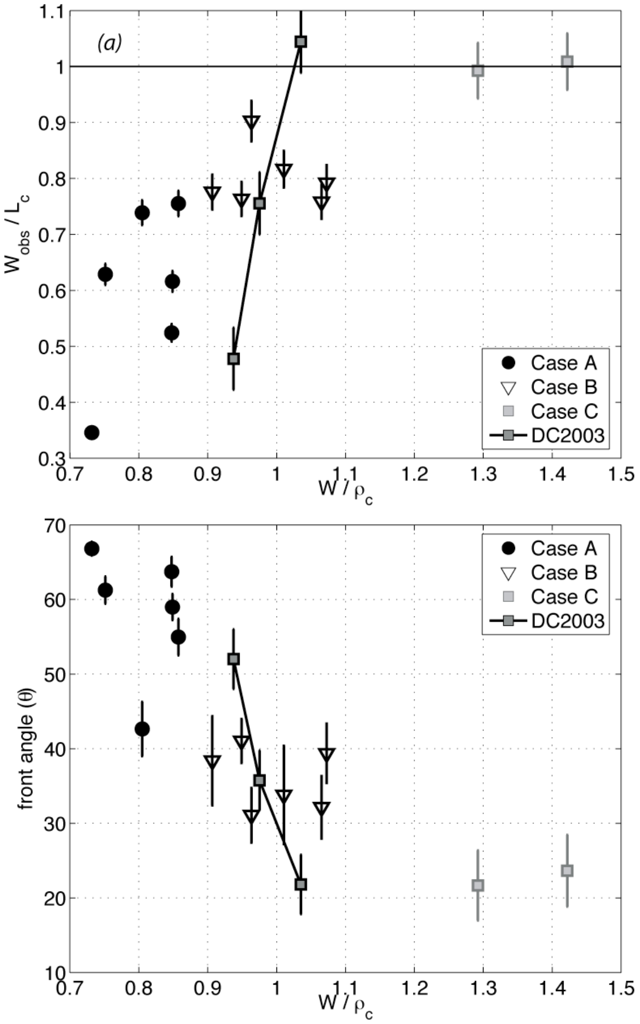

Figure 5.8. *(a)* W_{obs} / L_c versus the ratio of the predicted width of the current, W, and the radius of curvature, ρ_c for all runs. Grey squares are taken from *Chapman* [2003]. A value of $W_{obs} / L_c = 1$ indicates separation of the current from the canyon slope at the canyon mouth. *(b)* Same as in *a*, but for the angle of the current, θ, as it enters the canyon. Smaller angles indicate more flow straight across the canyon mouth.

The condition for separation derived by *DC03* was that the bottom velocity in the along-front direction goes to zero. Hence, indirect comparisons between the studies are necessary since calculating the velocity at the bottom of the current would have been challenging. However, it is important to note that in the *DC03* model, flow separation occurred for all inflow parameters (e.g. all g' and Q) if the background current was absent. In the laboratory, no background current was present, but separation did not always occur. Thus the separation process we observed in these experiments differed somehow from those in *DC03*. Finally, we looked at the dependence of the current width in the canyon on the ratio c_w / c_α, shown in Fig. 5.9. There seems to be a clear dependence of the flow behavior on c_w / c_α at the extreme range of the c_w / c_α values tested. The surface-trapped currents separated from the canyon slope closer to the canyon mouth, while the slope-controlled currents tended to follow the bathymetry far into the canyon. However, for intermediate values of c_w / c_α's, close to 1, the flow exhibited a wide range of behaviors. Since the ratios, W / ρ_c and c_w / c_α, can be calculated *a priori*, it is theoretically possible to fill in the missing parameter space of Fig. 5.9. Due to the limitation of using only one geometry (i.e., fixed W_c, ρ_c, and s) in the laboratory, it was impossible to set up runs with $c_w / c_\alpha >> 1$ and $W / \rho_c > 1$, or the opposite, having surface-trapped currents ($c_w / c_\alpha << 1$) that had $W / \rho_c < 1$. For the range of c_w / c_α that could also be varied in W / ρ_c, the parameter W / ρ_c controlled the degree of separation and not c_w / c_α, since as shown in Fig. 5.9, for the same value of c_w / c_α different levels of separation (i.e. $0.6 < W_{obs} / L_c < 1.0$) were observed.

Also plotted in Fig. 5.9 are the same three runs from *DC03* plotted in Fig. 5.8. These show that, at least in the numerical model, slope-controlled currents can either separate from the canyon slope near the canyon mouth ($W_{obs} / L_c \sim 1.0$) or penetrate into the canyon ($W_{obs} / L_c < 1.0$). This suggests that c_w / c_α is not a relevant parameter for the separation process for these numerical runs, as also indicated by the laboratory experiments discussed above.

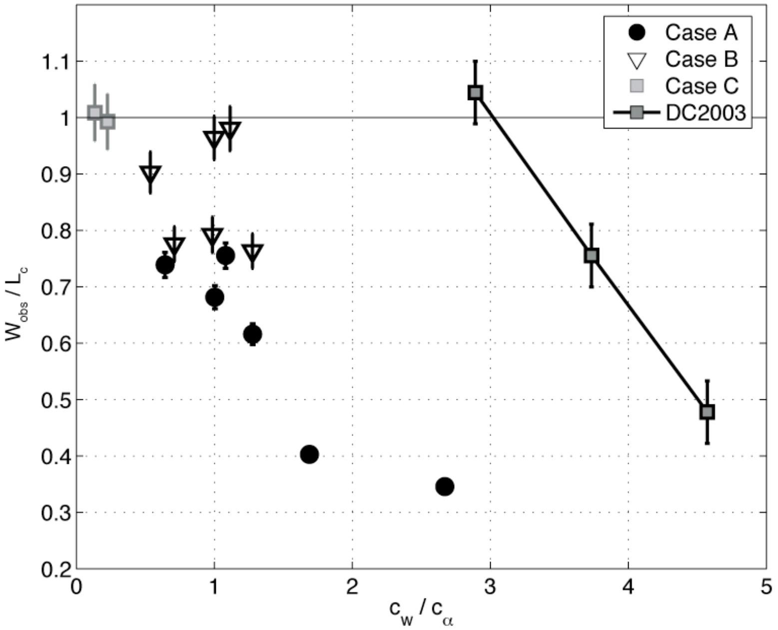

Figure 5.9. This plot shows the dependence of the location of the current separation from the canyon slope on the degree to which bottom friction is important, indicated by $c_w \ / c_\alpha$. A value of $c_w \ / c_\alpha >> 1$ corresponds to slope-controlled currents, while for $c_w \ / c_\alpha << 1$, the flow is surface-trapped. Grey squares are taken from *Chapman* [2003].

5.5 Discussion

The three cases of quasi-steady state flow described above span the range of flow behavior observed in the laboratory, and have some similarities to previous modeling and theoretical work. Case A was the simplest case (Fig. 5.7*a*), with the buoyant current entering and exiting the canyon without any portion of it moving across the mouth. All six runs of Case A had $W / \rho_c < 1$; this holds true even if the radius of curvature is increased to reflect the position of the foot of the current at depth.

Since no circulation was observed in the head of the canyon in the Case A runs, yet the position of the front inside the canyon varied slightly between runs (Fig. 5.8*a*), what sets the steady state position of the front? One potential explanation is the constraint of the canyon bathymetry on the current width itself. In other words, the width of the current going into the canyon plus the width of the current exiting the canyon, exerts control over where the main front is positioned at line *b*. The steady state position of the front inside the canyon should then scale with the position in the canyon corresponding to twice the width of the current, $2*W$.

Flow separation was observed to occur in the Case B runs along the canyon slope region (Fig. 5.7*b*), along with the formation of an anticyclonic eddy in the head of the canyon. These runs spanned the critical W / ρ_c value, illustrated in Fig. 5.8, though the location of current separation was almost constant ($W_{obs} / L_c \sim 0.8 - 0.9$). The eddy formed as the separated current split upon hitting the downstream side of the canyon, creating two oppositely directed flows (Whitehead, 1985). Note that it is not a strong recirculation and could have been ignored (i.e. not shown in figures) in the calculations of *DC03* that showed flow separation.

The runs of Case C were similar to Case B, but with complete separation of the current at the mouth of the canyon, confirming the validity of the $W > \rho_c$ criterion. These runs also exhibited a closed anticyclonic circulation, but the feature was constrained to hug the upstream canyon wall, which allowed a cyclonic circulation to flow through the head of the canyon and back out (Fig. 5.7*c*). After separation, the flow turned to the right and formed the anticyclonic eddy trapped to the upstream wall. Since the current separated near the initial bend in the bathymetry, however, the flow in the eddy did not reach the downstream wall and instead continued to rotate and turn back to split on the upstream wall. Thus it fed both the cyclonic through-flow that eventually exited the canyon and the eddy that had a countercurrent flow back towards the canyon mouth. The scale of the anticyclonic eddy was found to be similar to the Rossby radius of deformation. The formation of this eddy feature can be likened to the gyre formation observed in the lee of headlands in many oceanic regions [*Bormans and Garrett*, 1989; *Cenedese and Whitehead*, 2000; *Kawasaki and Sugimoto*, 1984] but constrained by the canyon bathymetry.

5.5.1 Oceanographic relevance

This section tests the applicability of the laboratory results to further help our understanding of how buoyant currents interact with shelf bathymetry in the real ocean. In particular, we examine the hydrographic observations from the KG trough region obtained during the summer 2004 cruise aboard the *RRS James Clark Ross* discussed previously in Chapters 2 and 3. Two hydrographic and velocity sections, one upstream and one downstream of the trough (Fig. 5.1), suggested that the EGCC was the result of a splitting of the EGC at the KG. We use those data for comparison, plus additional data from upstream of the trough in the Denmark Strait region (Fig. 5.1), where many more observations are available. These additional sections are described in more detail in Chapter 4 (see Fig. 4.1 and Table 4.4), where they were used to look at interannual variability in the freshwater composition of the EGC and EGCC.

From these hydrographic data we calculated the reduced gravity and depth of the EGC upstream of the KG. To calculate g' we used the difference between the average density over the shelf (ρ_a) and the average density within the EGC core (ρ). Those values were used to find the range of Bu, W/ρ_c, and c_w / c_α listed in Table 5.2. The width of the canyon and the radius of curvature vary depending upon which isobath the current is flowing along, and hence the strength of the current since h_p is a function of Q by (5.1). For example, ρ_c varies from a minimum of ~25 km on the 350 m isobath (Fig. 5.1) to ~40 km on the 250 m isobath (and to infinity if the current is over the continental slope that continues straight down the Greenland coast). The radius ρ_c also depends on the smoothness of the bathymetry data used to estimate it, since arbitrarily small radii can be obtained if you use fine enough bathymetric data. To get the values listed above we smooth the bathymetric data with a 2-D filter that has a length scale of one Rossby radius (see Fig. 5.10), since that is the natural length scale for the flows we are considering.

Table 5.2 indicates that the value of W/ρ_c for the EGC is within (or close to) the parameter range of all three cases discussed above. This suggests that, indeed, the EGC is susceptible to both moving across the mouth of the KG, as well as flowing into the canyon. This is supportive of evidence discussed earlier in the thesis that the KG strongly influences the path of the EGC. It is instructive to ask what changes in one variable, such as g', ρ_c, or h_p, are needed to push W / ρ_c into another case (A-C), if the other variables were kept fixed. For example, observations from north of Denmark Strait showed the EGC core in 2004 to have a $g' \sim 0.024$ m s^{-2} and $h_p \sim 300$ m, so that $\rho_c \sim 22$ km. This makes $W / \rho_c = 0.9$, which is in Case B in Table 2. Keeping h_p fixed, an increase in g' to 0.049 (e.g., from a surge in ice melt or surface heating) is required to make $W / \rho_c = 1.3$ and fit into Case C, where full separation is expected. On the other hand, a decrease in h_p (and subsequent decrease in ρ_c) to 275 m, keeping g' fixed, would lower W / ρ_c to 0.63 and in Case A, with flow towards the coast along the canyon expected. This suggests a likely seasonal effect to the splitting process of the EGC, in addition to the higher frequency changes induced by the winds, and other effects, discussed below.

However, if the EGC does flow towards Greenland up the KG trough, what is the process that causes the EGCC to form as a distinct flow, instead of the EGC returning unaltered back to the shelfbreak? Two possible scenarios exist. The first is due to the effects of mixing and the second is due to the fact that the isobaths diverge on the downstream side of the KG trough near the head of the canyon (Fig. 5.1). Mixing of the buoyant polar-origin EGC water with the Atlantic-influenced water of the Irminger Sea, which is brought into the canyon as the Irminger Current turns towards Greenland, would reduce the buoyancy of the current. This decrease in g' would reduce the trapping depth of the current (h_p in Eqn. 5.1), so that it could exit the canyon on a shallower isobath, i.e. as the EGCC. For example, the 200-m isobath near the head of the KG starts out towards the shelfbreak, but turns abruptly about a quarter of the way out back towards the coast (Fig. 5.1). Observations of the EGCC farther downstream suggest that it is trapped to isobaths in the range 100-200 m [Figs. 2.4-2.6; *Wilkinson and Bacon,* 2005; *Sutherland and Pickart,* 2007].

Upstream divergence of the EGC is also a possibility but is impossible to test given the scarcity of data there. We can plot f / H contours though, Fig. 5.10, which can be used as a proxy for where flow would be constrained if it conserved its potential vorticity. This plot shows that there is a potential for part of the EGC to divert towards the inshore side of the KG before encountering the trough, thus side-stepping the issue of whether or not splitting at the canyon is important or not to EGCC formation. In all likelihood, both processes are going on, and the dominance of one over the other still depends upon the upstream strength and structure of the EGC.

However, many more processes potentially complicate the circulation over the Greenland shelf. In particular, the effect of the wind on the EGC and EGCC is strong [see Section 2.4 and Chapter 3], and for a surface-trapped flow, it could exert a dominant influence on the path of the current. In general, the winds in this area are northeasterly (downwelling favorable). These strong wind events might have a profound influence not only on the upper layer flow behavior (i.e. EGC separation or not), but also on the amount of cross-shelf exchange between the lower layer waters in the canyon and offshore water [e.g. *Castelao and Barth*, 2006; *She and Klinck*, 2000]. The impact on this effect in winter due to ice advection/formation is unclear, but probable.

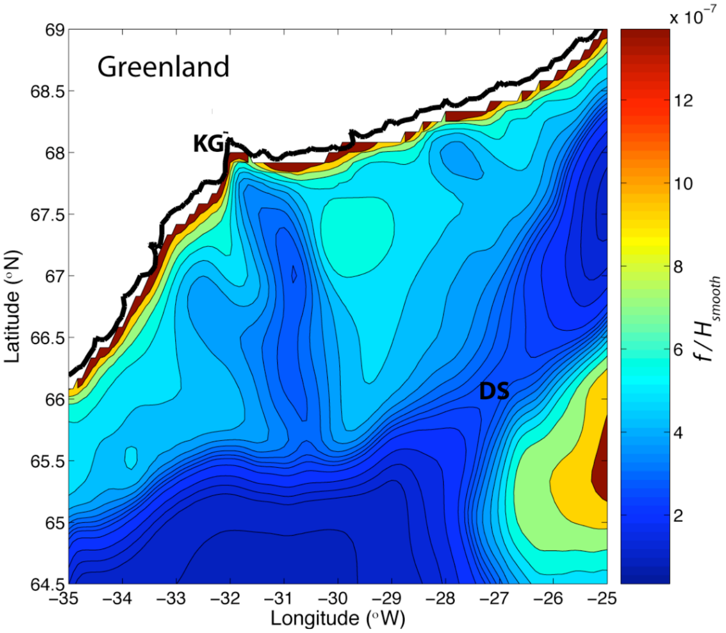

Figure 5.10. Contours of f / H, where the bathymetry, H, is smoothed using a 2-D box filter with a length scale of one Rossby radius in both directions. The smoothed bathymetry was also used to calculate the radius of curvature, ρ_c, for the KG in the text.

The area downstream of Denmark Strait, including the KG trough, is also known to be a site of high eddy kinetic energy [e.g. *Jakobsen, et al.,* 2003; *Centurioni and Gould*, 2004]. Eddies have been observed to form due to the descending of the deep overflow as it passes over the sill [e.g. *Bruce*, 1995; *Spall and Price*, 1998], and are also thought to form from the EGC itself through baroclinic instability [*R. Pickart,* pers. comm.]. What effect these eddies have on the formation of the EGCC is unknown, but the cross-shelf exchange of warm/salty water from offshore with the polar-origin EGC would certainly enhance any effects due to mixing. Tidal currents are generally small in the Nordic and Irminger Seas, but can reach up to 20 cm s^{-1} over the shelf near the KG [*Sutherland and Pickart*, 2007]. The effects of these tidal currents on the mixing between the EGC and Irminger Sea water, and the strength of the EGC and its interaction with the KG are unknown.

The results found here could also be applied to other regions of the EGC/EGCC system. One important area might be Cape Farewell, at the southern tip of Greenland, since if the EGC and EGCC were to separate there, the buoyant water might influence the stratification of the interior basin and thus the degree of convection that might occur in the Irminger Sea. However, $\rho_c \geq 90$ km for Cape Farewell, and is much greater than the local maximum Rossby radius of deformation hence, separation is not expected to occur. Wind and isobaths diverging offshore are more likely candidates for the offshore movement of the EGCC observed near Cape Farewell [*Sutherland and Pickart*, 2007]. The disappearance of the Pacific Water signal seen in Chapter 4 at Cape Farewell, and the reduction in the spatial extent of the EGCC there (Chapter 2), support the notion that the winds exert a dominant control over the current that far south.

5.6 Summary

The circulation over the southeast Greenland shelf and slope is dominated by an equatorward-flowing buoyant current system, but is complicated by the presence of irregular shelf bathymetry, strong along-shelf winds, and significant eddy activity. This chapter presented a set of laboratory experiments focused on understanding the effect of one of these processes: how a buoyant current over a sloping bottom interacts with a canyon and what controls the separation, if any, of the current from the upstream canyon bend.

We observed a range of flow behaviors that were time and scale dependent, and in agreement with previous studies. The separation of the buoyant current at the upstream edge of a canyon was found to depend upon the current width relative to the radius of curvature of the topography. The flow moved across the mouth of the canyon when the ratio W / ρ_c exceeded 1. This is in agreement with previous laboratory and analytical results, and also compares well to model results with similar configurations [*Chapman*, 2003]. Accompanying the buoyant current separation was the creation of an upper layer circulation inside the canyon; these re-circulations fit into three categories, characterized by the location of the separation point (Fig. 5.7). Case A showed no re-circulation in the head of the canyon and no flow separation. Cases B and C showed eddy features that formed in the lee of the separating current and were constrained in scale by the Rossby radius of deformation and the size of the canyon itself.

There are two important distinctions, however, between the present laboratory experiments and those examined previously. First, the laboratory flows spanned a wider range of currents with both slope-controlled and surface-trapped flows, as well as using a geometry more relevant to buoyant current-canyon interaction. In the intermediate range of c_w / c_α (close to 1), currents were observed to both separate completely and not separate at all, suggesting that, although bottom friction is important, separation driven by the inertia of the flow could overcome even the strongest bathymetric influence. A second difference is that although no background current was present separation did not always occur, in contrast to the model results of *Chapman* [2003].

These results support the hypothesis that the East Greenland Current may bifurcate at the KG trough (Fig. 5.1), as the range of oceanic values span all three laboratory regimes, which exhibit both separation and no separation. What causes the EGCC to form as a distinct jet downstream of the KG is still unclear, but is possibly due to mixing within the canyon or to bathymetric steering at the head of the canyon, where some of the isobaths diverge and follow an inner shelf route (the EGCC) or a shelfbreak route (the EGC recirculation). An unexplored possibility is the upstream splitting of the EGC suggested by Fig. 5.10. The temporal variability of this process likely occurs on timescales of days to weeks, since the strength of the EGC can vary significantly on these synoptic timescales, and is most likely influenced by the significant eddy activity observed near the canyon.

Chapter 6

Conclusions

6.1 Summary of the thesis

The main contribution of this thesis is in the first detailed description of the East Greenland Coastal Current, adding to our understanding of the subtidal circulation on the southeast Greenland shelf shown schematically in Fig. 2.14. Knowledge of the North Atlantic subpolar gyre's freshwater and volume budgets cannot be complete without inclusion of the EGCC and its interaction with the EGC, a start on which is given in the preceding chapters. The ocean is turbulent and has motion on a variety of time and space scales; this thesis has explored several forms of variability that influence the EGCC, including alongshelf wind forcing, bathymetric effects, and internal instability of the current itself, as well as describing some long-term, interannual variations. The following section summarizes the specific findings of each chapter, synthesizing the results where possible and pointing out inconsistencies or places where more work is needed, as well. A section detailing some ideas for future work is presented last.

Chapter 2 started with objectively defining the EGCC as a feature separate from the EGC, ending the historical confusion between the two currents, as well as demonstrating its presence along the entire southeastern shelf region. However, the hydrographic and velocity structure of the EGCC described also suggested that the two currents were linked, and that the EGCC might be primarily an inner branch of the shelfbreak EGC. Certainly, the θ/S properties of the two currents changed dramatically from north of Denmark Strait, where they reflected polar-origin waters, to the south near Cape Farewell. In the southern region the polar-origin core had eroded away, reflecting the intense mixing the EGC/EGCC undergoes with the warmer and saltier water of the Irminger Current, as well as through summertime solar warming. The horizontal and vertical structure of the EGCC, revealed through these hydrographic properties as well as the strong velocity signature of the jet in Figs. 2.3-2.7, were found to vary with the along-shelf wind forcing, a result in agreement with the behavior of river plumes observed in the mid-latitudes.

The influence of the along-shelf winds on the EGCC was used in Chapter 3 to improve the interpretation of the calculated volume and freshwater transports presented there. Adjusting for the strength of the wind-forcing, it was found that the EGCC and EGC could be considered as a combined system, co-varying in their transports down the shelf. Specifically, in the summer of 2004, the transport of the EGCC/EGC system was approximately constant at ~ 2 Sv, while the freshwater flux (relative to $S = 34.8$) increased from 59 mSv north of Denmark Strait to 96 mSv at Cape Farewell. This increase was explained by constructing a freshwater budget using published values for the addition of sea ice melt, meltwater runoff, and precipitation expected along the path of the currents.

Although sea ice melt was found to be the biggest contributor to the freshwater budget presented in Chapter 3, the freshwater composition results of Chapter 4 demonstrated that two other important sources of low-salinity water, Pacific Water and meteoric water, were present as well. During the sections occupied in 2004, a clear signal of Pacific Water was found below the surface layer in the vicinity of the EGCC, implying an Arctic-origin for the current, and solidifying the hypothesis that the EGCC is an inner branch of the EGC. Sea ice melt fractions increased down-shelf in the EGCC, while meteoric water fractions (including precipitation and meltwater runoff) were similar in magnitude but were larger on the shoreward side of the EGCC, reflecting their source.

The most intriguing result of Chapter 4 was the link between the Pacific Water signal seen in the EGC and EGCC near Denmark Strait to the Arctic Oscillation index. Using a set of twenty-five historical sections, a significant correlation was found between the Pacific Water content and the Arctic Oscillation index at a nine year time lag. Such a lag is in accord with residence time estimates for the Arctic Ocean, supporting previous work that hypothesized different Pacific Water pathways during different states of the Arctic Oscillation, and corroborating other work that had showed a reduction in the Pacific Water signal at Fram Strait from 1984-2005.

The final chapter dealt with the formation of the EGCC, investigating the intersection of a buoyant current with a canyon as one possible mechanism responsible for the diversion of the EGC onto the inner shelf. In a set of laboratory experiments meant to idealize the southeast Greenland shelf, as well as to be comparable to previous numerical modeling studies, we found that a buoyant current such as the EGC did indeed show a variety of behaviors, ranging from progressing straight across the canyon mouth to penetrating into the canyon with no flow across the mouth. Together with the effects of mixing and/or diverging isobaths at the head of the canyon, the EGCC could plausibly be formed from the EGC during this process. Whether or not the buoyant current separated at the initial bend in the canyon depended upon the ratio of the current width to the radius of curvature, a result in agreement with previous theoretical and laboratory results. However, our results showed that bottom friction, in terms of how slope-controlled or surface-trapped the current was, did not influence the separation process as much as previously thought.

6.2 Discussion

In synthesizing the main results of the this thesis, it is easiest to start with the final chapter, which deals with the formation of the EGCC, and work backwards towards the initial description of the current. Anywhere along the Greenland coast where a significant amount of meltwater enters the ocean, the potential exists for a cross-shelf density gradient to form and a buoyancy-driven flow to start. However, the formation process hypothesized in Chapter 5, which is essentially the diversion of a major shelfbreak flow onto the inner shelf, is the only mechanism that can explain the large transports observed at section 3 and 4 of JR105 (see Fig. 2.4-2.5 and Fig. 3.1), where the first strong realizations of the EGCC were found in 2004. The thermosalinograph data of Chapter 2 (Fig. 2.8) support this idea as well, and reveal not only the Kangerdlugssuaq Trough as an important location for the diversion of the EGC shoreward, but also the Sermilik Trough, near JR105 section 3 (see Fig. 2.14). Correspondingly, the formation of the EGCC is associated with the introduction of warmer and saltier Irminger Sea water that is brought up onto the shelf when the EGC moves shoreward. Whether this process of shelf-basin exchange is as important as the eddy-driven exchange of polar and Atlantic waters, seen commonly downstream of Denmark Strait (see Fig. 2.6), is an open question.

Another open question is whether the EGCC is confined to the southeastern Greenland shelf or if it is present along the northeastern coast as well. A hint of an EGCC-like flow was observed in 2002 during a cruise by the *IB Oden* [*Nilsson et al.*, 2006] north of JR105 section 5, but more high-resolution transects are needed. It is likely that some coastal current-like flow is present north of Denmark Strait, but may not be as strong as the southeastern EGCC, especially in the northern northeast where a northward flowing coastal current has been observed on the inshore side of Belgica Bank (Fig. 1.1; *Budeus et al.,* 1997; *Bacon et al., 2008*].

The water mass modification occurring along the southeast Greenland slope is important for setting the hydrographic properties of the quasi-continuous boundary current that circulates around Greenland and exits the Labrador Sea to flow past the Flemish Cap and the Grand Banks down to the Middle Atlantic Bight [e.g. *Fratantoni et al.,* 2007]. Along the way the current encounters numerous bathymetric irregularities similar to that modeled in Chapter 5, a fact that makes the monitoring of this current system complicated. New features of the boundary current system from east Greenland to the Middle Atlantic Bight are still being discovered. For instance, the retroflection of part of the EGC as it rounds Cape Farewell is a subject that demands more attention [*Holliday et al.,* 2007], as well as the development of the West Greenland Current and the apparent disappearance of a strong EGCC-like flow on the western side of Greenland. These results have implications for the injection of fresh water into the interior of the subpolar gyre, which might affect convective processes and the restratification of the interior after the winter months.

In terms of monitoring freshwater fluxes in the subarctic and Arctic oceans, the transports calculated for the EGCC and EGC here represent the best estimates to date. They fill a gap recognized by both recent reviews on the subject, which note that narrow (and hence hard to measure) boundary currents play a large role in carrying fresh water throughout the high-latitude oceans [*Serreze et al,* 2006; *Dickson et al.*, 2007]. It must be stressed that numbers obtained here are for summer only, and even though they were adjusted for the strong wind-forcing, they may reflect some synopticity in the system. Annual mean estimates, and any interannual variations, of the EGCC and EGC volume and freshwater transports along the southeast Greenland coast are still unknown.

The seasonality of the EGCC also remains uncertain. From this thesis it seems that it should be present during the winter, though perhaps in a modified form. Without the additional modification of the freshwater from the onset of melting, the inner branch of the EGC that becomes the summertime EGCC should more closely resemble the shelfbreak EGC. Evidence of the EGCC during the winter season comes from the one ice-based drifter of *Bacon et al.* [2008], which showed a strong inner shelf flow near JR105 section 4. Shelf moorings placed near JR105 section 2 have had mixed results, despite being designed to survive collisions with icebergs, so that no significant long-term results can be inferred from their deployments. These moorings are part of the Arctic-Subarctic Ocean Fluxes (ASOF) program, an ambitious project to monitor all the key locations of freshwater and volume transports in the high-latitude seas to detect changes and understand the implications of any climate change scenario.

In comparison to other coastal currents, the EGCC is a relatively large-scale, surface-trapped, buoyancy-driven flow, although strong wind events can alter the structure of the current significantly. Its behavior is qualitatively akin to some more well studied smaller scale coastal currents, such as the Delaware Coastal Current or the Chesapeake Coastal Current, with two main differences. First, no wind reversals are observed or seem possible for the flow scales and winds in question. Second, its freshwater source is input along a line up the coast (and along the path of melting sea ice) versus being a point source of a single river plume. The Alaska Coastal Current may be the closest analogue for the EGCC, since it is large in scale, receives freshwater over a distributed source, and is in a region of strong downwelling favorable wind stress for much of the year [*Weingartner et al.,* 2005]. During the low freshwater input conditions of winter, the Alaska Coastal Current is thinner and has a steeper front than during summer; such seasonal variability is yet to be determined for the EGCC.

6.3 Ideas for future work

More long-term measurements of the EGCC, and the entire shelf circulation, will answer many of the questions raised in this thesis on the temporal and spatial variability of the EGCC. A clearer understanding of how freshwater is distributed in the western subpolar North Atlantic is essential; not only in completing the circulation picture there, but also for a baseline of knowledge in this climate-sensitive area of the world's oceans. A recent model intercomparison by *Treguier et al.* [2005] underlines this need, since none of the models successfully reproduced the inner shelf circulation, either in the hydrographic or velocity fields, though they recognized its potential importance.

Given the difficulty of obtaining long time series records from moorings along the southeast Greenland shelf, it is desirable to come up with new observational techniques to monitor these flows. One potential idea is to utilize the large marine mammals of the region, which stay in the fish-rich waters year round, as samplers attached with mini-CTDs. *A. Rosing-Asvid* [Greenland Institute of Natural Resources, pers. comm., 2007] is doing this presently with hooded seals off the Greenland coast and plans are underway to use harbor seals in the future. Harbor seals are potentially more useful as they feed near frontal regions (such as that between the EGC and IC) and stay in one spot throughout the year while diving frequently to the bottom.

Other potential observing systems include more ice-based measurements such as those of *Bacon et al.* [2008]. Bottom-mounted acoustic Doppler current profilers (ADCP) over the inner shelf would also have greater chances of survival than standard moorings that stand tall in the water column. Clearly though, a complete mooring time series would be invaluable in clarifying the relationships between the EGCC and EGC and their respective structures and transports. The use of hardier underwater vehicles, such as the AUV's used off the Alaskan coast [*Plueddeman*, pers. comm.], might also be beneficial, while the use of gliders (e.g. like the ones being used currently to survey transects across Davis Strait [*Lee*, pers. comm.]) would be more difficult due to the strength of the current and its small spatial scales.

The complete untangling of the Pacific Water-Arctic Oscillation relationship is also left for future work, where more observations and the use of model output will aid in understanding the precise mechanisms at work. A combination of numerical model output, including biogeochemical fields (such as the Community Climate System Model, CCSM), with observations from programs such as ASOF, will allow for a more integrated understanding of these pan-Arctic changes. Certainly though, numerous large-scale changes have been observed in the Arctic, including the shifting of the Transpolar Drift Stream from the Lomonosov ridge to the Mendeleyev ridge in the 1990s [*McLaughlin et al.,* 1996; *Ekwurzel et al.,* 2001] and the spreading of a warm anomaly in the Atlantic layer of the Arctic Ocean, first observed in 1990 near the Kara Sea [e.g. *Quadfasel et al.,* 1991; *Melling,* 1998]. Many more pan-Arctic changes are predicted [see *Dickson et al.,* 2007]. These changes will have ramifications for the EGCC and EGC pathways downstream in the subpolar gyre. Also, using model fields would absolve the need to specify steady-state end-member values for the freshwater components, which introduces the biggest uncertainties in the method used in Chapter 4.

Finally, an extension of the laboratory work should be made utilizing numerical models and different laboratory geometries to fully explore the parameter space missed by the experiments of Chapter 5. This idealized modeling work could then be extended to more realistic circulation models that would help to answer a host of dynamical questions about the EGCC. The observations presented in this thesis would also help validate any model output of such an endeavor; their utilization by other global circulation models, such as the Estimating the Circulation and Climate of the Ocean (ECCO) project, was not stressed here but is extremely beneficial.

Appendix A

Error estimates for volume and freshwater transports

Quantifying the errors in absolute transport estimates, such as those made it Chapter 3 above, can be done in two ways. First, if enough realizations of a given transect exist, a standard error can be computed that indicates the range of variability in the transport value. In the absence of repeat sections, one can account for errors in calculating the transport value itself. The latter method is used here for the EGCC and EGC, as we lack enough observations to compute any significant mean values, except for the Cape Farewell sections. Standard errors calculated for that location were found to be very close to the errors calculated below and so are omitted. The method utilized is briefly discussed below and is based on work done computing absolute transport estimates of the North Atlantic Current [*Meinen*, 1998; *Meinen et al.*, 2000].

Three potential errors exist in computing the transports presented above. The first two come from station spacing and geopotential height (Φ) calculations, respectively, but are self-canceling from one CTD pair to another. The third stems from errors in calculating the reference velocity, U_{ref}. As *Meinen et al.* [2000] demonstrated, the velocity error due to station spacing by movement of the ship during a CTD occupation is $\Delta U = (\delta L/L)U_{mean}$, where L is the total distance across the section of the current, δL is the maximum ship movement during a typical station occupation, and U_{mean} is the mean velocity observed there. For the geopotential height error, inaccuracies in velocity come about through errors in determining the full water column geopotential anomaly ($\Delta\Phi$), which is about ±0.04 $m^2\ s^{-2}$ [*Meinen*, 1998]. Thus the velocity error associated with this across a section is $\Delta U = (\Delta\Phi/fL)$. Finally, the reference velocity error comes from ageostrophic effects, which include tides, Ekman flows, inertial oscillations, and internal waves, as well as from inaccuracies in the ADCP processing and calibration. Of these, the largest for the JR105 data stem from the de-tiding process, since tidal velocities on the shelf can be biased up to ±3 cm s^{-1} due to inaccuracies in the available bathymetric products [*Torres and Mauritzen*, 2002]. Also potentially important are the wind-induced ageostrophic effects such as Ekman flow and inertial oscillations, since several high wind events occurred during JR105.

We use the JR105 section 1 near Cape Farewell (Fig. 2.3) as an example to show how the error bars, listed in Table 3.1 and shown in Fig. 3.1, were computed for the EGCC transport and freshwater flux. For this section, L = 30 km and $f = 1.26 \times 10^{-4}$ s^{-1}, so that the geopotential height component of the velocity error is ±1 cm s^{-1}. If the ship moves up to $\delta L \sim 250$ m during a station, then the velocity error due to station spacing is about ±0.4 cm s^{-1}, assuming a U_{mean} of 50 cm s^{-1}. In calculating the reference velocity error, we assume that any ADCP calibration and processing inaccuracies are insignificant compared to the errors in de-tiding and other ageostrophic effects that the geostrophic velocity does not include, but that the ADCP captures. Thus, the total reference velocity error is from the ±3 cm s^{-1} de-tiding procedure and a combined ±5 cm s^{-1} error from an estimate of typical Ekman velocities, inertial oscillations, and other ageostrophic effects like cyclostrophic accelerations [*Meinen*, 1998] and equals $\sqrt{(3^2+5^2)}$ = 5.8 cm s^{-1}.

In calculating the total transport error at this section, 10 station pairs were used so that the reference velocity error is reduced by $\sqrt{N} = \sqrt{10-1} = \sqrt{9}$ where N = (# of station pairs – 1) is the effective number of degrees of freedom. The total reference velocity error is then $\sqrt{\left(1^2+0.4^2+(5.8/\sqrt{9})^2\right)}$ = 2.3 cm s^{-1}. Multiplying this by the average depth and width of the current gives an error bound on the EGCC volume transport at section 1, which is (2.3 cm s^{-1}) x (30 km) x (150 m) = ±0.1 Sv.

Error estimates were calculated this way separately for the EGC and EGCC at each section, and the results are listed in Table 3.1. To calculate the transport errors of the EGC/EGCC system (Fig. 3.1*b*), the separate error estimates are combined, e.g. for the 2004 Cape Farewell section the total error was $\sqrt{0.1^2+0.21^2}$ = ±0.23 Sv.

Errors in the freshwater flux calculation are dependent on the volume transport errors since the velocities used in computing FW_{flux} are identical. The only difference is we use the volume transport error calculated above and multiply it by the factor $(S_{mean} - S_{ref}) / S_{ref}$, where S_{mean} is the mean salinity observed and $S_{ref} = 34.8$. For example, at section 1 in 2004 the volume transport error is ±0.1 Sv, which when multiplied by (32.7 – 34.8) / 34.8 equals ±6.0 mSv. Table 3.1 lists the freshwater flux errors for each JR105 section. The largest error, ±7.7 mSv, was found at JR105 section 3 where the current is at its deepest and widest extent (see Fig. 2.5).

Bibliography

Aagaard, K. and E. C. Carmack (1989), The role of sea ice and other fresh water in the Arctic circulation. *J. Geophys. Res.*, *94***,** 14485–14498.

Anderson, L.G., G. Bjork, O. Holby, E.P. Jones, G. Kattner, K.P. Koltermann, B. Liljebad, R. Lindegren, B. Rudels, and J. Swift (1994), Water masses and circulation in the Eurasian Basin: Results from the Oden 91 expedition. *J. Geophys. Res.*, *99*, 3273–3283.

Anderson, L.G., S. Jutterstrom, S. Kaltin, E.P. Jones, and G. Bjork (2004), Variability in river runoff distribution in the Eurasian Basin of the Arctic Ocean. *J. Geophys. Res.*, *109*, C01016, doi:10.1029/2003JC001773.

Azetsu-Scott, K. and F.C. Tan (1997), Oxygen isotope studies from Iceland to an East Greenland Fjord: behavior of glacial meltwater plume. *Mar. Chem.*, *56*, 239-251.

Bacon, S., G. Reverdin, I. G. Rigor, and H. M. Smith (2002) A freshwater jet on the east Greenland shelf. *J. Geophy. Res.*, *107***,** doi:10.1029/2001JC000935.

Bacon, S., P.G. Myers, B. Rudels, and D.A. Sutherland (2008), Accessing the inaccessible: buoyancy-driven coastal currents on the shelves of Greenland and eastern Canada. *Arctic-Subarctic ocean fluxes: Defining the role of the Northern Seas in climate*. Eds. Dickson, Meincke, and Rhines.

Bauch, D., P. Schlosser, and R.G. Fairbanks (1995), Freshwater balance and the sources of deep and bottom waters in the Arctic Ocean inferred from the distribution of $H_2{}^{18}O$, *Prog. Oceanogr., 35*, 53–80.

Bigg, G.R. (1999), An estimate of the flux of iceberg calving from Greenland. *Arctic, Antarctic, Alpine Res.*, *31*, 174-178.

Bormans, M., and C. Garrett, (1989), A simple criterion for gyre formation by the surface outflow from a strait, with application to the Alboran Sea. *J. Geophy. Res.*, *94***,** 12,637-12,644.

Boyer, T.P., J.I. Antonov, H.E. Garcia, D.R. Johnson, R.A. Locarnini, A.V. Mishonov, M.T. Pitcher, O.K. Baranova, I.V. Smolyar (2006), World Ocean Database 2005. S. Levitus, Ed., *NOAA Atlas NESDIS 60*, U.S. Government Printing Office, Washington, D.C., 190 pp.

Box, J.E., D.H. Bromwich, and L.-S. Bai (2004), Greenland ice sheet surface mass balance 1991-2000: application of Polar MM5 mesoscale model and in situ data. *J. Geophys. Res.*, *109***,** doi:10.1029/2003JD004451.

Box, J.E., et al. (2006). Greenland ice sheet surface mass balance variability (1988 - 2004) from calibrated Polar MM5 output. *J. Clim.*, in press.

Bruce, J.G. (1995), Eddies southwest of Denmark Strait. *Deep-Sea Res. I, 42,* 13-29.

Budeus, G., W. Schneider, and G. Kattner (1997), Distribution and exchange of water masses in the Northeast Water Polynya, *J. Mar. Sys., 10*, 123–138.

Bryan, F. (1986), High-latitude salinity effects and interhemispheric thermohaline circulations. *Nature*, *323***,** 301-304.

Castelao, R.M., and J.A. Barth, (2006), The relative importance of wind strength and along-shelf bathymetric variations on the separation of a coastal upwelling jet. *J.*

Phys. Oceanogr., *36*, 412-425.

Cavalieri, D., C. Parkinson, P. Gloerson, and H.J. Zwally (2005) Sea ice concentrations from Nimbus-7 SMMR and DMSP SSM/I passive microwave data, 2001-2004. Boulder, CO, USA: National Snow and Ice Data Center.

Cenedese, A., Vigarie, C., and E.V. di Modrone, (2005), Effects of a topographic gradient on coastal current dynamics. *J. Geophy. Res.*, *110*, doi:10.1029/2004JC002632.

Cenedese, C., and J.A. Whitehead, (2000), Eddy shedding from a boundary current around a cape over a sloping bottom. *J. Phys. Oceanogr., 30*, 1514-1531.

Cenedese, C. and P.F. Linden, (2002), Stability of a buoyancy-driven coastal current at the shelf break. *J. Fluid Mech.*, *452*, 97-121.

Centurioni, L.R., and W.J. Gould (2004), Winter conditions in the Irminger Sea observed with profiling floats. *J. Mar. Res., 62*, 313–336.

Chapman, D.C., and S.J. Lentz, (1994), Trapping of a coastal density front by the bottom boundary layer. *J. Phys. Oceanogr., 24*, 1464-1479.

Chapman, D.C., (2003), Separation of an advectively trapped buoyancy current at a bathymetric bend. *J. Phys. Oceanogr., 33*, 1108-1121.

Cho, Y.-K., R.C. Beardsley, and V.A. Sheremet, (2002), On the cause of Scotian Shelf crossovers. *Geophys. Res. Lett., 29*, doi:10.1029/2002GL014968.

Clarke, R.A. (1984), Transport through the Cape Farewell-Flemish Cap section. *Rapp. P.-v.Reunn. cons. int. Explor. Mer.*, *185*, 120-130.

Coachman, L.K., K. Aagaard, and R.B. Tripp (1975), *Bering Strait: the regional physical oceanography.* 172 pp., Univ. Wash. Press, Seattle.

Codispoti, L.A. and D. Lowman (1973) A reactive silicate budget for the Arctic Ocean. *Limnol. Oceanogr., 18,* 448-456.

Cooper, L.W., T.E., Whitledge, J.M. Grebmeier, and T. Weingartner (1997), The nutrient, salinity, and stable oxygen isotope composition of Bering and Chukchi Seas waters in and near Bering Strait. *J. Geophys. Res.*, *102*, 12563-12574.

Curry, R., R. R. Dickson, and I. Yashayaev (2003), A change in the freshwater balance of the Atlantic Ocean over the past four decades. *Nature*, *426*, 826-829.

Curry, R., and C. Mauritzen (2005), Dilution of the northern North Atlantic Ocean in recent decades. *Science, 308,* 1772-1774.

Dickson, R. R., and J. Brown (1994), The production of North Atlantic Deep Water: sources, rates, and pathways. *J. Geophys. Res.*, *99*, 12319-12341.

Dickson, R., B. Rudels, S. Dye, M. Karcher, J. Meincke, and I. Yashayaev (2007), Current estimates of freshwater flux through Arctic and subarctic seas. *Prog. Oceanogr., 73,* 210 - 230.

Dodd, P. (2007), The freshwater transport of the East Greenland Current. M.S. thesis. Univ. East Anglia, Norwich, UK.

Egbert, G.D., A.F. Bennett, and M.G.G. Foreman (1994), TOPEX/POSEIDON tides estimated using a global inverse model. *J. Geophys. Res.*, *99*, 24821-24852.

Ekwurzel, B., P. Schlosser, R.A. Mortlock, and R.G. Fairbanks (2001), River runoff, sea ice meltwater, and Pacific water distribution and mean residence times in the Arctic Ocean. *J. Geophys. Res.*, *106*, 9075–9092.

Falck, E. (2001), Contribution of waters of Atlantic and Pacific origin in the Northeast Water Polynya. *Polar Res.*, *20*, 193-200.

Falck, E., G. Kattner, and G. Budeus (2005) Disappearance of Pacific Water in the northwestern Fram Strait. *Geophys. Res. Lett.*, *32*, L14619 doi:10.1029/2005GL023400.

Fahrbach, E., J. Meincke, S. Osterhus, G. Rohardt, U. Schauer, V. Tverberg, and J. Verduin (2001), Direct measurements of volume transports through Fram Strait. *Polar Res., 20*, 217-224.

Fong, D.A., W.R. Geyer, and R.P. Signell (1997), The wind-forced response of a buoyant coastal current: observations of the western Gulf of Maine plume. *J. Mar. Sys.*, *12***,** 69-81.

Fong, D.A., and W.R. Geyer (2001), Response of a river plume during an upwelling favorable wind event. *J. Geophys. Res.*, *106***,** 1067-1084.

Fratantoni, P.S., R.S. Pickart, D.J. Torres, and A. Scotti (2001), Mean structure and dynamics of the shelfbreak jet in the Middle Atlantic Bight during fall and winter. *J. Phys. Oceanogr.*, *31*, 2135-2156.

Fratantoni, P.S., and R.S. Pickart (2007), The Western North Atlantic shelfbreak current system in summer. *J. Phys. Oceanogr., 37,* 2509-2533.

Gordon, L.I., J.C. Jennings, A.A. Ross, and J.M. Krest (1993), A suggested protocol for continuous flow automated analysis of seawater nutrients (phosphate, nitrate, nitrite, and silicic acid) in the WOCE Hydrographic Program and the Joint Global Ocean Fluxes Study, *WOCE Hydrographic Program Office, Methods Manual WHPO 91-1.*

Griffiths, R.W., and P.F. Linden (1981), The stability of buoyancy driven coastal currents. *Dyn. Atmos. Oceans, 5*, 281-306.

Hakkinen, S. and P. Rhines (2004), Decline of subpolar North Atlantic circulation during the 1990s. *Science*, *304*, 555-559.

Halkin, D., and T. Rossby (1985), The structure and transport of the Gulf Stream at 73W. *J. Phys. Oceanogr.*, *15*, 1439-1452.

Hansen, B. and S. Osterhus (2000), North Atlantic-Nordic Sea exchanges. *Prog. Oceanogr.*, *45*, 109-208.

Hatun, H., A.B. Sando, H. Drange, B. Hansen, and H. Valdimarsson (2005), Influence of the Atlantic subpolar gyre on the thermohaline circulation. *Science*, *309*, 1841-1844.

Holliday, N.P., A. Meyer, S. Bacon, S.G. Alderson, and B. de Cuevas (2007) Retroflection of part of the east Greenland current at Cape Farewell. *Geophys. Res. Lett., 34,* doi:10.1029/2006GL029085.

IOC, IHO and BODC, 2003: Centenary Edition of the GEBCO Digital Atlas, published CD-ROM on behalf of the Intergovernmental Oceanographic Commission and the International Hydrographic Organization as part of the General Bathymetric Chart of the Oceans, British Oceanographic Data Centre, Liverpool, U.K.

Jakobsen, P.K., M.H. Ribergaard, D. Quadfasel, T. Schmith, and C.W. Hughes (2003), Near-surface circulation in the northern North Atlantic as inferred from Lagrangian drifters: variability from the mesoscale to the interannual. *J. Geophys.*

Res., 108, doi:10.1029/2002JC001554.

Jones, E.P., and L.G. Anderson (2008) Is the global conveyor belt threatened by Arctic Ocean freshwater outflow? *Arctic-Subarctic ocean fluxes: Defining the role of the Northern Seas in climate*. Eds. Dickson, Meincke, and Rhines.

Jones, E.P., L.G. Anderson, S. Jutterstrom, and J.H. Swift (2007), Sources and distribution of fresh water in the East Greenland Current. *J. Geophys. Res.,* in press.

Jones, E.P., L.G. Anderson, and J.H. Swift (1998), Distribution of Atlantic and Pacific waters in the upper Arctic Ocean: implications for circulation. *Geophys. Res. Lett.*, *25*, 765–768.

Jones, E.P., J.H. Swift, L.G. Anderson, M. Lipizer, G. Civitarese, K.K. Falkner, G. Kattner, and F. McLaughlin (2003), Tracing Pacific water in the North Atlantic Ocean. *J. Geophys. Res.*, *108*, doi:10.1029/2001JC001141.

Jonsson, S., and H. Valdimarsson (2004), A new path for the Denmark Strait overflow water from the Iceland Sea to Denmark Strait, *Geophys. Res. Lett.*, *31*, doi:10.1029/2003GL019214.

Kawasaki,, V., and T. Sugimoto, (1984), Experimental studies on the formation and degeneration processes of the Tsugaru Warm Gyre. *Ocean Hydrodynamics of the Japan and East China Seas, Oceanogr. Ser.*, *39*, ed. T. Ichiye, 225-238.

Klinck, J.M., (1996), Circulation near submarine canyons: a modeling study. *J. Geophys. Res.*, *101*, 1211-1223.

Klinger, B.A., (1994), Inviscid current separation from rounded capes. *J. Phys. Oceanogr., 24*, 1805-1811.

Krabill, W., et al. (1999), Rapid thinning of parts of the southern Greenland ice sheet. *Science*, *283*, 1522-1524.

Krabill, W., et al. (2004), Greenland Ice Sheet: increased coastal thinning. *Geophys. Res. Lett.*, *31*, doi:10.1029/2005GL021533.

Krauss, W. (1995), Currents and mixing in the Irminger Sea and in the Iceland Basin. *J. Geophys. Res.*, *100*, 10851-10871.

Kwok, R., and D. A. Rothrock (1999), Variability of Fram Strait ice flux and the North Atlantic Oscillation. *J. Geophys. Res.*, *104*, 5177-5189.

Large, W.G., and S. Pond (1981), Open ocean momentum flux measurements in moderate to strong winds. *J. Phys. Oceanogr.*, *11*, 324-336.

Lentz, S.J. and K.R. Helfrich, (2002), Buoyant gravity currents along a sloping bottom in a rotating fluid. *J. Fluid Mech.*, *464*, 251 – 278.

Lentz, S.J. and J. Largier (2006), The influence of wind forcing on the Chesapeake Bay buoyant coastal current. *J. Phys. Oceanogr.*, *36*, 1305–1316.

Loder, J.W., B. Petrie, and G. Gawarkiewicz (1998), The coastal ocean off northeastern North America. A large scale view. in *The Sea*, A.R. Robinson and K.H. Brink, Eds., 105-153.

Lozier, M.S., M.S.C. Reed, and G.G. Gawarkiewicz (2002), Instability of a shelfbreak front. *J. Phys. Oceanogr.*, *32*, 924–944.

McLaughlin, F.A., E.C. Carmack,, R.W. MacDonald, and J.K. Bishop (1996), Physical and geochemical properties across the Atlantic/Pacific water mass front in the southern Canadian Basin. *J. Geophys. Res., 101,* 1183-1197.

Malmberg, S.-A., H.G. Gade, and H.E. Sweers (1967), Report on the second joint Icelandic-Norwegian expedition to the area between Iceland and Greenland in August-September 1965. *NATO Subcommittee on Oceanographic Research*, Technical Report No. 41, Irminger Sea Project, 44 pp.

Malmberg, S.-A. (1985), The water masses between Iceland and Greenland. *Rit. Fishideildar*, *9*, 127-140.

Martin, T., and P. Wadhams (1999), Sea-ice flux in the East Greenland Current. *Deep-Sea Res. II*, *46*, 1063-1082.

Meinen, C.S. (1998), Transport of the North Atlantic Current. Ph.D. thesis, Univ. of Rhode Island, unpublished.

Meinen, C.S., D.R. Watts, and R.A. Clarke (2000), Absolutely referenced geostrophic velocity and transport on a section across the North Atlantic Current. *Deep-sea Research I*, *47*, 309-322.

Melling, H. (1998) Hydrographic changes in the Canada basin of the Arctic Ocean, 1979-1996. *J. Geophys. Res., 103,* 7637-7645.

Melling, H. (2000), Exchanges of freshwater through the shallow straits of the North American Arctic. *The freshwater budget of the Arctic Ocean*, E. E. Lewis, Ed., Kluwer, 479-502.

Meredith, M., K. Heywood, P. Dennis, L. Goldson, R. White, E. Farbach, U. Schauer, and S. Osterhus (2001), Freshwater fluxes through the western Fram Strait. *Geophys. Res. Lett., 28,* 1615–1618.

Moore, G.W.K., and I.A. Renfrew (2005), Tip jets and barrier winds: a QuikSCAT climatology of high wind events around Greenland. *J. Clim.*, *18*, 3713-3725.

Mork, M. (1981), Circulation phenomena and frontal dynamics of the Norwegian Coastal Current. *Phil. Trans. Roy. Soc. London*, *Series A*, *302*, 635-647.

Mosby, H. (1962), Water, salt, and heat balance of the North Polar Sea and of the Norwegian Sea. *Geophys. Pubs.*, *24*, 289-313.

Nilsson, J., G. Bjork, B. Rudels, P. Winsor, and D. Torres (2006), Late-winter conditions and freshwater transport in the East Greenland Current: results from an icebreaker-based survey. *J. Geophys. Res.,* submitted.

Ostlund, H.G. and G. Hut (1984), Arctic Ocean water mass balance from isotope data. *J. Geophys. Res.*, *89*, 6373–6381.

Pedlosky, J. (1987), *Geophysical Fluid Dynamics*, 2nd edition. Springer. 710 pp.

Pickart, R.S., M.A. Spall, M.H. Ribergaard, G.W.K. Moore, and R.F. Milliff (2003), Deep convection in the Irminger Sea forced by the Greenland tip jet. *Nature, 424,* 152-156.

Pickart, R.S., D.J. Torres, and P.S. Fratantoni (2005), The East Greenland spill jet. *J. Phys. Oceanogr.*, *35*, 1037–1053.

Proshutinsky, A.Y. and M.A. Johnson (1997), Two circulation regimes of the wind-driven Arctic Ocean. *J. Geophys. Res., 102,* 12,493-12,514.

Quadfasel, D., A. Sy, D. Wells, and A. Tunik (1991), Warming in the Arctic. *Nature*, 350, 385, doi:10.1038/350385a0.

Reeh, N. (1985), Greenland ice-sheet mass balance and sea-level change. *Glaciers, ice* *sheets, and sea level: effect of a CO2-induced climatic change*, Department of Energy, 155-171.

Reverdin, G., P.P. Niiler, and H. Valdimarsson (2003), North Atlantic Ocean surface currents. *J. Geophys. Res.*, *108*, doi:10.1029/2001JC001020.

Risien, C.M., and D.B. Chelton (2007), A global climatology of surface wind and wind stress fields from 7 years of QuikSCAT scatterometer data. *J. Phys. Oceanogr.*, Submitted.

Rignot, E., D. Braaten, S.P. Gogineni, W.B. Krabill, and J.R. McConnell (2004), Rapid ice discharge from southeast Greenland glaciers. *Geophys. Res. Lett.*, *31*, doi:10.1029/2004GL019464.

Rudels, B., Fahrbach, E., Meincke, J., Budeus, G., and P. Erikson (2002), The East Greenland Current and its contribution to the Denmark Strait Overflow. *ICES J. Mar. Sci., 59,* 1133-1154.

Rudels, B., E.P. Jones, U. Schauer, and P. Eriksson (2004), Atlantic sources of the Arctic Ocean surface and halocline waters. *Polar Res., 23,* 181-208.

Schlosser, P., D. Bauch, R. Fairbanks, and G. Bonisch (1994), Arctic river-runoff: Mean residence time on the shelves and in the halocline. *Deep Sea Res. Part A*, *41*, 1053–1068.

Serreze, M.C., A.P. Barrett, A.G. Slater, R.A. Woodgate, K. Aagaard, R.B. Lammers, M. Steele, R. Moritz, M. Meredith, and C.M. Lee (2006), The large-scale freshwater cycle of the Arctic. *J. Geophys. Res.*, *111*, doi:10.1029/2005JC003424.

She, J. and J.M. Klinck, (2000), Flow near submarine canyons driven by constant winds. *J. Geophys. Res.*, *105*, 28,671-28,694.

Sheremet, V.A., and J. Kuehl, (2007), Gap-leaping western boundary currents in a circular tank model. *J. Phys. Oceanogr.*, *37*, 1488 – 1495.

Shimada, K., E.C. Carmack, K. Hatakeyama,, and T. Takizawa (2001), Varieties of shallow temperature maximum waters in the western Canadian Basin of the Arctic Ocean. *Geophys. Res. Lett., 28*, 3441-3444.

Spall, M.A., and J.F. Price (1998), Mesoscale variability in Denmark Strait: the PV outflow hypothesis. *J. Phys. Oceanogr.*, *28*, 1598-1623.

Steele, M., J. Morison, W. Ermold, I. Rigor, M. Ortmeyer, and K. Shimada (2004), Circulation of summer Pacific halocline water in the Arctic Ocean. *J. Geophys. Res.*, *109*, C02027, doi:10.1029/2003JC002009.

Stefansson, U. (1968) Dissolved nutrients, oxygen, and water masses in the Northern Irminger Sea, *Deep Sea Res.*, *15*, 541-575.

Sutherland, D.A., and R.S. Pickart (2007), The East Greenland Coastal Current: structure, variability, and forcing. Accepted to *Prog. Oceanogr.*

Taylor, J.R., K.K. Falkner, U. Schauer, and M. Meredith (2003), Quantitative considerations of dissolved barium as a tracer in the Arctic Ocean. *J. Geophys. Res.*, *108*, doi:10.1029/2002JC001635.

Torres, D.J. and C. Mauritzen (2002), Using a global tidal model for removing the tides from direct velocity measurements in the Faroe Bank Channel. *Amer. Geophys. Union*, *82*, OS32F-197.

Treguier, A.M., S. Theetten, E.P. Chassignet, T. Penduff, R. Smith, L. Talley, J.O. Beismann, and C. Boning (2005), The North Atlantic Subpolar Gyre in four high-resolution models. *J. Phys. Oceanogr.*, *35*, 757-772.

Vinje, T., N. Nordlund, and A. Kvambekk (1998), Monitoring ice thickness in Fram Strait. *J. Geophys. Res.*, *103***,** 10437-10449.

Weingartner, T.J., S. Danielson, Y. Sasaki, V. Pavlov, and M. Kulakov (1999), The Siberian Coastal Current: A wind- and buoyancy forced Arctic coastal current. *J. Geophys. Res.*, *104*, 29697-29713.

Weingartner, T.J., Danielson S.L. and T.C. Royer (2005), Freshwater variability and predictability in the Alaska Coastal Current. *Deep-Sea Res. II*, *52*, 169-191.

Whitehead, J.A., and A.K. Miller, (1979), Laboratory simulation of the gyre in the Alboran Sea. *J. Geophys. Res.*, *84*, 3733-3742.

Whitehead, J.A., (1985), The deflection of a baroclinic jet by a wall in a rotating fluid. *J. Fluid Mech.*, *157*, 79-93.

Wilkinson, D. and S. Bacon (2005), The spatial and temporal variability of the East Greenland Coastal Current from historic data. *Geophys. Res. Lett.*, *32*, doi:10.1029/2005GL024232.

Williams, W.J., G. Gawarkiewicz, and R.C. Beardsley (2001), The adjustment of a shelfbreak jet to cross-shelf topography. *Deep-Sea Res. II*, *48*, 373-393.

Wilson, C., and D.W.R. Wallace (1990), Using the nutrient ratio NO/PO as a tracer of continental shelf waters in the Central Arctic Ocean. *J. Geophys. Res.*, *95*, 22,193–22,208.

Wolfe, C.L., and C. Cenedese (2006), Laboratory experiments on eddy generation by a buoyant coastal current flowing over variable bathymetry. *J. Phys. Oceanogr.*, *36*, 395-411.

Woodgate, R.A., and K. Aagaard (2005), Revising the Bering Strait freshwater flux into the Arctic Ocean. *Geophys. Res. Lett.*, *32*, L02602, doi:10.1029/2004GL021747.

Yamamoto-Kawai, M., F.A. McLaughlin, E.C. Carmack, S. Nishino, and K. Shimada (2007), Freshwater budget of the Canada Basin, Arctic Ocean from geochemical tracer data. Submitted to *J. Geophys. Res.*

Yankovsky, A.E., and D.C. Chapman (1997), A simple theory for the fate of buoyant coastal discharges. *J. Phys. Oceanogr. 27*, 1386-1401.